

**COARSENING, STEADY-STATE AND PHASE TRANSITION IN
SELF-PROPELLED PARTICLES**

A THESIS SUBMITTED FOR THE DEGREE OF
DOCTOR OF PHILOSOPHY (SCIENCE)
IN PHYSICS (THEORETICAL)

by
RAKESH DAS

Department of Physics
University of Calcutta

2018

Dedicated to

My Parents

&

My Teacher Sri Phani Bhushan Mondal

ACKNOWLEDGEMENTS

I would like to thank my research supervisors Dr. Manoranjan Kumar and Dr. Shradha Mishra for their constant support, guidance and encouragement. I especially thank them for letting me do mistakes and realise these errors later by myself which made me understand the associated concepts clearly. I would also like to thank our collaborator Prof. Sanjay Puri from Jawaharlal Nehru University, New Delhi for suggestions and advises. Personal interactions with Dr. Sakuntala Chatterjee, Prof. Subhrangshu Sekhar Manna, Prof. Manu Mathur, Prof. Samir Kumar Pal and Prof. Indrani Bose enriched my understanding of the science. I acknowledge S. N. Bose National Centre for Basic Sciences for financial support and moreover for providing research facilities. I also acknowledge kind hospitality of IIT(BHU), Varanasi during my visits there.

I would like to thank my group-mates Aslam da, Daya da, Sudipta, Debasmita, Monalisa, Sudip, Koushik, Saniur for academic and non-academic discussions. I also thank Subhajit da and Raj Kumar Sadhu for their companionship. I respect their depth in thought, calmness in handling issues and helpful character. I am also delighted to have friends like Shinde da, Kartik da, Somnath da, Subrata da, Subhasish da, Sayani di, Pandey ji, Krishnendu da, Anita, Keshab, Ananda, Jayita and many others. I especially acknowledge the 'breakfast table' in our Students' mess where me and some of the regular faces mentioned above exchange our views on innumerable issues. I also thank Sarowar da, the founder of 'Khaja Band', who made our Centre an enjoyable place to live.

My stay in the S. N. Bose Centre is full with various kinds of constructive activities, thank to Arghya da, Biplab da, Sumanta, Subhadip, Debasish, Poulami, Anulekha, Rahul, Anupam, Swarnali and many others. The only motivation for me to be in the campus on the weekends is our Cricket ground, where I have shared joyful moments with Supriyo da, Abhishek da, Souvanik, Maheub, panda and many others.

I must acknowledge friends from my old days who have deep effect on my academic life and also in my personal being. I thank Subhrajyoti for motivating me towards scientific research. The moments we share on the banks of Damodar discussing about anything related to society are precious to me. I thank Bhaskar who used to be my roommate in the University days with whom I have many cherishable memories. I also thank Shramana for the moments we spend together. I really enjoyed explaining vectors and matrix algebra to you, and telling you my own fictitious stories that I never had the patience to keep written. It is the innocence of my little niece Madhushree that make me relaxed whenever I get frustrated about anything.

Finally, I express my deepest gratitude, respect and love for my parents Smt. Santwana Das and Sri Jahar Das, and my teacher Sri Phani Bhushan Mondal. I doubt whether I am capable of writing what they are to me! Probably the most difficult thing to do is to explain the meaning of life. It is their lesson that drives me incessantly to find a justifiable explanation for that perpetual question.

PUBLICATIONS

PAPERS TO BE INCLUDED IN THE PH.D. THESIS

- **Order-disorder transition in active nematic: A lattice model study**, Rakesh Das, Manoranjan Kumar and Shradha Mishra, *Sci. Rep.* **7**, 7080 (2017).
- **Ordering dynamics of self-propelled particles in an inhomogeneous medium**, Rakesh Das, Shradha Mishra and Sanjay Puri, *Europhys. Lett.* **121**, 37002 (2018).
- **Polar flock in the presence of random quenched rotators**, Rakesh Das, Manoranjan Kumar and Shradha Mishra, arXiv:1802.08861v2 [cond-mat.stat-mech].
- **Polar flock in the presence of non-quenched inhomogeneity**, Rakesh Das *et al.* (*in preparation*).

OTHER PUBLICATIONS

- **Enhanced dynamics of active Brownian particle in a periodic and confined channel**, Sudipta Pattanayak, Rakesh Das, Manoranjan Kumar and Shradha Mishra, arXiv:1807.07766v1 [cond-mat.soft].

CONTENTS

1	INTRODUCTION	1
1.1	Active systems are out-of-equilibrium	1
1.2	Categories of active matter	4
1.2.1	Polar and apolar	4
1.2.2	Dry and wet	5
1.3	Methodology	6
1.3.1	Agent-based simulation	6
1.3.2	Hydrodynamics	7
1.3.3	Experiments	8
1.4	Polar system	8
1.4.1	Vicsek Model	8
1.4.2	Noise: angular and vectorial	9
1.4.3	Hydrodynamics	10
1.4.4	Active Ising model	14
1.4.5	Experiments	15
1.5	Apolar system	17
1.5.1	Microscopic model	17
1.5.2	Hydrodynamics	18
1.5.3	Experiments	21
1.6	Coarsening	22
1.6.1	Coarsening towards an equilibrium state	22
1.6.2	Coarsening in active systems	25
1.7	Effect of inhomogeneity	25
1.7.1	Non-active systems with inhomogeneity	26
1.7.2	Active systems with inhomogeneity	27

1.8	Objective and organisation of this thesis	28
2	A LATTICE MODEL STUDY OF ACTIVE NEMATIC	29
2.1	Introduction	29
2.2	Model	30
2.3	Numerical study	32
2.3.1	Phase diagram – equilibrium and active model	33
2.3.2	Two-point orientation correlation	38
2.3.3	Orientation distribution and autocorrelation of the mean orientation	40
2.4	Hydrodynamics of the active model at low density	42
2.5	Discussion	45
	Appendices	48
2.A	Order-disorder transition in the equilibrium model	48
2.B	Renormalised mean field (RMF) study of active nematic for small scalar order parameter	48
3	ORDERING DYNAMICS OF SELF-PROPELLED PARTICLES IN AN INHOMOGENEOUS MEDIUM	52
3.1	Introduction	52
3.2	Model	53
3.3	Numerical study	56
3.3.1	Coarsening in clean system	58
3.3.2	Coarsening in inhomogeneous system	60
3.4	Discussion	67
4	POLAR FLOCK IN THE PRESENCE OF RANDOM QUENCHED ROTATORS	69
4.1	Introduction	69
4.2	Model	70
4.3	Numerical study	71
4.3.1	Quasi-long range order	72

4.3.2	Scaling	75
4.3.3	Transition from quasi-long range order to disorder state	77
4.4	Linearised hydrodynamics	79
4.5	Discussion	81
Appendices		
4.A	Voigt profile	83
4.B	Linearised theory of the broken symmetry state in the presence of quenched inhomogeneities	83
5	POLAR FLOCK IN THE PRESENCE OF NON-QUENCHED INHOMOGENEITY	88
5.1	Introduction	88
5.2	Model	89
5.3	Numerical study	90
5.3.1	Clean system	91
5.3.2	SPPs with quenched inhomogeneity	91
5.3.3	SPPs with non-quenched inhomogeneity	92
5.4	Discussion	98
6	CONCLUSION	99

LIST OF FIGURES

- Figure 1.1 A polar (blue arrow) SPP moves forward only, whereas apolar particle (blue ellipse) moves towards its head or tail with equal probability. If a collection of polar particles align parallel to each other, they altogether move towards a director as indicated by the green arrow for the polar arrangement. On the contrary, if the polar particles construct a mutual anti-parallel arrangement, the flock does not have a macroscopic velocity. Similarly a collection of apolar particles aligned parallel to each other does not go anywhere macroscopically. For these apolar arrangements its director (head-tail symmetric green arrow) represents the direction of broken rotational symmetry. For both the polar and the apolar arrangements, the translational symmetry is not broken. 5
- Figure 1.2 Though active nematic does not have any macroscopic velocity, splay or bend arrangement of the apolar particles introduces local polarity as indicated by the arrows. This local polarity induces local particle current proportional to the local curvature of the configuration. 19
- Figure 2.1 (a) Two dimensional square lattice with occupied ($n = 1$) or unoccupied ($n = 0$) sites. Filled circles indicate the occupied sites. Inclinations of the rods towards the horizontal direction show respective particle orientations $\theta \in [0, \pi]$. (b) Equilibrium move: particle can move to any of the four neighbouring sites with equal probability $1/4$. (c, d) Active move: particle can move to either of its two neighbouring sites with probability $1/2$, if unoccupied, in the direction it is more inclined to, *i. e.*, along BD in (c), and AC in (d). 31

Figure 2.2 Phase diagram for both the equilibrium and the active nematic in the density versus inverse temperature plane. The equilibrium system remains in the isotropic (EI) state in the low density regime (on the left of the solid line) and in the nematic (EN) state in the high density regime (on the right of the solid line). The active nematic goes from the disordered isotropic (I) state to the locally ordered inhomogeneous mixed (IM) state with increasing density or decreasing temperature. The I - IM transition occurs with the appearance of clear bands (BS) in the low temperature regime. In the high density regime the active nematic shows bistability between the IM and the homogeneous globally ordered (HO) state. 34

Figure 2.3 Scalar order parameter versus packing density plot for 400×400 system size at $\beta\epsilon = 2.0$. The equilibrium system (E, solid line) shows continuous isotropic to nematic state transition with increasing density. The active system goes from the isotropic (I) state to the locally ordered inhomogeneous mixed (IM, \times) state. In the high density regime the system shows bistability between the IM state and the homogeneous globally ordered (HO, \bullet) state. 34

Figure 2.4 Left panel shows snapshot of the particle inclination towards the horizontal direction. Colour bar ranging from zero to one indicates vertical to horizontal orientation, respectively. BS is the banded state configuration shown for $(\beta\epsilon, C) = (2.0, 0.38)$. IM, HO and EN state configurations are shown for $(\beta\epsilon, C) = (2.0, 0.78)$. Right panel shows the coarse-grained density in the respective states. 35

Figure 2.5 Density fluctuation $\Delta N = \sqrt{\langle N^2 \rangle - \langle N \rangle^2}$. All the active ordered states show large density fluctuation obeying the relation $\Delta N \sim \langle N \rangle^\zeta$ with $\zeta > 1/2$. The active disordered isotropic state shows normal density fluctuation with $\zeta = 1/2$. 37

- Figure 2.6 The I to IM transition at low temperature occurs with a jump in S where the particles form bands (BS). Distribution of the scalar order parameter near the I - BS transition at $(\beta\epsilon, C) = (2.0, 0.37)$ shows two peaks. 37
- Figure 2.7 (a) Finite size scaling of S for both the HO and the IM state at $(\beta\epsilon, C) = (2.0, 0.76)$. (b) Order parameter time series show that the active system flips between the HO and the IM state in the bistable regime. Two time series are shown for two different parameter values in the high density regime. 39
- Figure 2.8 Two-point orientation correlation shown for $\beta\epsilon = 2.0$ on log-log scale. (a) Active model: $g_2(r)$ decays exponentially at low density (\circ, \square) and algebraically at high density (\diamond, \triangle). In the bistable regime at high density (\triangle), $g_2(r)$ decays algebraically in the HO state and abruptly in the IM state. (b) Equilibrium model: $g_2(r)$ decays exponentially at low density (\circ, \square) and algebraically at high density ($\diamond, +, \triangle$). Continuous lines are the respective fits, fitted for more than one decade. 40
- Figure 2.9 Steady-state characteristics of high density states. (a) Orientation distribution $P(\theta)$ of particles calculated from one snapshot in the steady-state. $P(\theta)$ fits with Gaussian distribution (continuous lines) for both the HO and the EN states. The IM state shows broad distribution of θ . (b) Distribution of the mean orientation $P(\bar{\theta})$ calculated from $\bar{\theta}$ of each snapshot in the steady-state. $P(\bar{\theta})$ is broad for the EN state in comparison to the HO state. 41
- Figure 2.10 Steady-state characteristics of high density states. Steady-state auto-correlation $C_{\bar{\theta}}(t)$ of the mean orientation of the system. All plots are shown for $(\beta\epsilon, C) = (2.0, 0.80)$. 42

Figure 2.A.1 Order-disorder transition in the equilibrium model. Main – scalar order parameter S versus inverse temperature $\beta\epsilon$ plot for different density C . With increasing $\beta\epsilon$ the system goes from the isotropic (small S) to the nematic (large S) state. The critical temperature for $C = 1$ matches with the corresponding value for the equilibrium XY model [108]. Inset – the critical inverse temperature decreases with increasing density. Similar phenomenon was earlier observed for diluted XY model [108]. 48

Figure 3.1 Heat map of (left panel) the orientation $\theta(\mathbf{r}, t) = \tan^{-1} \left(\frac{p_y(\mathbf{r}, t)}{p_x(\mathbf{r}, t)} \right)$, and (right panel) the density, shown for the clean system ($\Delta = 0$). Starting with random orientation and uniform density at $t = 0$, the system coarsens with time. Respective times are indicated on the left margin. 57

Figure 3.2 (a) Two-point correlation function versus distance plot for the polarisation field in the clean system ($\Delta = 0$) at different times. (b) Two-point correlation function versus scaled distance plot. C_p shows good collapse. 59

Figure 3.3 (a) Two-point correlation function versus distance plot for the density field in the clean system ($\Delta = 0$) at different times. (b) Two-point correlation function versus scaled distance plot. C_ρ does not show good scaling; therefore, dynamic scaling is absent for the density field. 60

Figure 3.4 (a) Growth law of the hydrodynamic variables in the clean ($\Delta = 0$) system. The self-propelled speed $v_s = 0.5$ for the random field active model (RFAM), whereas $v_s = 0$ for the zero-SPP model (zero-SPPM). The straight lines are drawn for the respectively indicated power-laws. (b) Plot of effective growth exponent of the hydrodynamic fields versus time in the clean system for the RFAM. 61

- Figure 3.5 Heat map of (left panel) the orientation $\theta(\mathbf{r}, t) = \tan^{-1} \left(\frac{P_y(\mathbf{r}, t)}{P_x(\mathbf{r}, t)} \right)$, and (right panel) the density, shown for fixed time $t = 1000$ and different disorder strengths Δ indicated on the left margin. Size of the ordered domains reduces with increasing strength of disorder. 62
- Figure 3.6 (a) Two-point correlation function for the polarisation, drawn for different disorder strengths at $t = 1000$. (b) shows scaling collapse of C_p as a function of r/L_p . Morphology of the polarisation field is approximately independent of disorder. 63
- Figure 3.7 Growth law of the field variables - (a) the polarisation and (b) the density in the RFAM, drawn for different disorder strengths. In the disordered environments, the growth deviates from the power-law at late times. 64
- Figure 3.8 (a) Time variation of the effective growth exponent of the polarisation field in the RFAM, shown for different disorder strengths. (b) The scaling collapse of $z_{\text{eff}(P)} - \bar{z}_p$ versus L_p/λ_p . The best fit $z_{\text{eff}(P)} - \bar{z}_p \simeq 0.193(L_p/\lambda_p)^{8.86}$ is shown by the solid line. (c) Disorder dependence of λ_p . The solid line shows a power-law fit $\lambda_p \sim \Delta^{-0.72}$. 66
- Figure 4.1 V versus $1/N_s$ plots in the (a) ordered and (b) disordered state for $\eta = 0.10$. The error bars indicate standard error in mean. The solid lines show the respective algebraic fits. 73
- Figure 4.2 Steady-state snapshots are shown for $\eta = 0.10$, $L = 150$. (a - d) are drawn for $c_r = 0, 0.005, 0.01$ and 0.02 , respectively. The colour bar indicates orientation of the SPPs. The rotators with random intrinsic orientation are not shown for the sake of clarity of the figures. 74
- Figure 4.3 (a) Distribution $P(\phi)$ of the orientation of the SPPs is shown for $\eta = 0.10$ and $c_r = 0.005$. The curves are zoomed into the range $\phi \in [-\pi/2, \pi/2]$ for better visibility. The solid lines show the respective fits with Voigt profile. (b) Plot of the FWHM f of $P(\phi)$ versus N_s . In the presence of quenched rotators, f increases logarithmically with N_s . The dashed lines show respective fits. 75

- Figure 4.4 Plot of orientation distribution $P(\phi)$ of the SPPs for $\eta = 0.40$. In the clean system, *i. e.*, for $c_r = 0$, the system remains in the banded state. As shown in (a), $P(\phi)$ does not change with system size in this state. However, as shown in (b) for $c_r = 0.008$, fluctuation in V increases with system size. Respective fits with Voigt profile has not been shown for the sake of clarity of the plots. 76
- Figure 4.5 (a) Plot of V versus scaled system size N_s/N_s^Γ on log-log scale, where γ is a function of c_r . The data shows good scaling for $0 < c_r \leq 0.0125$, but deviates for $c_r \geq 0.0125$. (b) Plot of shifted FWHM $f - g_1(c_r)$ with scaled system size N_s/N_s^Γ , where both g_1 and Γ are functions of c_r . The scaling holds good for $c_r \leq 0.0125$. 77
- Figure 4.6 (a) Variation of V with c_r shown for different system sizes and $\eta = 0.10$. (b) Variance χ of V plotted with c_r . The peaks in the curves indicate the critical density of rotators $c_{rc}(L)$ for the QLRO-disorder transition for the respective system sizes. (c) V shows good scaling with reduced density of rotators $c(L) = (c_{rc}(L) - c_r)/c_{rc}(L)$ for $c_r \leq c_{rc}$ for all system sizes. The dashed line shows the scaling $V \sim c^{0.287}$. 78
- Figure 4.7 Phase diagram in noise strength versus density of rotator plane. For small c_r , the QLRO state prevails, beyond which the system continuously goes to the disorder state. 79
- Figure 4.8 Plot of average normalised velocity versus noise strength shown for $L = 100$ and different density of the rotators. While V decreases monotonically with increasing η for the clean system, in the presence of the rotators, a certain amount of noise maximizes the ordering. 82

Figure 5.1 Order-disorder transition with noise strength shown for $L = 200$. The clean system shows monotonous transition. The same curve has been drawn in (a) and (b) for the clean system. In the presence of obstacles, (a) and (b) are drawn for $c_o = 0.004$ and 0.040 , respectively. If the obstacles are quenched in nature ($\alpha = 0$), optimal ordering is attained at finite $\eta > 0$. For non-quenched obstacles ($\alpha = 1$), the system shows monotonous transition. Also, for non-quenched obstacles the transition takes place at higher η as compared to the clean system.

92

Figure 5.2 Real space snapshot. The colour bar indicates orientation $\Phi \equiv \theta$ (respectively ϕ) of the SPPs (obstacles). The obstacles are represented by \otimes symbols, and the colour of \times in \otimes indicates ϕ . From left to right, the panels correspond to $\eta = 0.01, 0.20$ and 0.40 respectively. (Top panel) is drawn for the clean system ($c_o = 0$). The ordering decreases monotonously with η for the clean system. Band appears in the right most panel. (Second panel from the top) is drawn for $c_o = 0.006$ with quenched obstacles, *i. e.*, $\alpha = 0$. In this case the system is disordered at low noise, gets ordered at moderate noise, and again gets disordered at high noise (band is destroyed at $\eta = 0.40$). (Bottom panel) is drawn for $c_o = 0.006$ with non-quenched obstacles ($\alpha = 1$). In this case, the system shows monotonous order-disorder transition like the clean system. Again band appears for $\eta = 0.40$. All obstacles are not shown for the sake of the clarity of the figures.

93

Figure 5.3 V versus $1/N_s$ plot on log-log scale for $\eta = 0.10$. (a) In the presence of quenched obstacles, *i. e.*, for $\alpha = 0$, V decreases algebraically with N_s . The solid lines show respective fits. (b) For $\alpha = 1$ and $c_o > 1$, V shows almost no change with N_s . The solid lines show algebraic fits with exponent $\nu < 10^{-3}$.

94

- Figure 5.4 Steady-state orientation distribution of the SPPs shown for $\eta = 0.10$ and $c_o = 0.004$. (a) Width of $P(\theta)$ increases with system size in the presence of quenched obstacles. (b) For non-quenched obstacles $P(\theta)$ does not depend on system size. θ axis has been zoomed into the range $[-\pi/2, \pi/2]$ for better visibility. 95
- Figure 5.5 (a) and (b) show Binder cumulant for $c_o = 0$ and 0.04 , respectively. (b) is shown for $\alpha = 1$. The transition noise η_c is given by the deepest U_L for the corresponding system size L . 96
- Figure 5.6 (a) shows finite size scaling of η_c for different c_o . The dashed lines are the respective quadratic fits. Intercept on η_c -axis gives thermodynamic value of the critical noise strength ($\eta_{c\infty}$). (b) In the presence of the OTAs, $\eta_{c\infty}$ increases monotonously with c_o . 97

LIST OF TABLES

Table 3.1	Parameters \bar{z}_p and λ_p in the RFAM with different Δ values.	67
-----------	--	----

INTRODUCTION

Various aerial displays exhibited collectively by a flock of birds often fascinate us. Similar collective behaviours are observed in shoal of fishes or animal herds of length spanning a few kilometers. On the other hand, micro-organisms like bacteria, motor proteins with associated biofilaments, cytoskeleton of living cells, melanocytes in our skin, *etc.* display analogous collective phenomena in micron scales. Despite the difference in their sizes and biological origins, emergence of such coordinated movement or pattern formation, even in absence of any external drive, seem to be common in all these systems. This ubiquity in their behaviours is a consequence of the similarity in the symmetry and the conservation laws of these systems. These similarities further allow us to treat all these systems on equal footing. *Active matter*, a rapidly growing sub-field of the condensed matter physics, provides such a unified framework to study all these systems, and the constituents of an *active system* are called *self-propelled particles* (SPPs) [1–7]. This sub-field mainly focuses on various mechanical and statistical properties emerging in a collection of SPPs, and specific biological details are not important here. There are also abundant varieties of artificially designed systems, *e. g.*, active colloids [8–10], active polar disks [11], vibrated granular media [12–15], chemically boosted wire-cuts [16] that facilitate experimental studies of the active matter.

1.1 ACTIVE SYSTEMS ARE OUT-OF-EQUILIBRIUM

The active systems are out-of-equilibrium, and their properties are governed by underlying symmetries and conservation laws. Before going into the details of these systems, let us reca-

pitulate the fundamental theories for well-understood equilibrium systems. Let us consider an isolated system separated from its surroundings by an adiabatic wall, so that there is no exchange of matter or energy between the system and its surrounding. The complete description of that system is given by the associated conserved quantities, *viz.*, number of constituting particles, total volume and total energy. These quantities are *extensive* thermodynamic variables as their values depend on the mass of the system. Any number of replicas of the system can be generated by considering other isolated systems of the identical chemical compositions with the same values of the thermodynamic variables. After a sufficiently long time of the system preparation, the replicas statistically exhibit identical macroscopic properties, which do not evolve with time, and the systems are in their *equilibrium states* for the given thermodynamic variables. The equilibrium state can also be determined by another thermodynamic variable, namely *entropy* S . From the concept of the thermodynamics [17] and the statistical mechanics [18, 19], we know that the thermodynamic equilibrium state of a system is a macrostate with the largest possible number of microstates, *i. e.*, the highest entropy.

Now let us focus on a single isolated system and consider it as a collection of two subsystems separated by a fictitious boundary. The nature of the boundary controls the mutual exchange of energy, volume or particles, although these variables are conserved in the whole isolated system. The condition for the thermodynamic equilibrium in these two subsystems is governed by the principle of maximum entropy, which essentially boils down to the equalities of the respective *conjugate* variables, *viz.*, temperature, pressure and chemical potential. These conjugate thermodynamic variables do not depend on the mass of the system, and therefore, these are *intensive* quantities. In general for any arbitrary system, the thermodynamic variables are related to its entropy by an identity

$$dS = - \sum_i X_i dY_i, \quad (1.1)$$

where Y_i 's are the relevant extensive variables, and X_i 's are the respective conjugate variables, intensive in nature.

Let us now redefine one of the above subsystems as a new system and the other one as the surrounding. Moreover, we assume the new system to be separated from the surrounding

by a diathermic boundary, so that only exchange of energy is permitted. The new system is macroscopic in size, but much smaller than the surrounding such that any exchange of energy would leave the surrounding unaltered. Hence, the system is said to be in thermal contact with a *bath* that maintains a fixed temperature. It is then instructive to define the thermodynamic potentials, *i. e.*, free energies [17–19] whose minimisation leads the system to the thermodynamic equilibrium. The global minimum of the free energy surface dictates the equilibrium state for the given parameters, and with the change in a typical parameter, the system goes from one state to another, *i. e.*, phase transition takes place [17, 20]. The free energy changes continuously with the parameter, but its higher order derivative shows discontinuity at the transition point. We call the transition to be *first order* if the first derivative shows discontinuity, whereas it is a *continuous transition* if the second or higher order derivative is discontinuous. Generally, first order transition occurs through nucleation in the system, whereas in the continuous transition, system have large fluctuation, which is manifested by divergence in *susceptibility* [17, 20].

In the equilibrium state the macroscopic properties statistically remain unchanged with time, *i. e.*, a *steady-state* prevails. However, the word ‘equilibrium’ conveys a much more rigorous sense. For example, let us consider a Brownian system – a pollen is dispersed in water kept in a beaker in contact with a constant-temperature bath. Since the pollen is dispersed in a viscous media, naively one would expect its motion to be ceased after sufficiently long time. On the contrary, the particle shows persistent motion because of the random forces experienced from relatively smaller water molecules. Here, the fluctuations in the system balances expected dissipation, and a *fluctuation-dissipation relation* (FDR) [21] exists in the system. Also, the equilibrium criterion of the system demands time-reversal invariance, which invokes the principle of *detailed balance* [21, 22].

Now let us discuss about the active matter. Each bird within a flock flies forward at the cost of its internal energy acquired through nutrition. Therefore, there is constant injection of energy that is transduced to mechanical energy manifesting into a systematic motion. This phenomenon is a defining characteristic of the active matter. As compared to the earlier discussed Brownian motion, here the dissipation of energy is not correlated with the input – there is an incessant input of energy that drives the active system out-of-equilibrium.

There are some studies of the active matter [23–28] that amount to define an ‘effective temperature’ in certain limit of the associated parameters, where the system obeys detailed balance, and an effective FDR can be found. Still the active matters are generally regarded as out-of-equilibrium systems. However, active systems are different from other kinds of out-of-equilibrium systems like a bulk fluid sheared from the top or driven diffusive systems [21]; in active systems, energy is injected at the individual particle level.

The out-of-equilibrium feature of the active systems restrict us from defining an equilibrium state for it, but a non-equilibrium steady-state (NESS) can be defined similar to other out-of-equilibrium systems [21]. When a large population of birds sit for roosting, there is no flock – their arrangement seems to be random. On the contrary, all of the birds move in a globally agreed direction while flying, *i. e.*, flock appears. We can regard this flocked arrangement as a steady-state since there is a steady mass current. Therefore, there is a non-equilibrium order-disorder transition in active systems where the rotational symmetry gets broken. The steady mass current in the active systems could naively be compared with the flow of a viscous fluid, usually described by the Navier-Stokes equations [20], but there is a significant difference between these two types of systems. The active systems are not Galilean invariant, since adding a constant velocity to all the birds changes the phenomenology of the flock [29].

1.2 CATEGORIES OF ACTIVE MATTER

1.2.1 *Polar and apolar*

Self-propelled particles in general possess some intrinsic axes along which they manifest their mechanical activity. For example, an individual bird flies forward along its long axis, whereas melanocyte cell can move forward or backward with equal probability. Therefore, bird-like SPPs possess some polarity along their intrinsic axis, whereas melanocyte-like entities possess a head-tail symmetry. We call the first type a *polar particle* and the latter one an *apolar particle*.

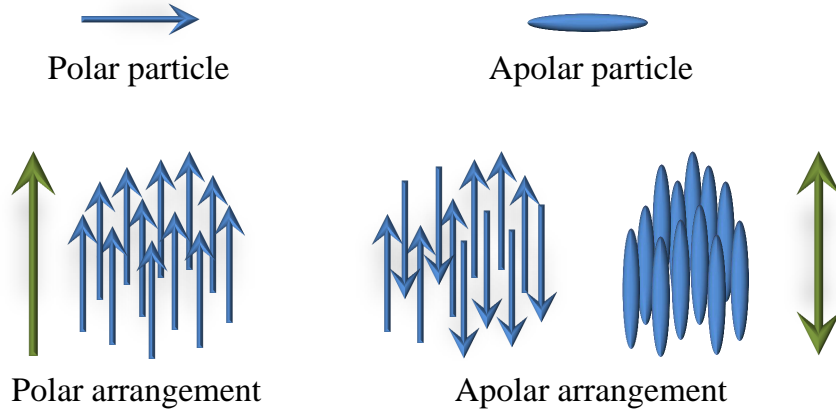


Figure 1.1: A polar (blue arrow) SPP moves forward only, whereas apolar particle (blue ellipse) moves towards its head or tail with equal probability. If a collection of polar particles align parallel to each other, they altogether move towards a director as indicated by the green arrow for the polar arrangement. On the contrary, if the polar particles construct a mutual anti-parallel arrangement, the flock does not have a macroscopic velocity. Similarly a collection of apolar particles aligned parallel to each other does not go anywhere macroscopically. For these apolar arrangements its director (head-tail symmetric green arrow) represents the direction of broken rotational symmetry. For both the polar and the apolar arrangements, the translational symmetry is not broken.

Dynamics of a collection of SPPs depend on the nature of inter-particle interactions. If all the particles in a population of polar SPPs on average tries to align in parallel, we can assign a unit vector, called *director*, for the collection towards which the flock moves. Here the polar particles are said to form a *polar flock*. On contrary, if the inter-particle interaction allows both parallel and anti-parallel alignment of the polar particles, there could be a situation when the collection macroscopically goes nowhere. Here the director \hat{n} represents the direction of broken rotational symmetry of the population and possesses $\hat{n} = -\hat{n}$ symmetry. Hence, we call the system to be in an *apolar* or *nematic* state. The *nematic* state could also be emerged in a collection of apolar particles for parallel alignment interactions. Different states appearing for polar and apolar SPPs are represented in the schematic Fig. 1.1.

1.2.2 *Dry and wet*

In a collection of SPPs moving in a background fluid, each particle loses momentum to the fluid because of the viscous drag offered to it. Although the total momentum of the particles and the fluid remains constant, the momentum is not conserved if only the particles

are considered. Depending on this criterion of momentum conservation, we can categorise active systems as (i) *wet system* – total momentum remains conserved and (ii) *dry system* – total momentum is not conserved. If η represents viscosity of the fluid medium, and γ be the frictional drag experienced by the particles, then in general the effect of the fluid medium on the particle dynamics could safely be neglected beyond a length scale $\sqrt{\eta/\gamma}$. Typically this length scale is very short ranging over only few neighbouring particles. In the studies of the active matter, often we shall focus on the SPPs only. Consequently, the total momentum of the system would not be conserved, and we shall address those as dry active system. However, if the phenomenology demands both the particles and the fluid to be considered as the system, we shall call those as wet active matter. There are indeed many natural systems that are intrinsically wet [1–7], but our focus in this thesis is the dry active system only.

1.3 METHODOLOGY

What could be the framework to study active systems? The active systems, mostly inherited from biological origins, are extremely complex in nature. Mechanical manifestation of the real SPPs are often governed by a large number of other agents, internal or external, the response to which is not always straight forward, rather a bit puzzling. One could certainly use the available techniques for studying other types of out-of-equilibrium systems; however, those techniques are yet to achieve simplicity and versatility of their equilibrium counterparts. Thankfully scientists have managed to prescribe frameworks often borrowed from equilibrium counterparts that could be applicable to the active systems in some limits. Here we shall mention some of the frameworks often used in studies of the active matter.

1.3.1 *Agent-based simulation*

A commonly used technique to study the active systems is to consider a collection of pseudo-particles, and simulate those using computers. In simulations, the dynamics are usually adopted looking at the phenomenology of the concerned active system, and thereafter some approximated interactions are employed depending on the aspects we are interested in. For

example, in the polar systems the interaction should be ‘ferromagnetic’ in nature, whereas for the apolar systems both parallel and anti-parallel interactions are allowed. The volume exclusions are incorporated in system dynamics [30] if we wish the steric interaction to be taken into account. Otherwise, simulations with point particles would suffice for our aim. Other than the exact interactions, ‘errors’ are accounted by relevant noise terms [31, 32]; therefore, stochasticity comes into play. Scientists often adopt Monte-Carlo algorithms [33–35] to deal with stochasticity. Although questions might be raised how an algorithm developed strictly for equilibrium systems could be employed here, in general the coupling of Monte-Carlo algorithm with particle dynamics is such that the detailed balance is violated [33–35].

1.3.2 *Hydrodynamics*

The phenomenology of the active systems could also be described by means of a continuum theory – hydrodynamics [1, 7, 29, 36–38]. For that, one needs to identify the relevant slow variables first. Those slow variables could be obtained from the associated agent-based microscopic models through proper coarse-graining. The next step is to write the time evolution equations for those slow variables where all the terms should be incorporated that are not restricted by the inherent symmetry of the system. Analogous to the prescription for equilibrium systems, the effect of other fast variables are summarised in noise terms. However, here we need not to worry about FDR and detailed balance. Although these equations of motion are usually written following the phenomenology, those could also be derived from the microscopic models. In general, the evolution dynamics of the associated slow variables are expressed by coupled non-linear stochastic partial differential equations (SPDEs), where the coefficients of different terms depend on the parameters of the corresponding microscopic model. Once we succeed in formulating those equations, we can gain information following linearised treatment [29] or other theoretical frameworks like refined mean-field [34, 35] or dynamic renormalisation group approach [29]. One can also simulate those SPDEs numerically [39].

1.3.3 Experiments

As compared to other disciplines of science, in the evolution of the active matter literature, experiment follows theory. One of the major reasons for this could be complexity in working with biologically originated constituents. Although, there are experimental studies for active matter [40–44] with biological ingredients, most of the studies are for artificial imitations [9, 11–15]. Since the theoretical framework for the active systems are yet to attain a generic feature, their results should be compared with the experiments in a qualitative sense. Next, we shall briefly discuss about the characteristics of different types of active systems, mostly in two spatial dimensions unless specified, that have been unveiled so far.

1.4 POLAR SYSTEM

1.4.1 Vicsek Model

The first significant model for a two-dimensional flock of ‘birds’ is given by Vicsek and his collaborators [31]. They model individual bird as point particle that tries to move in the average direction of all the neighbouring particles within a range of ‘influence’. Although this seems like a ferromagnetic spin model [20], here the spins are itinerant in nature. Moreover, while trying to move in the determined average direction, the bird makes some error. The update rules governing the position $\mathbf{r}_j(t)$ and the direction of motion (orientation) $\theta_j(t)$ of the j th particle at time t are as following:

$$\mathbf{r}_j(t+1) = \mathbf{r}_j(t) + \mathbf{v}_j(t), \quad (1.2)$$

$$\theta_j(t+1) = \arg \left[\sum_{k \in R_s} \exp(i\theta_k(t)) \right] + \eta\psi_j, \quad (1.3)$$

where each particle moves with velocity $\mathbf{v}(t) = v(\cos\theta(t), \sin\theta(t))$ of a constant speed v . Each particle interacts with its neighbours within a circle of radius R_s around it. Error in movement is incorporated by an additive noise term ψ chosen from a uniform distribution in $[-\pi, \pi]$. The authors show that for sufficiently high density of particles, the model shows

order-disorder transition with increasing noise strength η . For low η values, all the birds move homogeneously in the same direction on average. For moderately high η values, some dense clustered bands appear in the system, while rest of the system remains disordered (note that no bands were reported in Ref. [31]). On further increment of noise, the birds show no coherent motion. Similar order-disorder transition is also noted with the variation in particle density [31]. Vicsek *et al.* also argue that this order-disorder transition is continuous in nature, and calculate critical exponents for the model in analogy with the standard techniques for the equilibrium systems.

1.4.2 Noise: angular and vectorial

The claim of continuous order-disorder transition in the collection of SPPs is refuted by Chaté and collaborators [32, 45, 46] using a modified VM. Although the position update equation is retained unchanged, the ‘angular noise’ in Eq. (1.3) is replaced by the ‘vectorial noise’ as following:

$$\theta_j(t+1) = \arg \left[\sum_{k \in R_s} \exp(i\theta_k(t)) + \eta n_j(t) \exp(i\psi_j(t)) \right], \quad (1.4)$$

where $n_j(t)$ is the number of neighbours of the j th particle within its interaction range R_s at time t . Compared to the angular noise in the VM, this choice of vectorial noise implies that the birds make error while determining the orientations of their neighbours. Using this modified model, they show that the order-disorder transition in polar SPPs takes place through coexisting states, where high density waves propagates steadily in a disordered background. In analogy of the liquid-gas phase transition through nucleation mechanism, they argue in favour of the first order transition. Moreover, they show that the simple modification in the update rule from Eq. (1.3) to Eq. (1.4) has nothing to do with the nature of transition. Indeed the original VM also exhibits first order transition, provided one considers large enough system size, because the finite size effect is much more dominant for angular noise [31] as compared to the vectorial choice [32]. Although, claims are made that the emergence of an artificial symmetry breaking [47] or way of noise incorporation in the model [48] control the

nature of the transition, now it is more or less settled that this transition is first-order [32, 45, 46] in nature.

1.4.3 Hydrodynamics

For a hydrodynamic description, all we need is to recognise the relevant slow variables and contain the effect of other fast variables in noise terms with appropriate distributions, as mentioned in Sec. 1.3.2. In the dry active systems, the SPPs move on a substrate that hinders particles' motion through frictional forces. Therefore, the only conserved quantity for this system is the number density $\rho(\mathbf{r}, t)$ of the SPPs, as we do not allow the 'birds' to reproduce or die during flight. This field variable could be obtained from the respective microscopic model through proper coarse-graining within a radius R_{cg} as following:

$$\rho(\mathbf{r}, t) = \sum_{j \in R_{cg}} \delta(\mathbf{r} - \mathbf{r}_j(t)). \quad (1.5)$$

The polar orientation of the system could be presented by a polarisation vector field as

$$\mathbf{p}(\mathbf{r}, t) = \frac{1}{\rho(\mathbf{r}, t)} \sum_{j \in R_{cg}} \hat{n}_j(t) \delta(\mathbf{r} - \mathbf{r}_j(t)), \quad (1.6)$$

where $\hat{n}(t)$ represents instantaneous orientation of the SPPs. This is a broken symmetry parameter representing orientational order in the system and is not a conserved quantity. Considering the conservation laws and the symmetries of the polar SPPs as in the VM, hydrodynamical equations of motions (EOMs) for the above mentioned slow variables have first been written by Toner and Tu [29, 49]. Later, those EOMs have been derived with the expressions for the associated coefficients using Boltzmann-equation approach [38, 50, 51]. However, the forms of these coefficients are model specific, and in general depend on the model parameters, *viz.*, density, velocity *etc.* Here we try to obtain the EOMs following the phenomenology, but in a manner that could be easily compared with its equilibrium coun-

terpart. Therefore, we write the EOMs as if the terms arise from a free energy functional \mathcal{F}_p , and add the terms responsible for the out-of-equilibrium aspects separately, as following:

$$\partial_t \rho + v_s \nabla \cdot (\rho \mathbf{p}) = -\nabla \cdot \left(-\frac{1}{\gamma_\rho} \nabla \frac{\delta \mathcal{F}_p}{\delta \rho} + \mathbf{f}_\rho \right), \quad (1.7)$$

$$\partial_t \mathbf{p} + \lambda_1 (\mathbf{p} \cdot \nabla) \mathbf{p} = -\frac{1}{\gamma_p} \frac{\delta \mathcal{F}_p}{\delta \mathbf{p}} + \mathbf{f}_p, \quad (1.8)$$

where v_s represents speed of the SPPs, γ_ρ and γ_p represent kinetic coefficients. The right-hand-side (RHS) of Eq. (1.7) contains two terms – while the first term could be understood as a diffusive current, the second term represents associated noise. To be consistent with the EOMs introduced by Toner and Tu [29, 49], we shall drop both these terms, which is a reasonably good assumption for most of the active systems [1]. As mentioned in Sec. 1.1, the polarisation Eq. (1.8) could be compared with the celebrated Navier-Stokes equation [20]. The coefficient λ_1 has dimensions of speed, and the associated term represents non-linear advection in the system. However, break-down of the Galilean invariance for the SPPs imposes condition $v_s \neq \lambda_1$. This inequality allows the fluctuations in the density and the polarisation fields to convect at different speeds. The noise term \mathbf{f}_p appearing in Eq. (1.8) is generally assumed to be additive, white, and Gaussian with zero mean and delta-correlation

$$\langle f_{p,i}(\mathbf{r}, t) f_{p,j}(\mathbf{r}', t') \rangle = \Delta \delta_{ij} \delta(\mathbf{r} - \mathbf{r}') \delta(t - t'), \quad (1.9)$$

where Δ is a constant, and dummy indices i, j represent Cartesian components.

As compared to the Navier-Stokes equation for simple fluid, the polarisation field defined for the active systems possesses a dual nature. While the polarisation represents a broken-symmetry parameter of the system, $v_s \mathbf{p}$ signifies particle velocity field. This duality of the polarisation field essentially leads many distinction in large scale behaviour of this out-of-equilibrium system, as we shall see later. The Free energy functional for dry polar SPPs could be written as [1, 3]

$$\mathcal{F}_p = \int d^d r \left\{ -\frac{\alpha_1(\rho)}{2} p^2 + \frac{\alpha_2}{4} p^4 + \frac{K}{2} \nabla \mathbf{p} \nabla \mathbf{p} + \frac{w}{2} p^2 \nabla \cdot \mathbf{p} - w_1 \nabla \cdot \mathbf{p} \frac{\delta \rho}{\bar{\rho}} + \frac{A}{2} \left(\frac{\delta \rho}{\bar{\rho}} \right)^2 \right\}, \quad (1.10)$$

where $\delta\rho = \rho - \bar{\rho}$ represents fluctuation in the density field from its average value $\bar{\rho}$. The α_1 and α_2 terms dictate mean-field order-disorder transition in the system as α_1 changes its sign. In general for metric interaction models like VM, one can assume $\alpha_1(\rho) = \left(\frac{\rho}{\rho_c} - 1\right)$, so that α_1 changes its sign at a critical $\rho = \rho_c$. Here we have assumed a one-elastic constant approximation; therefore, the energy cost for a spatially inhomogeneous deformation is represented by the K term, where the Frank constant K is positive. The terms with w 's in Eq. (1.10) are allowed in equilibrium systems also. They represent the density and p^2 contributions to the spontaneous splay [20]. The last term in Eq. (1.10) takes care of the incompressibility of the system. Substituting this expression for \mathcal{F}_p into Eq. (1.8), and using the notations $v_1 = w_1/\gamma_p$ and $\lambda = w/\gamma_p$, we obtain the EOM for the polarisation field as

$$\partial_t \mathbf{p} + \lambda_1 (\mathbf{p} \cdot \nabla) \mathbf{p} = (\alpha_1 - \alpha_2 p^2) \mathbf{p} + K \nabla^2 \mathbf{p} - v_1 \nabla \frac{\rho}{\bar{\rho}} + \frac{\lambda}{2} \nabla p^2 - \lambda \mathbf{p} (\nabla \cdot \mathbf{p}) + \mathbf{f}. \quad (1.11)$$

The gradient of the density term on the RHS of Eq. (1.11) gives gradient of pressure, which appears because of the density fluctuation in the system. This EOM for the polarisation field is similar to the EOM phenomenologically advocated by Toner and Tu [29, 49] with $\lambda_2 = \lambda$ and $\lambda_3 = -\lambda/2$. Although it seems that $\lambda_{1,2,3}$ are mutually related, the exact relation depends on the specific microscopic model. Here, we have considered single elastic constant for the system; however, there could be two more elastic (viscosity) terms appearing in the equation, if we consider explicit contribution from splay and bend deformations [20, 29, 49], as depicted for the apolar system in schematic Fig. 1.2.

The homogeneous steady-state solution of Eq. (1.11) shows that the system remains in a disordered state for $\alpha_1 < 0$ corresponding to the mean density $\bar{\rho} < \rho_c$. On the other hand, for $\bar{\rho} > \rho_c$, *i. e.*, $\alpha_1 > 0$ the system gets ordered with an average polarisation $\bar{p} = \sqrt{\alpha_1(\bar{\rho})/\alpha_2}$. Deep in the ordered state, a linearised study of the EOMs suggests that there exists two decoupled modes of propagation with different speeds [2, 29]. This difference in speed of the sound modes emerges because of the lack of Galilean invariance in SPPs. As compared to the normal fluids where propagation of sound waves are dictated by momentum conservation, the sound modes in the SPPs indicate spontaneously broken symmetry of the system. If we approach the mean-field transition from the ordered state, near the transition the system

turns linearly unstable, and therefore, solitary waves propagates in the form of bands [32, 39, 46, 51].

In the active systems, the density field is coupled with the polarisation by means of their EOMs. This coupling introduces anomalous number fluctuation [1, 3] in these systems, as compared to their equilibrium counterparts. For a given system, its number fluctuation is related to its static structure factor $S(q)$ through the relation

$$\lim_{q \rightarrow 0} S(q) = \frac{(\Delta N)^2}{\langle N \rangle}, \quad (1.12)$$

where \mathbf{q} represents wave vector, N is the instantaneous number of particles in a region of size V , $\langle N \rangle$ is its average over time, and $\Delta N = \sqrt{\langle N^2 \rangle - \langle N \rangle^2}$ represents the standard deviation. A linearised study of the EOMs for the polar SPPs would give us the static structure factor as

$$\begin{aligned} S(\mathbf{q}) &= \frac{1}{\bar{\rho}V} \langle \delta\rho_{\mathbf{q}}(t) \delta\rho_{-\mathbf{q}}(t) \rangle \\ &= \mathcal{A}(\theta) \frac{1}{q^2}, \end{aligned} \quad (1.13)$$

where only the first order significant terms have been retained in the calculation. The coefficient \mathcal{A} depends on the system parameters as well as the angle between flocking direction and \mathbf{q} [1, 3, 29]. For $\theta = 0$, $\mathcal{A}(\theta) = 0$, and therefore higher order corrections are necessary there. Otherwise, this $1/q^2$ divergence seems to be quite omnipresent for active systems [1, 3, 29, 49], and does not even depend on the dimensionality d of the system; though \mathcal{A} depends on d . The shortest wave vector in an active system could fairly be assumed of the order of the inverse of system size $V^{-1/d}$, and therefore of the order $\langle N \rangle^{-1/d}$. Then Eq. (1.13) suggests $\lim_{q \rightarrow 0} S(q) \sim \langle N \rangle^{2/d}$ for the active systems. Combining this expression with Eq. (1.12), we obtain

$$\Delta N \sim \langle N \rangle^{\frac{1}{2} + \frac{1}{d}}, \quad (1.14)$$

i. e., there exists *giant number fluctuation* (GNF) in the active systems. Although, we have introduced the concept of GNF for the polar SPPs, it is a common characteristic of both polar and apolar active systems, and it was first predicted for the apolar system [36, 52].

The expression for the static structure factor for polar SPPs as in Eq. (1.13) is analogous to that for the XY model [20]. Therefore, one may naively expect existence of quasi-long range order in the polar SPPs. However, for two-dimensional polar SPPs, effect of the neglected non-linearities are quite relevant. Those non-linearities suppress the fluctuation in the system, so that, for $q \rightarrow 0$, divergence of $S(q)$ is slower than $1/q^2$. This establishes true long range order (LRO) in the polar SPPs. Note that we are discussing about the presence of LRO in a two-dimensional system that may sound like violation of the Mermin-Wagner theorem [53]. However, the SPPs construct out-of-equilibrium system where this theorem is not satisfied. In fact, the polar SPPs themselves carry information from one subflock to the other, which is faster as compared to the diffusive transport of informations [29] in usual equilibrium systems in two dimensions. This convective nature of the particles induces true LRO in these systems.

1.4.4 *Active Ising model*

Apart from the systematic studies of the polar SPPs through simulations of Vicsek-like models or the hydrodynamic analysis of the respective coarse-grained EOMs [29, 31, 32, 38, 46, 49–51], another interesting approach to understand flocking phenomena minimally has been introduced by Solon and Tailleur [34, 35]. In analogy of the Ising model for equilibrium systems [20], they introduce an out-of-equilibrium version of the same model, namely *Active Ising Model* (AIM). In the AIM, both the self-propulsion characteristics and the alignment interactions of the SPPs have been taken care of. However, as compared to the continuous rotational symmetry of the SPPs in Vicsek-like models, here the particles possess discrete rotational symmetry – each particle possesses ‘spin’ $+1$ or -1 . They consider a square lattice, and the Active Ising Spins (AISs) can sit on its vertices. There is no volume exclusion interaction; therefore, any number of AISs can sit on a single site. The AISs move to their right and left sites with different probabilities depending on their spins. In the vertical direc-

tion, they perform diffusive movement. Each AIS tries to get aligned with all other AISs on the same site. The dynamics of the system is controlled by the density of the particles and the ambience temperature (comparable to the noise term in the VM). For this model and an associated refined mean-field model (RMFM), they argue that the flocking phenomena could also be understood as gas-liquid transition – (i) at high temperature and low density, the system does not form flock, which could be compared with a gaseous state; (ii) for low temperature and high density, the AISs align and flow like a liquid; (iii) in between this two regimes, bands travel with disordered background.

1.4.5 Experiments

Here we briefly discuss some of the interesting experimental studies for the polar SPPs. As already mentioned in Sec. 1.3.3, the results of these experiments should be compared with the theoretical predictions only qualitatively.

Schaller *et al.* perform an *in vitro* experiment [54] with actin filaments propelled by one type of motor protein, namely heavy meromyosin. They keep the motor proteins attached to the substrate that drive the thread-like filaments through treadmilling mechanism. Some of the filaments are fluorescently labelled to visualise their alignment. They show that below a certain density of the filaments, individual filaments perform persistent random walk. Therefore, the system remains in a disordered state analogous to the disordered state observed in the Vicsek model. However, if the density of the filaments is higher than its critical value, then these threads show coherent motion. For further increment in density, wave-like structures appear in the system. Through another following experiment [55] they argue the importance of long ranged interactions on the stability of the patterns appearing in the system.

A similar experiment was preceded by Szabó *et al.* [56] where they look for order-disorder transition in a collection of keratocytes (tissue cells) extracted from fish scales. For initial collection of the cells with low density, random motility is observed. However, with the cell division in the course of time, *i. e.*, increase in density over a threshold value, the cells exhibit cooperative movement. Motivated by this experiment, they introduce a numerical

model which advocates for continuous order-disorder transition in the system. Although such a conclusion could not be drawn from the poor data quality of this experiment, we must realise the qualitative agreement of their results with the earlier described theoretical prescriptions.

While experiments with biological constituents seem to be complicated because of required controlling protocols, experimentalists often find it easy to work with artificially designed SPPs [11, 14–16, 57–59]. Paxton *et al.* [16] devised polar SPPs using rod-shaped micron-sized gold-platinum wire-cuts, which propels toward the platinum end because of the emerged chemical imbalances on aqueous hydrogen peroxide solution. A more celebrated technique of devising polar SPPs is by assigning anisotropy either in shape or in mass distribution of small rods. Kudrolli *et al.* considered a collection of cylindrical entities having mass anisotropy [58], and placed those on a plane substrate that has been vibrated vertically with certain frequency and a driving acceleration. Here the driving acceleration of the shaker is analogous to the ambient noise introduced in the Vicsek-like models [31, 32]. Above a threshold driving acceleration, each rod moves towards its lighter end since the heavier end encounters more frictional force from the substrate. With the increment of driving acceleration, the rods tend to accumulate near the boundary of the substrate. However, with further increase in the acceleration, the accumulation turns less pronounced because of higher noise. They argue that the cylindrical shape of the entities is the reason behind the accumulation near the boundary, since spherical particles do not exhibit similar tendency. They also characterise presence of large number fluctuation in the system. To avoid accumulation tendency of polar SPPs near the wall, petal geometry has been incorporated in later experiments [11, 15, 59]. In Ref. [11], Deseigne *et al.* consider a collection of circular disks with anisotropic base. While the circular geometry suppresses nematic alignment, in-built polarity induces directed motion on the vibrated substrate. With this experimental setup, they show onset of collective motion with varying vibration amplitude. They also report large number fluctuation with scaling constants qualitatively in agreement with theoretical prescriptions. Following this they perform another experiment and introduce a numerical model for the vibrated polar disks [59], from which they confirm the existence of true long range order in two-dimensional polar SPPs. In an ingenious experiment [15], Kumar *et al.* show that coher-

ent motility could be achieved by a collection of vibrated granular rods, provided those rods interact through passive spherical beads, and the motility could be increased with increasing density of passive beads. This experiment provides a new mechanism for carrying cellular cargo particles. As compared to the electrically energised spherical polar SPPs in Ref. [9], the motility of the polar rods in Ref. [15] could be controlled by tuning the concentration of the ‘compressible fluid’ of passive beads in the background.

1.5 APOLAR SYSTEM

The choice of the broken symmetry parameter for the apolar (nematic) systems is little more subtle as compared to the polar systems. A system with nematic order must be invariant under the inverse transformation of the director, *i. e.*, $\hat{n} \rightarrow -\hat{n}$. Therefore any vector quantity, like polarisation in the polar case, would not be eligible for the choice; rather a second rank tensor would serve the purpose. Moreover, that tensor should be symmetric and traceless since it must yield zero in the isotropic disordered state. In general for two dimensional nematic systems, the tensor order parameter [20, 60] is defined as

$$\mathbf{Q}(\mathbf{r}, t) = \frac{S}{2} \begin{pmatrix} \cos 2\theta(\mathbf{r}, t) & \sin 2\theta(\mathbf{r}, t) \\ \sin 2\theta(\mathbf{r}, t) & -\cos 2\theta(\mathbf{r}, t) \end{pmatrix}, \quad (1.15)$$

where θ represents orientation of the coarse-grained director $\hat{n}(\mathbf{r}, t) = (\cos \theta(\mathbf{r}, t), \sin \theta(\mathbf{r}, t))$. Here we have restricted ourselves to the discussion of uniaxial nematics only. Ordering of such systems is generally quantified by the positive eigenvalue S of \mathbf{Q} , while the associated eigenvector represents orientation of the global director.

1.5.1 Microscopic model

Following the Vicsek model for the polar SPPs, Chaté *et al.* introduce a similar model for active nematics [61]. They consider a collection of point particles, where any arbitrary particle j possesses an intrinsic orientation $\theta_j(t) \in [-\pi/2, \pi/2]$, so that $\theta_j \equiv -\theta_j$. At every time step,

the particle travels a fixed distance either along θ_j or $\theta_j + \pi$ with equal probability. At every time step θ_j is updated to the orientation of the eigenvector $\Theta_j(t)$ corresponding to the positive eigenvalue of the local tensor order parameter $\mathbf{Q}_j(t)$. $\mathbf{Q}_j(t)$ is calculated from the orientations of all neighbouring particles k within a fixed interaction range R_s of the j th particle. However, ambient noise perturbs the expected update:

$$\theta_j(t+1) = \Theta_{k \in R_s}(t) + \eta \psi_j, \quad (1.16)$$

where $\psi \in [-\pi/2, \pi/2]$ is an additive delta-correlated white noise, and noise strength $\eta \in [0, 1]$. They show that with the variation of noise strength, the system shows continuous order-disorder (nematic to isotropic disorder state) transition. This transition is similar to the Berezinskii-Kosterlitz-Thouless (BKT) transition [20] observed in equilibrium systems, and the system remains in a QLRO state for the nematic alignment. However, active nematic is different from its equilibrium counterpart because of the presence of GNF in the earlier system, as Chaté *et al.* show by their numerical simulation [61]. The existence of GNF in the active nematics was earlier predicted by Ramaswamy *et al.* [36, 52] from the hydrodynamic theory.

1.5.2 Hydrodynamics

Similar to the polar system, here we introduce EOMs for the relevant hydrodynamic variables of the apolar system. Since the number of particles is conserved, the coarse-grained density $\rho(\mathbf{r}, t)$, as defined in Eq. (1.5), is a conserved field variable. The broken symmetry variable representing ordering in the apolar system is given by a coarse-grained tensor field $\mathbf{Q}(\mathbf{r}, t)$ with components

$$Q_{lm}(\mathbf{r}, t) = \frac{1}{\rho(\mathbf{r}, t)} \sum_{j \in R_{cg}} \left(\hat{n}_{jl}(t) \hat{n}_{jm}(t) - \frac{1}{2} \delta_{lm} \right) \delta(\mathbf{r} - \mathbf{r}_j(t)), \quad (l, m = 1, 2). \quad (1.17)$$

The conservation criterion for the number of particles governs the EOM for $\rho(\mathbf{r}, t)$ as

$$\partial_t \rho = -\nabla \cdot \left(-\frac{1}{\gamma_\rho} \nabla \frac{\delta \mathcal{F}_Q}{\delta \rho} + \mathbf{f}_\rho + \mathbf{J}_a \right), \quad (1.18)$$

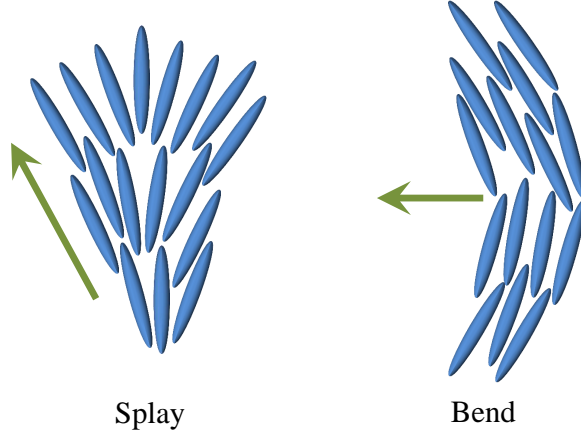


Figure 1.2: Though active nematic does not have any macroscopic velocity, splay or bend arrangement of the apolar particles introduces local polarity as indicated by the arrows. This local polarity induces local particle current proportional to the local curvature of the configuration.

where \mathcal{F}_Q is the nematic free energy functional discussed below. Note that, as compared the density Eq. (1.5) for the polar case, no convective term appears on the left hand side (LHS) of Eq. (1.18), since there is no drift velocity in the active nematic [1, 3]. However, because of the splay and bend arrangement of the apolar SPPs, a local current J_a emerges in the system, as shown in schematic Fig. 1.2. This local current is proportional to the curvature of the arrangement, specifically, $J_a \propto \nabla \cdot \mathbf{Q}$. Since our main focus is two-dimensional systems, we do not discuss about the twist deformation, which would be present in higher dimensions [20, 29]. Appearance of such active current introduces many anomalous characteristics in the apolar system [1, 3, 36].

The EOM for the order parameter field is given by

$$\partial_t \mathbf{Q} = -\frac{1}{\gamma_Q} \frac{\delta \mathcal{F}_Q}{\delta \mathbf{Q}} + f_Q, \quad (1.19)$$

where the effect of different fast variables has been summarised in the random noise term f_Q , and γ_Q represents rotational viscosity appearing because of friction from the substrate.

Thermodynamics of the nematic system in two-dimensions is governed by the free energy functional [1]

$$\mathcal{F}_Q = \int d^d r \left\{ -\frac{\alpha_1(\rho)}{2} \mathbf{Q} : \mathbf{Q} + \frac{\alpha_2}{4} (\mathbf{Q} : \mathbf{Q})^2 + \frac{K_Q}{2} (\nabla \mathbf{Q})^2 + C_Q \mathbf{Q} : \nabla \nabla \frac{\delta \rho}{\bar{\rho}} + \frac{A}{2} \left(\frac{\delta \rho}{\bar{\rho}} \right)^2 \right\}, \quad (1.20)$$

where Frobenius inner product $A : B = A_{lm} B_{lm}$. The first two terms of the integrand appearing on the RHS of Eq. (1.20) govern mean-field order-disorder transition. The system orders nematically for $\alpha_1 > 0$, provided $\alpha_2 > 0$. The third term represents Frank free energy density where the Frank constant K_Q is positive. The coupling between the density and the order parameter fields is taken care by the fourth term, and the last term represents energy cost because of fluctuation in the density. Injection of the expression for \mathcal{F}_Q from Eq. (1.20) into Eq. (1.19) would give us the explicit EOM for \mathbf{Q} similar to the equation phenomenologically introduced by Ramaswamy *et al.* [36]. The EOMs for ρ and \mathbf{Q} could also be derived following Fokker-Planck approach [62] or through proper coarse-graining of microscopic models [37].

Linearised study of the EOMs for the active nematic suggests that the system shows order-disorder transition with the variation in noise and density, *i. e.*, in the (f_Q, ρ) plane [37]. The solutions are linearly stable for deep in both the ordered regime (low f_Q and/or high ρ) and the disordered regime (high f_Q and/or low ρ). However, near the transition, the solutions are linearly unstable, around which band-like structures appear in the system. This instability was first predicted by Shi and Ma [62]. The appearance of bands suggests coexistence of ordered and disordered domains near the transition; therefore, the transition is expected to be discontinuous in nature, contrary to the prediction from the microscopic model described in Sec. 1.5.1.

Existence of GNF in the active nematic could also be understood from the EOMs of the slow variables. Considering a small perturbation around a steady-state homogeneous ordered solution, one may check that in linearised approximation the static structure factor is given by $S(q) \sim 1/q^2$. Therefore, in two spatial dimensions, number fluctuation $\Delta N \sim N$, which is in agreement with the available studies for active nematics [1, 3, 36, 37]. Because of this GNF, the active nematics are intrinsically phase separated, as confirmed by Mishra *et al.* through a lattice model study [33].

In this thesis, we do not discuss about the active nematics consisting of polar SPPs. However, one can find extensive studies for those systems in the literature [63–65].

1.5.3 Experiments

Apolar SPPs are available in nature that form active nematic under suitable condition; human melanocytes that distribute colour pigments in our skin, human fibroblasts which is a common cell of connective tissues, and human osteoblasts are few such examples. These cells are usually anisotropic in shape, and the mutual communication amongst these cells is usually established through steric repulsion and some external drives, *viz.*, chemotaxis or galvanotaxis. In Ref. [42], Gruler *et al.* show that, melanocytes remain in isotropic disordered state under weak external drives. As the external drive turns stronger, melanocytes form nematic state similar to equilibrium liquid crystalline [60], but are active in nature. In Ref. [41], Kemkemer *et al.* show the appearance of $\pm 1/2$ disclinations [20] in the nematic state of melanocytes, and characterise splay and bend elastic constants for the system. Appearance of such disclinations is crucial for nematic states, and has also been observed in experiment on microtubules [66–68]. There are also many theoretical and numerical studies for the characterisation and dynamics of these disclinations in the active nematic [30, 68–71]. Although these experiments characterise isotropic-nematic transition for apolar active systems, existence of GNF is yet to be verified for these type of biological systems.

Other than biological entities, experimentalists also use artificial apolar rods to study active nematic, where a continuous vibration of the container (substrate) acts as the source of energy. In Ref. [12], Narayan *et al.* use apolar rod-like constituents of different shapes and show that particle shapes play a major role in pattern formation. In a following experiment [13], they provide experimental evidence of GNF in the nematic state of apolar active particles. There they also confirm the earlier theoretical prediction of long-time tail in auto-correlation [13, 36]. In Ref. [14], Blair *et al.* report about different types of vortices appearing in a collection of granular rods vibrated vertically and horizontally.

1.6 COARSENING

In this section, we discuss about *coarsening* or *phase ordering kinetics* of different systems. Given a parameter space, the equilibrium state of a system is determined by the global minimum of the associated free energy. Let us consider a system in a disordered state at a high temperature and quench it rapidly to a low temperature so that the corresponding equilibrium state would be an ordered one. Though the system will achieve that ordered state, but not immediately. By the term ‘coarsening’, we refer how the system evolves from that disordered state to the ordered state after a rapid quench. Obviously, coarsening is an out-of-equilibrium process since the system evolves with time. However, let us first discuss about the coarsening of systems approaching equilibrium states [72, 73], and thereafter, we focus on the active systems.

1.6.1 Coarsening towards an equilibrium state

Let us first consider a magnetic substance evolving from para-state to ferro-state after a rapid quench of temperature T below its critical value T_c . There will be domains of ‘up’ and ‘down’ spins competing for an ‘all up’ or ‘all down’ state for a finite system. this evolution takes place through Glauber dynamics [74], *i. e.*, random particle flips its spin to achieve the global minimum of the free energy. Consequently, the magnetisation does not remain conserved. We distinguish this as a class of systems for which the associated order parameter is not conserved. Contrary to this class, the order parameter remains constant in a binary mixture. For $T > T_c$, the mixture remains in a homogeneous state, whereas for $T < T_c$, the system gets phase separated in the equilibrium state. After a rapid quench from $T > T_c$ to $T \ll T_c$, the system evolves through local exchange of the two species. Note, this is different from the Glauber dynamics, since the relative composition of the two species has to be kept fixed in this case. For this mixture, the order parameter is measured by the difference in the number of entities of these two species, and it remains conserved throughout the evolution. This type of evolution through species exchange in binary mixture or analogous class of systems is known as Kawasaki dynamics [75]. In both the cases, the evolution takes place through the

dynamics of domain walls or topological defects. Next, using phenomenological free energy approach we try to understand the evolution dynamics of the order parameter for both the cases described above.

Suppose, for a system, a scalar order parameter field $\phi(\mathbf{r}, t)$ is defined in the coarse-grained limit. The ordered state of the system could be typically represented by a Landau-Ginzburg free-energy functional

$$\mathcal{F}[\phi] = \int d^d r \left\{ f(\phi) + \frac{1}{2} K (\nabla \phi)^2 \right\}, \quad (1.21)$$

where $f(\phi)$ is a polynomial in ϕ representing the local free-energy, and the K term represents energy cost for the domain interface, *i. e.*, topological defect. Evolution dynamics of $\phi(\mathbf{r}, t)$ in a system with *non-conserved order parameter* is given by a time-dependent Ginzburg-Landau equation

$$\partial_t \phi(\mathbf{r}, t) = -\frac{1}{\gamma} \frac{\delta \mathcal{F}}{\delta \phi} + \psi(\mathbf{r}, t), \quad (1.22)$$

where γ represents damping coefficient, and ψ is a random noise. Since the system will eventually settle to an equilibrium state, γ and ψ are correlated by a FDR. Compared with this, the evolution dynamics for the *conserved order parameter* case is given by a Cahn-Hilliard-Cook equation

$$\partial_t \phi(\mathbf{r}, t) = \nabla \cdot \left\{ D \frac{\delta \mathcal{F}}{\delta \phi} + \psi(\mathbf{r}, t) \right\}, \quad (1.23)$$

since diffusion of the ingredient species is the prime mechanism of evolution. The diffusivity D is again related with the noise term. As per the categorisation by Hohenberg and Halperin [76], Eqs. (1.22) and (1.23) represent *Model A* and *Model B*, respectively.

One interested only in the coarsening problem can safely neglect the noise terms in Eqs. (1.22)-(1.23) [77–79], and understand the processes by solving their deterministic parts. Rather than going for a rigorous calculation, here we try to understand the coarsening processes through intuitive arguments. In both the conserved and the non-conserved cases, the coarsening takes place through emergence and growth of domains. Although the domain in-

creases in size in the course of time, its configuration statistically remains the same. This fact could be realised by checking for dynamical scaling of the equal-time two-point correlation function [20, 72, 73]

$$C_\phi(\mathbf{r}, t) = \langle \phi(\mathbf{r}_0, t) \phi(\mathbf{r}_0 + \mathbf{r}, t) \rangle. \quad (1.24)$$

Characteristic length L_ϕ of the domains are usually defined as the distance over which $C_\phi(\mathbf{r}, t)$ drops to 1/2. Existence of the dynamical scaling infers that the coarsening is governed by a single dominant scale, and L_ϕ is a typical measure of that scale. Growth law for the system, *i. e.*, time dependence of L_ϕ could be understood by the ‘motion’ of the associated defects (domain walls in this case with scalar $\phi(\mathbf{r}, t)$). For a system with *non-conserved order parameter*, the effective velocity of the domain wall should be equal to its curvature. Now the wall velocity $\sim dL_\phi/dt$, and the curvature $\sim 1/L_\phi$, and equating those we obtain $L_\phi \sim t^{1/2}$. For the system with *conserved order parameter*, a similar but more subtle argument has been provided by Huse [80]. In this case the system evolves through nucleation and growth of the component present in a vanishing fraction in a small neighbourhood. Therefore, surface tension has a major role to play which effectively gives local concentration current $\sim D\sigma/L_\phi^2$, σ being the surface tension. This current equated to wall velocity gives $L_\phi \sim t^{1/3}$.

So far in this section, we have discussed about scalar $\phi(\mathbf{r}, t)$ only. However, for systems like superconductor, nematic liquid crystal, *etc.* we need n -component vector order parameters [72]. One of the very interesting case for this class is $d = 2 = n$, where $L_\phi \sim \left(\frac{t}{\ln t}\right)^{1/2}$ for a vector order parameter field $\boldsymbol{\phi}(\mathbf{r}, t)$ in two-dimensions [72, 73]. In this case, the topological defects are vortices, not domain wall.

Although our discussion about coarsening revolves around growth laws for characteristic length extracted from equal time two-point correlation, the usually measured quantity in experiments is structure factor $S_\phi(\mathbf{k}, t) = \int d^d r e^{i\mathbf{k}\cdot\mathbf{r}} C_\phi(\mathbf{r}, t)$, where \mathbf{k} represents wave-vector. This structure factor provides information about the morphology of the domain walls [72, 73]. Moreover, if the structure factor follows dynamical scaling of the form

$$S_\phi(\mathbf{k}, t) = L_\phi^d f(kL_\phi), \quad (1.25)$$

then near the interface, *i. e.*, for $kL_\phi \rightarrow \infty$, the scaled structure factor follows

$$f(kL_\phi) \sim (kL_\phi)^{-(d+n)}. \quad (1.26)$$

This is called generalised Porod's law.

1.6.2 Coarsening in active systems

The physics of the active systems is significantly different from that of usual equilibrium systems. Motivated by this fact Dey *et al.* [81] investigate coarsening of the coarse-grained density field $\rho(r, t)$ for different types of microscopic active models [31, 32, 46, 61, 63]. They show that all those active models exhibit non-Porod behaviour. Similar conclusion has earlier been made by Mishra *et al.* for active nematic [33] and active polar system [39]. Compared to earlier prediction of the growth law $L_\rho \sim t^{5/6}$ [2, 82], Dey *et al.* [81] propose existence of another length scale $L_\rho \sim t^{0.25}$ for the polar system.

Phase separation kinetics for Brownian type of particles, but with an integrated activity degrees of freedom (active Brownian particle) is studied by Stenhammer *et al.* [83], and they show that this kinetics is not very different from its equilibrium counterpart. In a similar spirit, Wittkowski *et al.* [84] introduce an 'Active Model B' and study phase-separation kinetics for it. As the name suggests, this is a Model B with activity associated with it. In spite of all these studies, a generalised understanding of phase ordering kinetics for the active systems is still very poor compared to their equilibrium counterparts. Therefore, we need to study coarsening in active systems in much more detail.

1.7 EFFECT OF INHOMOGENEITY

In the previous sections, we have discussed about systems, equilibrium or otherwise, that are *clean* in composition; there were no inhomogeneity present. In reality, such systems could hardly be found since inhomogeneity, *i. e.*, presence of impurity or disorder, is an inevitable fact of nature. Presence of such inhomogeneities induces substantial change in the system

characteristics like equilibrium state, phase transition, scaling laws, ordering kinetics *etc.* [85–92]. In general, the inhomogeneities are of two types: (i) *quenched* – the random parameters defining the characteristics of the inhomogeneity do not change with time and (ii) *annealed* – the random parameters evolve with time. As compared to the quenched case, annealed inhomogeneities achieve thermal equilibrium in experimental time scales. Therefore, their effect could be incorporated in the statistical description of the clean system with modified parameters [93, 94]. However, the situation is not so straight forward with quenched inhomogeneities; therefore, we mostly focus on the quenched case. In the last five decades, there have been extensive studies for understanding the effects of inhomogeneities on systems, mostly in equilibrium or approaching towards it. Recently, scientists have also started to look for inhomogeneous active systems [95–99]. In this section, we first discuss effect of inhomogeneities on *non-active* (mostly equilibrium) systems, and then provide a brief review for inhomogeneous active systems.

1.7.1 *Non-active systems with inhomogeneity*

Let us consider a clean magnetic system represented by the Ising model [18–20]. The Hamiltonian of the system consists of a spin-spin interaction term with a strength ϵ and a field-spin interaction term in presence of some external field h . The equilibrium configuration of the system is determined by this Hamiltonian for temperature T below a critical value T_c , and the system remains in ferromagnetic state, provided $\epsilon > 0$. On the contrary, for $T > T_c$, the equilibrium state is dominated by the entropic part of the free energy, and the system attains paramagnetic state. However, this simple phenomenology is not accurate for all spatial dimensions, since there exists a lower critical dimension d_l so that, for any dimension $d \leq d_l$, thermal fluctuations make the ordered state unstable. For Ising model, which could be regarded as a special case of $O(n)$ model with $n = 1$ [20], $d_l = 1$. For $O(2)$ model, *i. e.*, XY model, the lower critical dimensionality is 2, above which a broken-symmetry state with long range order can be sustained. In the marginal case of $d = 2$, BKT state emerges in the XY model [20, 88].

Now suppose the system is not clean, rather some non-magnetic or other kind of magnetic molecules replace the original spins. This scenario with quenched inhomogeneities could be tackled by the Ising model (in the simplest case) with non-uniform exchange interactions, *i. e.*, ϵ is not same throughout the whole system. This modified description, commonly known as *random bond Ising model* (RBIM) in literature, has been used extensively to study inhomogeneous systems. An alternative way to study inhomogeneous systems is to regard ϵ to be uniform everywhere, but the external field h to be non-uniform. In literature, this description is known as *random field Ising model* (RFIM). For both these models, the lower critical dimension is 2, and even in the marginal case of $d = 2$, the ordered state is unstable [88]. As compared to the Ising case, $d_l = 4$ for systems with continuous symmetry like XY model [85]. Quenched inhomogeneities can also induce a much complicated scenario compared to RBIM and RFIM, *viz.*, spin glass [90, 100], which we do not discuss here.

Scientists have also studied the effect of quenched inhomogeneities on coarsening of non-active systems. In Ref. [91], Corberi *et al.* have studied RBIM with Glauber dynamics, and shown that there is a crossover in growth law from power law to logarithmic growth. Later, they draw a similar conclusion for RFIM [92]. In both the cases superuniversality [20] is found not to hold. In a recent study [101], coarsening in RFIM has been studied for Kawasaki dynamics.

1.7.2 Active systems with inhomogeneity

It is only recently that scientists have started to look for the effect of inhomogeneities on active systems [102]. In a surprising work, Chepizhko *et al.* [95] show that, in presence of inhomogeneities, a certain amount of noise facilitates optimal flocking of the polar SPPs! This is something counter intuitive, since one would naively expect more ordering with less noise. However, since the self-propulsion nature of the SPPs is the principal reason of true long range order in two-dimensions, presence of inhomogeneities hinder the mutual information transport within the sub-flocks. Therefore, the system needs an optimal noise to overcome those hindrance and establish order in the system. In Ref. [98], Quint and Gopinathan report swarming phase transition on a two-dimensional percolated lattice in presence of topological

inhomogeneities. Sándor *et al.* introduces different type of dynamic states of SPPs in presence of quenched inhomogeneities [99]. In an experiment with artificial SPPs, Morin *et al.* show that, in presence of high density inhomogeneities, the flock becomes extremely tortuous and gets destroyed [97]. In Ref. [96], Yllanes *et al.* consider two species of SPPs with different ‘intentions’, and show that the flock of one species could easily be destroyed by a few number of other species.

1.8 OBJECTIVE AND ORGANISATION OF THIS THESIS

The previous sections highlight about developments in the field of active matter, polar or apolar, and provide comparison with the well understood systems, mostly in equilibrium. With these understanding as the basis, we have unveiled further aspects of the active systems that have been organised in the following chapters. In Chapter 2, we introduce a minimal lattice model for active nematic comprised of apolar SPPs, and construct a phase diagram in temperature versus density plane. In Chapter 3, we study coarsening of polar SPPs in clean as well as inhomogeneous environment. In Chapter 4, we discuss about the absence of long range order in two-dimensional polar SPPs in presence of quenched inhomogeneities. In Chapter 5, we propose a mechanism for better and robust flocking in inhomogeneous environment, following which, we conclude this thesis in Chapter 6.

A LATTICE MODEL STUDY OF ACTIVE NEMATIC

2.1 INTRODUCTION

Theoretical studies of the active nematic are mostly done by using the relevant hydrodynamic equations of motion (EOMs) [36, 37, 62, 68–71, 103], microscopic rule based simulation of point particles [61] or Brownian dynamics simulation [30]. These studies indeed provide significant understanding of the active nematic, *e. g.*, order-disorder transition in the density-temperature plane, presence of long-wavelength instability near the transition, GNF in the nematic state, associated defect dynamics, *etc.* However, study of lattice models is in general interesting for development of simplified theories, and it often provides insight into complex systems. In this chapter¹, we introduce a lattice model for a two-dimensional active nematic, explore various states of the system in the density-temperature plane, and compare it with the corresponding equilibrium model. Our model is similar to the Active Ising model discussed in Chapter 1.4.4 for the polar system [34, 35]; but we include volume exclusion that often introduces interesting features like typical pattern formation [104, 105] or density induced motility [106] in the system.

This chapter is organised as follows. In Sec. 2.2 we define the lattice model for the active nematic and its equilibrium counterpart. Details of the numerical simulations are presented in Sec. 2.3. We construct a phase diagram for the active nematic in the density-temperature plane, as presented in Sec. 2.3.1. There we note – (i) disordered isotropic (I) state in low density regime, (ii) locally ordered inhomogeneous mixed (IM) state in intermediate density

¹ The work reported here is based on the paper “Order-disorder transition in active nematic: A lattice model study”, Rakesh Das, Manoranjan Kumar and Shradha Mishra, Scientific Reports 7, 7080 (2017).

regime, and (iii) bistability between the IM and a homogeneous globally ordered (HO) state in high density regime. In contrast to the continuous isotropic to nematic (I-N) transition in the equilibrium model, the I to IM state transition in the active nematic in the low temperature regime occurs with a jump in order parameter. This transition occurs at a density lower than its critical value in the equilibrium model, and the system forms clear bands (BS) in this regime. Different states appearing in the active nematic and the corresponding equilibrium nematic are characterised by a two-point orientation correlation in Sec. 2.3.2. Orientation fluctuation in the states corresponding to the high density limit are characterised in Sec. 2.3.3. We justify the jump in the order parameter and the shift in the transition density in the active model by analysing their coarse-grained hydrodynamic EOMs in Sec. 2.4. We close this chapter with a brief summary of results and concluding remarks in Sec. 2.5.

2.2 MODEL

We consider a collection of apolar self-propelled particles (SPPs) on a two-dimensional (2D) square lattice, as shown in schematic Fig. 2.1(a). Occupation number ' n_i ' of the i^{th} lattice site can take values 1 (occupied) or 0 (unoccupied). Orientation θ_i of apolar particle at i^{th} site can take any value between 0 and π . The model follows two sequential processes at every step; first, a particle moves to a nearest neighbouring site with *some probability*, and then orientation of the particle is updated based on its nematic interaction with its nearest neighbours. We define two kinds of models on the basis of the particle movement: (i) 'Equilibrium model' (EM) – particle moves with equal probability $1/4$ to any of the four neighbouring sites (Fig. 2.1(b)), (ii) 'Active model' (AM) – in this model the particle movement occurs in two steps. First, it chooses a direction along which it is more inclined. As shown in Fig. 2.1(c, d), it chooses the direction of movement along BD if $\pi/4 < \theta \leq 3\pi/4$ and along AC otherwise. In the second step, it moves to a randomly selected site between the two nearest neighbouring sites along the chosen direction. For example, if BD is selected as the direction of movement, then the particle moves to randomly selected site B or D in the second step. In both the models, we consider volume exclusion, *i. e.*, particle movement is allowed only if the selected site is unoccupied.

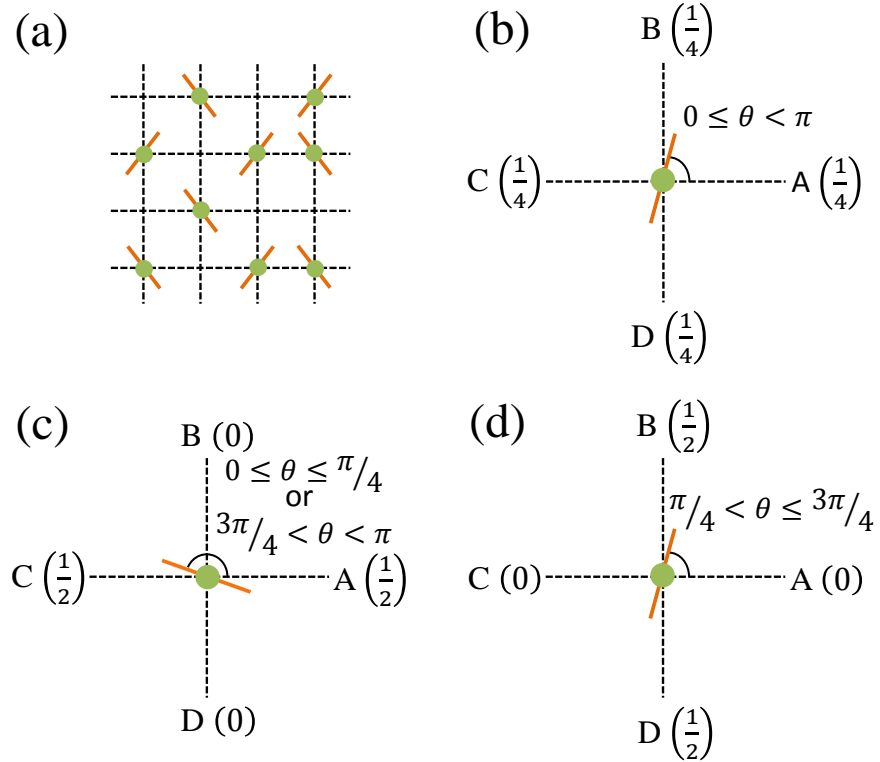


Figure 2.1: (a) Two dimensional square lattice with occupied ($n = 1$) or unoccupied ($n = 0$) sites. Filled circles indicate the occupied sites. Inclinations of the rods towards the horizontal direction show respective particle orientations $\theta \in [0, \pi]$. (b) Equilibrium move: particle can move to any of the four neighbouring sites with equal probability $1/4$. (c, d) Active move: particle can move to either of its two neighbouring sites with probability $1/2$, if unoccupied, in the direction it is more inclined to, *i. e.*, along BD in (c), and AC in (d).

In both the models, the particles also interact with their nearest neighbours. The interaction depends on the relative orientation of the particles and is represented by a modified Lebwohl-Lasher Hamiltonian [107]

$$\mathcal{H} = -\epsilon \sum_{\langle ij \rangle} n_i n_j \cos 2(\theta_i - \theta_j), \quad (2.1)$$

where ϵ is the interaction strength between two neighbouring particles. The interaction in Eq. (2.1) governs the orientation update of the particle. We employ Metropolis Monte-Carlo (MC) algorithm [22] for orientation update of the particle after the movement trial. In both the models, an order parameter defining the global alignment of the system does not remain conserved during the MC orientation update described above. In actual granular or biological systems where mutual alignment emerges because of steric repulsion, orientation of particles need not to follow a conservation law. Therefore, an order parameter defined

by coarse-graining the orientation in our present model is a class of non-conserved order parameter, *i. e.*, *Model A* [76] as described in Sec 1.6.1.

Both the models EM and AM comprise two different physical aspects – motion of the particles and nematic interaction amongst the nearest neighbours. If the particles are not allowed to move, the models reduce to an apolar analogue of the diluted XY model with nonmagnetic impurities [108], where impurities and spins are analogous to vacancies and particles, respectively. However, unlike the diluted XY model, particles in these models are dynamic. In the EM, the particle diffuses to neighbouring sites, whereas it moves anisotropically in the AM. In general, the anisotropic movement of the active particles arises because of the self-propelled nature of the particles in many biological [41] and granular systems [12, 13]. This move produces an active curvature coupling current in the coarse-grained hydrodynamic EOMs [36, 37]. The AM does not satisfy the detailed balance principle [22] because of the orientation update after the anisotropic movement. The coupling of the particle movement with the orientation update in our active model is analogous to the active Ising model introduced by Solon and Tailleur [34, 35], where the probabilistic flip of the spins is an equilibrium process, whereas the out-of-equilibrium aspect of the model is attributed to the anisotropic movement probability of the spins. However, their orientation update algorithm [34, 35] is similar to kinetic Monte-Carlo, whereas we use Metropolis Monte-Carlo algorithm to update particle orientation.

2.3 NUMERICAL STUDY

We consider a collection of N particles with random orientation $\theta \in [0, \pi]$ homogeneously distributed on a $L \times L$ lattice ($L = 256, 400, 512$) with periodic boundary. Packing density of the system is defined as $C = N/L^2$, which we consider as a dimensionless quantity. We choose a particle randomly, move it to a neighbouring site obeying exclusion, and then update its orientation using Metropolis algorithm. In each iteration we repeat the same process for N times, and we use 1.5×10^6 iterations to achieve the steady-state of the system. We obtain the steady-state results by averaging the observables over next 1.5×10^6 iterations and use more than twenty realisations for better statistics.

The ordering in the system is characterised by a scalar order parameter defined as

$$S = \sqrt{\left(\frac{1}{N} \sum_i n_i \cos(2\theta_i)\right)^2 + \left(\frac{1}{N} \sum_i n_i \sin(2\theta_i)\right)^2}. \quad (2.2)$$

It is proportional to the positive eigenvalue of the nematic order parameter Q [60], as discussed in Sec. 1.5. It takes the minimum value 0 in the disordered state and the maximum value 1 in the complete ordered state. In this chapter, we take care of the temperature T by a dimensionless quantity, called ‘inverse temperature’, $\beta\epsilon = \epsilon/k_B T$, where k_B is the Boltzmann constant. First we study the EM as a function of the inverse temperature for different packing densities, where we note that the system shows disordered isotropic to nematic state (I-N) transition with decreasing temperature. In contrast to the first order I-N transition in the equilibrium Lebwohl-Lasher model in three dimensions (3D) [20, 107], we note continuous transition for the EM defined in 2D. The observed nature of the transition supports the study by Mondal and Roy [109]. Similar to the diluted XY model [108], the critical inverse temperature $\beta_c(C)$ increases with density in the EM. This result is shown in Appendix 2.A.

2.3.1 Phase diagram – equilibrium and active model

We construct phase diagram for both the equilibrium model and the active model on the density-temperature plane. As shown in Fig. 2.2, two distinct states appear in the EM - (i) an equilibrium isotropic (EI) state on the left side of the red boundary and (ii) an equilibrium nematic (EN) state on the right side of the red boundary. In the EI state, particles remain disordered and homogeneously distributed throughout the system. Consequently, the scalar order parameter $S \simeq 0$ in this state. With increasing density or decreasing temperature, the particles get mutually ordered and form the EN state ($S > 0$). As shown in Fig. 2.3, for a fixed temperature S increases continuously with the density, and the system enters into the nematic state. Both the particle orientation and the coarse-grained density remain homogeneous in the EN state, as shown in the real space snapshot Fig. 2.4.

Similar to the EM, the active system remains in a homogeneous disordered isotropic (I) state in the high temperature and/or low packing density regime (cyan coloured regime in

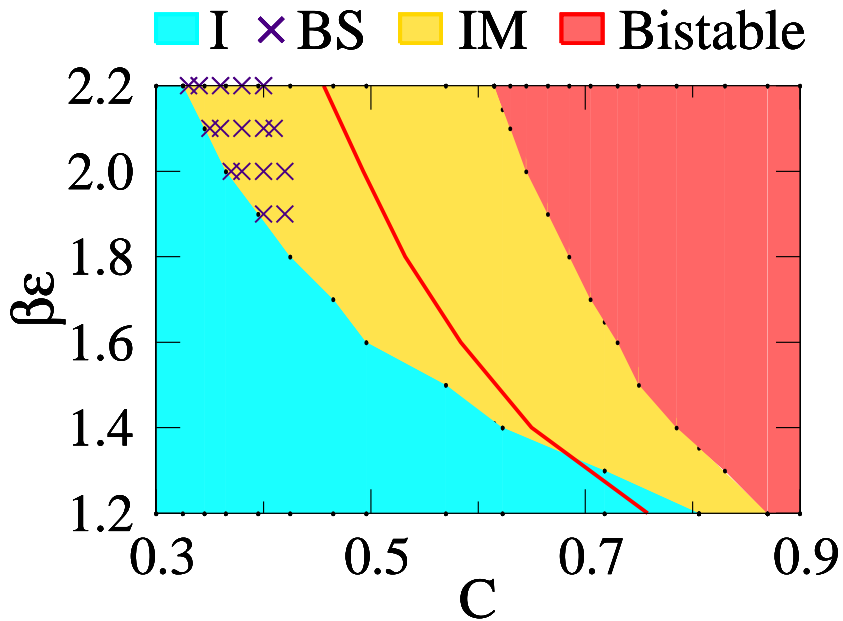


Figure 2.2: Phase diagram for both the equilibrium and the active nematic in the density versus inverse temperature plane. The equilibrium system remains in the isotropic (EI) state in the low density regime (on the left of the solid line) and in the nematic (EN) state in the high density regime (on the right of the solid line). The active nematic goes from the disordered isotropic (I) state to the locally ordered inhomogeneous mixed (IM) state with increasing density or decreasing temperature. The I - IM transition occurs with the appearance of clear bands (BS) in the low temperature regime. In the high density regime the active nematic shows bistability between the IM and the homogeneous globally ordered (HO) state.

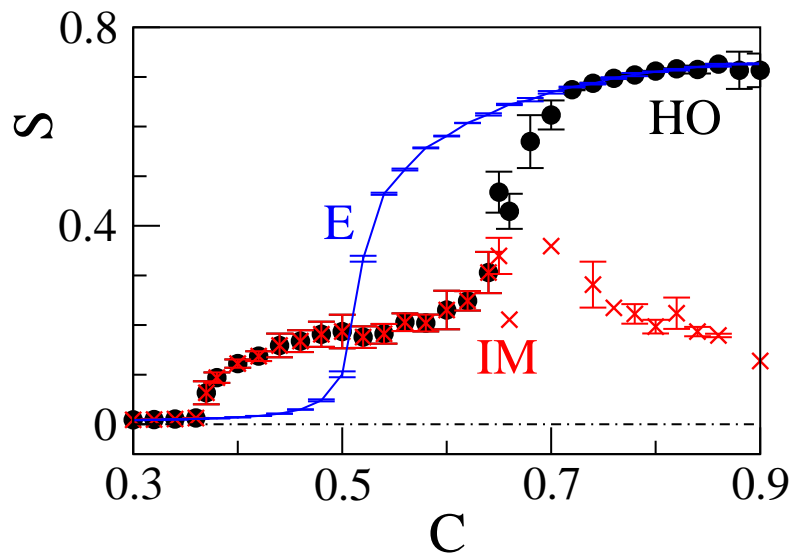


Figure 2.3: Scalar order parameter versus packing density plot for 400×400 system size at $\beta\epsilon = 2.0$. The equilibrium system (E, solid line) shows continuous isotropic to nematic state transition with increasing density. The active system goes from the isotropic (I) state to the locally ordered inhomogeneous mixed (IM, \times) state. In the high density regime the system shows bistability between the IM state and the homogeneous globally ordered (HO, \bullet) state.

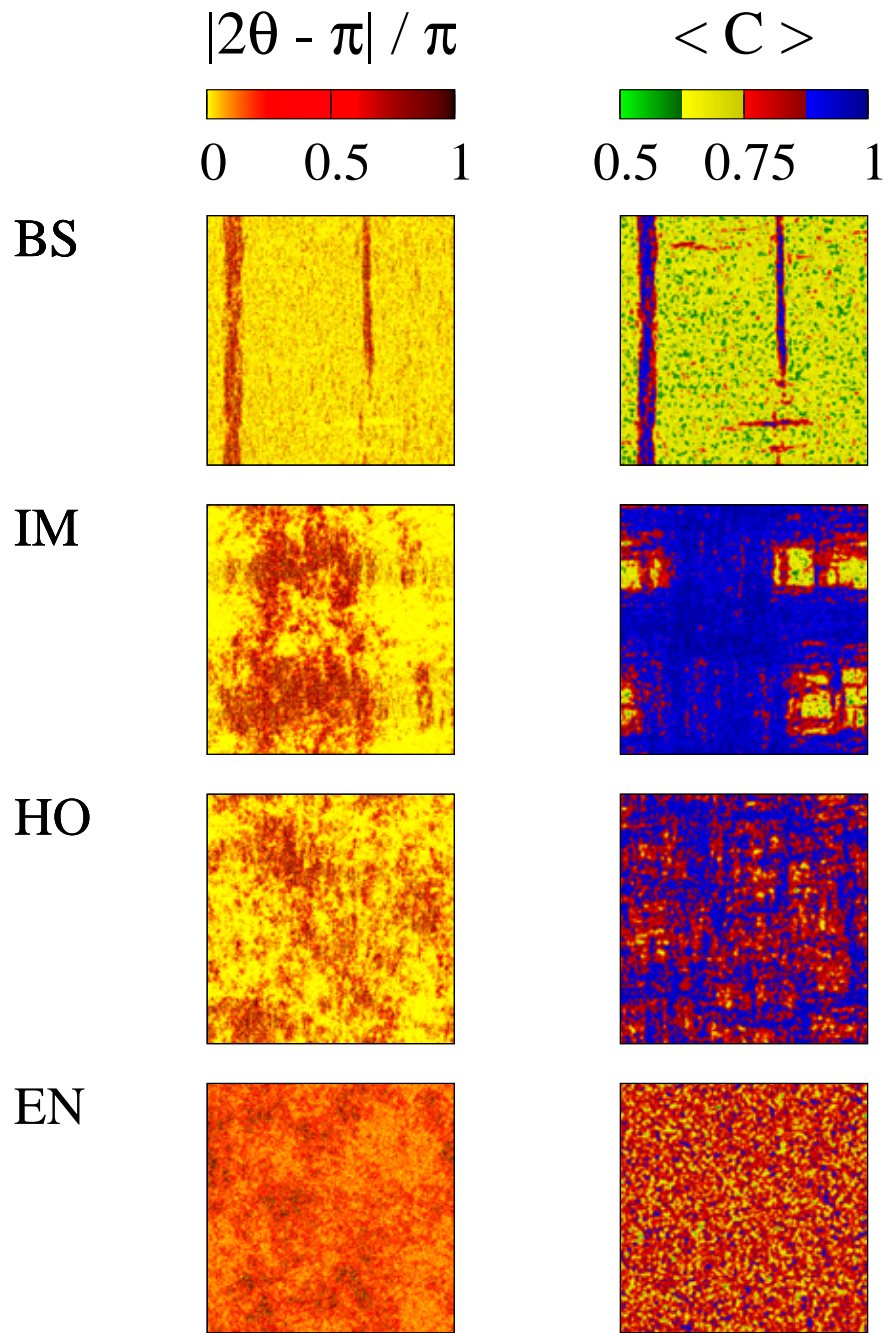


Figure 2.4: Left panel shows snapshot of the particle inclination towards the horizontal direction. Colour bar ranging from zero to one indicates vertical to horizontal orientation, respectively. BS is the banded state configuration shown for $(\beta\epsilon, C) = (2.0, 0.38)$. IM, HO and EN state configurations are shown for $(\beta\epsilon, C) = (2.0, 0.78)$. Right panel shows the coarse-grained density in the respective states.

the phase diagram Fig. 2.2). With increasing density or decreasing temperature, beyond the I state, the active system enters into an inhomogeneous mixed (IM) state (golden regime in the phase diagram Fig. 2.2), where locally ordered high-density domains coexist with disordered low-density regions. In the low temperature regime ($\beta\epsilon \in [1.9, 2.2]$), the I to IM state transition with increasing C occurs with a jump in the scalar order parameter S , as shown in Fig. 2.3. In the very beginning of the IM state, as indicated by cross symbols in Fig. 2.2, we find a banded state (BS) in the low temperature regime, where particles cluster and align themselves within a strip to form band. However, out of the strip the system remains disordered with low local density, as shown in the real space snapshot Fig. 2.4. On further increment of the packing density C , bands formed in different directions start mixing leaving the system with many locally ordered high density patches separated by low density disordered regions. Typical real space snapshots for the orientation and the coarse grained density in the IM state are shown in Fig. 2.4. The jump in the $S - C$ curve reduces with increasing temperature, and no bands appear in the high temperature ($\beta\epsilon < 1.9$) regime.

Fig. 2.3 shows that the I to BS transition occurs in the low temperature regime with a jump in S at a density lower than the corresponding equilibrium I-N transition density C_{IN} . These bands appear because of the large activity strength. A linear stability analysis, as detailed in Sec. 2.4, shows that the large activity strength induces an instability in the disordered isotropic state. This instability goes away for small activity strength or at high temperature. We also do a renormalised mean field calculation of an effective free energy written for the active nematic. The calculation predicts a jump in the scalar order parameter and shows a shift in the disordered ($S = 0$) to ordered ($S \neq 0$) state transition density. Both the jump in S and the shift in the transition density reduce with the activity strength or increasing temperature. The I to BS transition is a first order transition. The shift in the disorder-order transition point is a common feature of the active systems. For large activity and low temperature, if the system density is above a certain value but less than C_{IN} , the giant number fluctuation (GNF) present in these systems causes local alignment with local density higher than C_{IN} . As shown in Fig. 2.5, we observe the presence of GNF in the ordered active states in our model. Due to activity these locally ordered regions move anisotropically and combine with nearby region with similar local ordering. So larger ordered region forms at mean

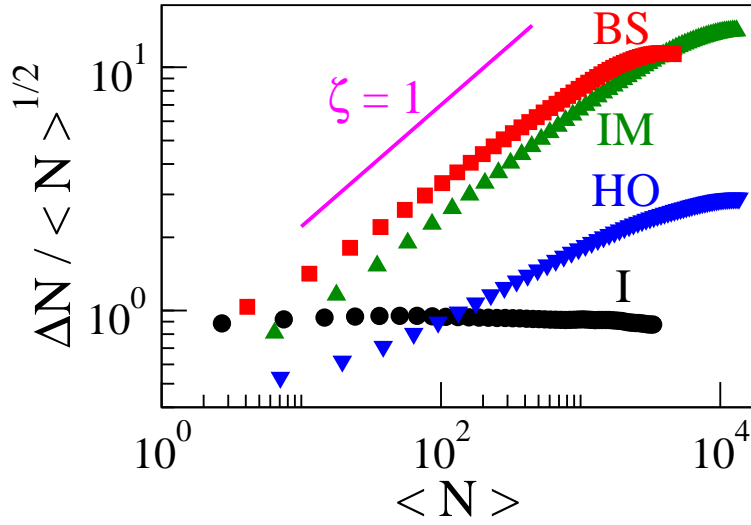


Figure 2.5: Density fluctuation $\Delta N = \sqrt{\langle N^2 \rangle - \langle N \rangle^2}$. All the active ordered states show large density fluctuation obeying the relation $\Delta N \sim \langle N \rangle^\zeta$ with $\zeta > 1/2$. The active disordered isotropic state shows normal density fluctuation with $\zeta = 1/2$.

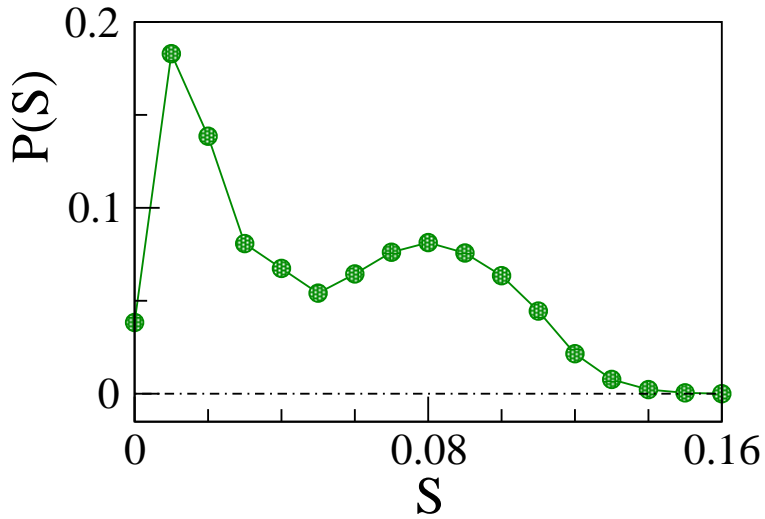


Figure 2.6: The I to IM transition at low temperature occurs with a jump in S where the particles form bands (BS). Distribution of the scalar order parameter near the I - BS transition at $(\beta\epsilon, C) = (2.0, 0.37)$ shows two peaks.

density lower than the equilibrium I-N transition density. Therefore, we find a disordered to ordered state transition at a lower density. For large activity strength, I-BS transition occurs with the jump in scalar order parameter. In our numerical study we calculate the probability $P(S)$ of the scalar order parameter averaging over many iterations and realisations near the I-BS transition point. Fig. 2.6 shows $P(S)$ has two peaks, which further supports the first order I-BS transition for large activity strength.

In the high density regime (red coloured regime in the phase diagram Fig. 2.2), the AM shows bistability, *i. e.*, it can be either in the locally ordered IM state or in a homogeneous globally ordered (HO) state. As shown in Fig. 2.3, the $S - C$ curve for fixed temperature bifurcates in the high density regime; the lower branch corresponds to the earlier discussed IM state, whereas the higher branch indicates the existence of the globally ordered state. Fig. 2.4 shows that the system possesses less density inhomogeneity in the HO state compared to the IM state. A finite size scaling of both the HO and the IM state, as shown in Fig. 2.7(a), shows that the active nematic possesses non-zero finite order in both these states. Order parameter time series shown in Fig. 2.7(b) confirms the bistability of the system in the high density regime. Bistability is not generally seen in other agent based numerical simulations of point particles [110]; it appears because of finite filling constraint of the model. This feature can be suppressed if we allow more than one particle to sit together. In the complete filling limit $C = 1.0$, the AM is equivalent to the EM, and it shows the globally ordered HO state only.

2.3.2 Two-point orientation correlation

We further characterise various states on the basis of the two-point orientation correlation in the different states of the equilibrium and the active nematic. It is defined as

$$g_2(r) = \langle \sum_i n_i n_{i+r} \cos [2(\theta_i - \theta_{i+r})] / \sum_i n_i^2 \rangle, \quad (2.3)$$

where r represents interparticle distance, and $\langle . \rangle$ signifies an average over many realisations. Fig. 2.8(a, b) show $g_2(r)$ versus r plots on log-log scale for the AM and the EM, respectively, for a fixed inverse temperature $\beta\epsilon = 2.0$. In the AM, $g_2(r)$ decays exponentially

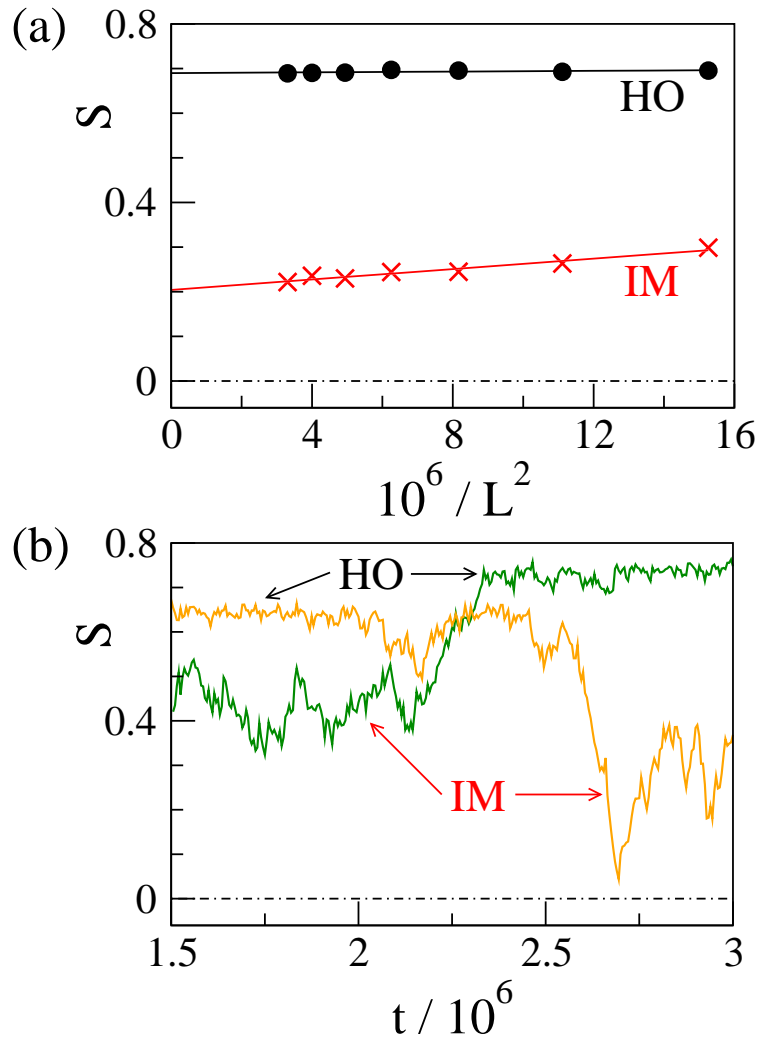


Figure 2.7: (a) Finite size scaling of S for both the HO and the IM state at $(\beta\epsilon, C) = (2.0, 0.76)$. (b) Order parameter time series show that the active system flips between the HO and the IM state in the bistable regime. Two time series are shown for two different parameter values in the high density regime.

at low packing density $C < 0.37$, *i. e.*, in the isotropic state. Therefore, the active isotropic is a short range ordered (SRO) state. In the BS at $C = 0.38$, $g_2(r)$ decays following a power law. Therefore, the system is in a quasi-long range ordered (QLRO) state. Ordering increases with density. At high packing density, correlation function confirms the bistability in the active system. At $C = 0.82$, $g_2(r)$ shows power law decay in the HO state, whereas in the IM state $g_2(r)$ decays abruptly after a distance r . The abrupt change in $g_2(r)$ at a certain distance indicates the presence of locally ordered clusters in the IM state. In contrast, the equilibrium system shows a transition from SRO (exponential decay) isotropic state at low density $C \lesssim 0.48$ to QLRO (power law decay) nematic state at high density $C \gtrsim 0.50$.

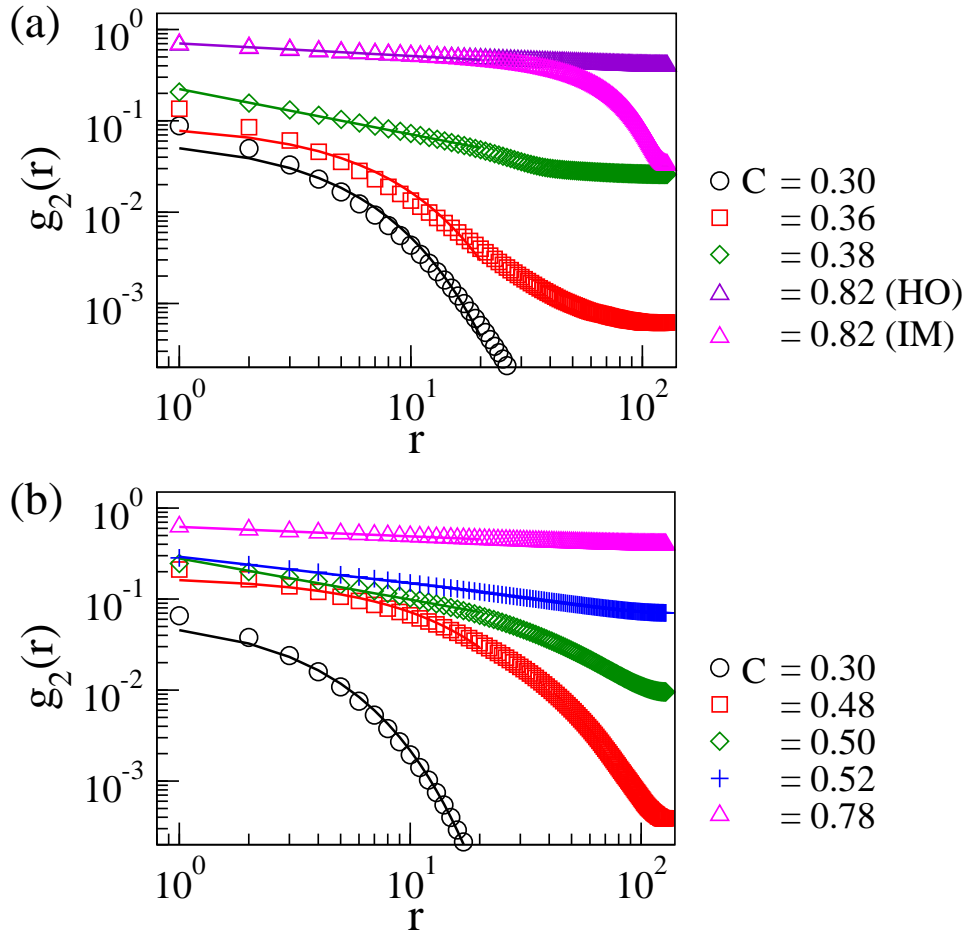


Figure 2.8: Two-point orientation correlation shown for $\beta\epsilon = 2.0$ on log-log scale. (a) Active model: $g_2(r)$ decays exponentially at low density (\circ, \square) and algebraically at high density (\diamond, \triangle). In the bistable regime at high density (\triangle), $g_2(r)$ decays algebraically in the HO state and abruptly in the IM state. (b) Equilibrium model: $g_2(r)$ decays exponentially at low density (\circ, \square) and algebraically at high density ($\diamond, +, \triangle$). Continuous lines are the respective fits, fitted for more than one decade.

2.3.3 Orientation distribution and autocorrelation of the mean orientation

We compare the steady-state properties of the active and the equilibrium models in the high density limit. First we calculate the steady-state (static) orientation distribution $P(\theta)$ from a snapshot of particle orientation θ . As shown in Fig. 2.9(a), both the active HO and the equilibrium nematic show Gaussian distribution of orientation. Peak position of $P(\theta)$ for both the EN and the HO state can appear at any point between 0 and π because of the continuous broken rotational symmetry of the Hamiltonian shown in Eq. (2.1). Data shown in Fig. 2.9(a) is for one realisation only, and for other realisations also the distribution

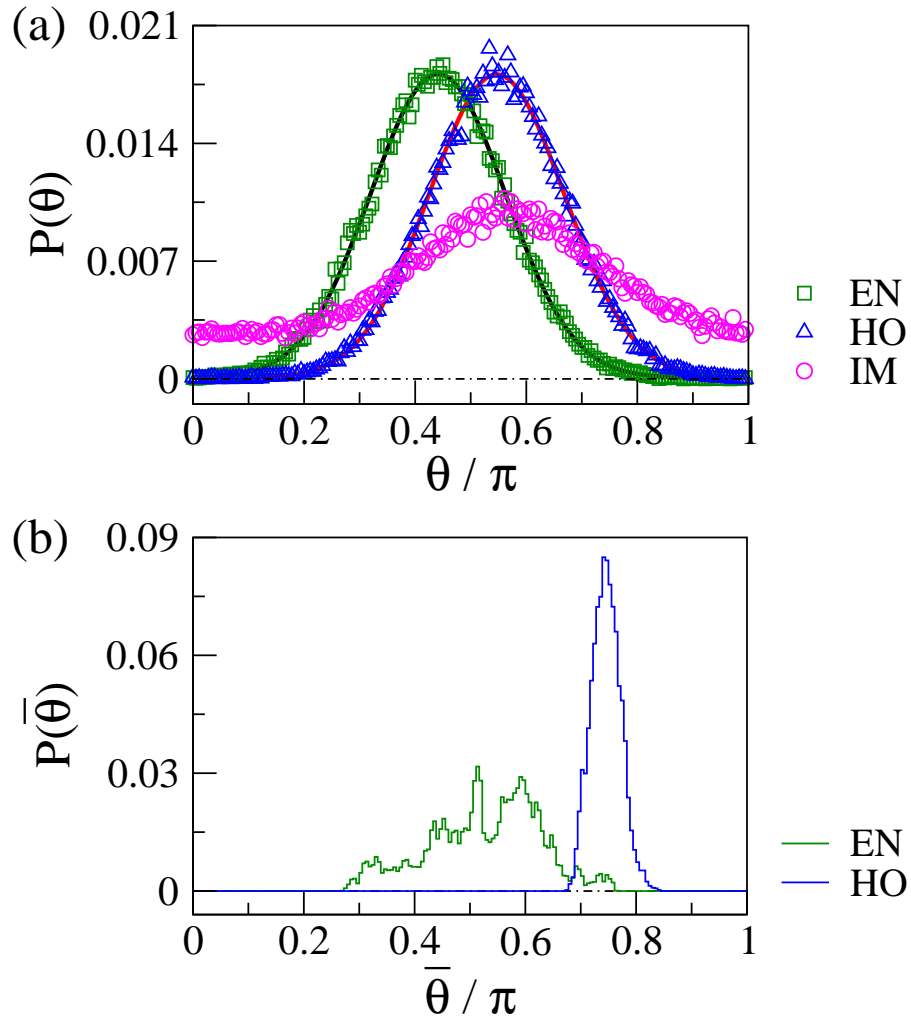


Figure 2.9: Steady-state characteristics of high density states. (a) Orientation distribution $P(\theta)$ of particles calculated from one snapshot in the steady-state. $P(\theta)$ fits with Gaussian distribution (continuous lines) for both the HO and the EN states. The IM state shows broad distribution of θ . (b) Distribution of the mean orientation $P(\bar{\theta})$ calculated from $\bar{\theta}$ of each snapshot in the steady-state. $P(\bar{\theta})$ is broad for the EN state in comparison to the HO state.

$P(\theta)$ remains Gaussian with peak at other θ values. Therefore, orientation fluctuation of the particles in the active HO state is same as in the equilibrium nematic state. The distribution $P(\theta)$ in the IM state is very broad and spans over the whole range of orientation. Therefore, the system possess no global ordering in the IM state.

We also calculate the time averaged distribution $P(\bar{\theta})$ of mean orientation of all the particles in the active HO and the equilibrium nematic states. The mean orientation $\bar{\theta}(t)$ of all particles is calculated for each iteration time t in the steady-state. The distribution $P(\bar{\theta})$ of the mean orientation is obtained from these $\bar{\theta}(t)$ data. This distribution is a measure of the fluc-

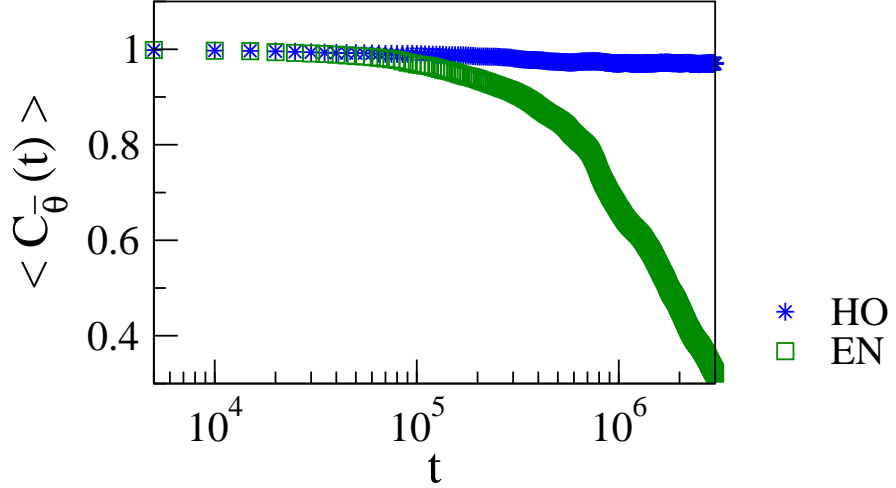


Figure 2.10: Steady-state characteristics of high density states. Steady-state autocorrelation $C_{\bar{\theta}}(t)$ of the mean orientation of the system. All plots are shown for $(\beta\epsilon, C) = (2.0, 0.80)$.

tuation in the global orientation of the particles in the steady-state. As shown in Fig. 2.9(b), $P(\bar{\theta})$ in the active HO state is narrow in comparison to the broad distribution in the EN state. We also calculate the autocorrelation of the mean orientation defined as

$$C_{\bar{\theta}}(t) = \left\langle \frac{1}{t} \sum_{\tau=1}^t \cos [2 \{ \bar{\theta}(t_0) - \bar{\theta}(t_0 + \tau) \}] \right\rangle, \quad (2.4)$$

where t_0 is an arbitrary simulation time in the steady-state. in the steady-state. As shown in Fig. 2.10, $C_{\bar{\theta}}(t)$ decreases with time in the EN state, but remains unchanged in the active HO state. Both these results imply that the fluctuation in the global orientation direction $\bar{\theta}$ in the active HO state is small compared to the EN state. We do not calculate the mean orientation $\bar{\theta}$ in the active IM state, because the system possesses no global ordering in this state.

2.4 HYDRODYNAMICS OF THE ACTIVE MODEL AT LOW DENSITY

In this section we write the hydrodynamic EOMs for the active model and characterise the low density states of the system. As discussed in Sec. 1.5.2, the relevant slow variables for the coarse-grained AM are number density $\rho(\mathbf{r}, t)$ (for definition, see Eq. (1.5)) and tensor order parameter $\mathbf{Q}(\mathbf{r}, t)$ (see Eq. (1.17) for definition). Here we represent the order parameter by a

modified variable $\Pi(\mathbf{r}, t) = \rho(\mathbf{r}, t)\mathbf{Q}(\mathbf{r}, t)$ for simplicity. The EOMs for the slow variables are as follows [36, 37]:

$$\partial_t \rho = a_0 \nabla_i \nabla_j \Pi_{ij} + D_\rho \nabla^2 \rho \quad (2.5)$$

and

$$\partial_t \Pi_{ij} = \{\alpha_1(\rho) - \alpha_2(\Pi : \Pi)\} \Pi_{ij} + \beta \left(\nabla_i \nabla_j - \frac{1}{2} \delta_{ij} \nabla^2 \right) \rho + D_\Pi \nabla^2 \Pi_{ij}. \quad (2.6)$$

The total number of particles being a conserved quantity of the system, Eq. (2.5) represents a continuity equation $\partial_t \rho = -\nabla \cdot \mathbf{J}$ where the current $J_i = -a_0 \nabla_j \Pi_{ij} - D_\rho \nabla_i \rho$. The first term of J_i consists of two parts – an anisotropic diffusion current $J_{p1} \propto Q_{ij} \nabla_i \rho$ and an active curvature coupling current $J_a \propto a_0 \rho \nabla_j Q_{ij}$ where a_0 represents activity strength of the system. The second term represents an isotropic diffusion $J_{p2} \propto \nabla \rho$. The α terms in Eq. (2.6) represent mean field alignment in the system. We choose $\alpha_1(\rho) = (\rho/\rho_{IN} - 1)$ as a function of density that changes sign at some critical density ρ_{IN} . The β term represents coupling with density. The last term represents diffusion in order parameter that is written under equal elastic constant approximation for two-dimensional nematic. The steady-state solution $\rho(\mathbf{r}, t) = \rho_0$ and $\Pi(\mathbf{r}, t) = \Pi_0$, where $\Pi_0 = \sqrt{\alpha_1(\rho_0)/\alpha_2}$, of Eqs. (2.5) and (2.6) represents a homogeneous ordered state for $\alpha_1(\rho_0) > 0$ at $\rho_0 > \rho_{IN}$, and a disordered isotropic state for $\alpha_1(\rho_0) < 0$ at $\rho_0 < \rho_{IN}$. The Eqs. (2.5) and (2.6) represent similar phenomenology as discussed in Sec. 1.5.2.

We study the linear stability of the disordered isotropic state ($\Pi_0 = 0$) by examining the dynamics of spatially inhomogeneous fluctuations $\delta\rho(\mathbf{r}, t) = \rho(\mathbf{r}, t) - \rho_0$, $\delta\Pi_{11} = \Pi_{11}(\mathbf{r}, t)$, and $\delta\Pi_{12} = \Pi_{12}(\mathbf{r}, t)$. We obtain the linearised coupled equations of motion for small fluctuations as

$$\partial_t \delta\rho = a_0 \left(\partial_x^2 - \partial_y^2 \right) \delta\Pi_{11} + 2a_0 \partial_x \partial_y \delta\Pi_{12} + D_\rho \nabla^2 \delta\rho, \quad (2.7)$$

$$\partial_t \delta\Pi_{11} = \alpha_1(\rho_0) \delta\Pi_{11} + D_\Pi \nabla^2 \delta\Pi_{11} + \frac{\beta}{2} \left(\partial_x^2 - \partial_y^2 \right) \delta\rho, \quad (2.8)$$

$$\partial_t \delta\Pi_{12} = \alpha_1(\rho_0) \delta\Pi_{12} + D_\Pi \nabla^2 \delta\Pi_{12} + \beta \partial_x \partial_y \delta\rho. \quad (2.9)$$

Using Fourier transformation defined as

$$Y(\mathbf{q}, \lambda) = \int e^{i\mathbf{q}\cdot\mathbf{r}} e^{\lambda t} Y(\mathbf{r}, t) d\mathbf{r} dt, \quad (2.10)$$

we get linear set of equations in the Fourier space as

$$\lambda \begin{pmatrix} \delta\rho \\ \delta\Pi_{11} \\ \delta\Pi_{12} \end{pmatrix} = M \begin{pmatrix} \delta\rho \\ \delta\Pi_{11} \\ \delta\Pi_{12} \end{pmatrix}, \quad (2.11)$$

where M is the coefficient matrix as obtained from Eqs. (2.7), (2.8) and (2.9) after the transformation. We solve Eq.(2.11) for the hydrodynamic modes λ . We choose $q_x = q_y = \frac{q}{\sqrt{2}}$ since both the directions are equivalent. Therefore, we obtain

$$(\lambda - \alpha_1(\rho_0) + D_{\Pi}q^2) \left\{ (\lambda + D_{\rho}q^2) (\lambda - \alpha_1(\rho_0) + D_{\Pi}q^2) - \frac{1}{2}a_0\beta q^4 \right\} = 0. \quad (2.12)$$

For small wave-vector q limit, we can find an unstable mode

$$\lambda_+ = -2D_{\rho}q^2 + \frac{a_0\beta q^4}{2|\alpha_1(\rho_0)|} - \frac{a_0\beta q^6(D_{\Pi} - D_{\rho})}{\alpha_1^2(\rho_0)}. \quad (2.13)$$

For small D_{ρ} and large activity a_0 this mode becomes unstable for $q < q_c$, where

$$q_c^2 = \frac{|\alpha_1(\rho_0)|}{2\Delta D} + \frac{1}{2} \sqrt{\left(\frac{|\alpha_1(\rho_0)|}{\Delta D} \right)^2 - \frac{8D_{\rho}\alpha_1^2}{\Delta D a_0\beta'}} \quad (2.14)$$

provided $\Delta D = D_{\Pi} - D_{\rho}$ is positive and $a_0\beta > 8D_{\rho}\Delta D$. Therefore, the unstable mode λ_+ causes the I - BS transition for small diffusivity, *i. e.*, at low temperature and for large activity strength a_0 .

We also calculate the jump in the scalar order parameter S and the shift in the transition density from Eqs. (2.5) and (2.6). A homogeneous steady-state solution of these equations gives a mean field transition from the isotropic to the nematic state at density ρ_{IN} where $\alpha_1(\rho)$ changes sign. Using renormalised mean field (RMF) method, we calculate an effective

free energy $\mathcal{F}_{eff}(S)$ close to the order-disorder transition where S is small. We consider density fluctuations $\delta\rho$ and neglect order parameter fluctuations. The effective free energy is

$$\mathcal{F}_{eff}(S) = -\frac{b_2}{2}S^2 - \frac{b_3}{3}S^3 + \frac{b_4}{4}S^4, \quad (2.15)$$

where $b_2 = \alpha_1(\rho) + \alpha'_1 c$ and c is a constant. $\alpha'_1 = \partial\alpha_1/\partial\rho|_{\rho_0}$, $b_3 = a_0\rho_0\alpha'_1/2D_\rho$ and $b_4 = \frac{1}{2}\rho_0^2\alpha_2$. Both b_3 and b_4 are positive. A detailed calculation for \mathcal{F}_{eff} is shown in the Supplementary Information. The density fluctuations introduce a new cubic order term in the free energy $\mathcal{F}_{eff}(S)$ that is proportional to the activity strength a_0 . The presence of such term produces a jump $\Delta S = S_c = 2b_3/3b_4$ at a density $\rho_c = \rho_{IN}(1 - 2b_3^2/9b_4) < \rho_{IN}$. Fluctuation in density produces a jump in order parameter and shifts the critical density. Such type of fluctuation induced transitions are called fluctuation dominated first order phase transitions in statistical mechanics [111] and are widely studied for many systems [112, 113]. The jump in S and the shift in the transition density are proportional to the activity strength a_0 , and for $a_0 = 0$ we recover the equilibrium transition.

2.5 DISCUSSION

In this chapter, we have introduced a minimal lattice model for the active nematic and studied different ordering states in the density-temperature plane. A brief summary of the results is as follows. In the low density regime, the system is in the disordered isotropic (I) state with short range orientation correlation amongst the particles. In the low temperature regime, large density fluctuation in the active system induces a first order transition from the isotropic to the banded state with a jump in the scalar order parameter at a density lower than the equilibrium isotropic-nematic (I-N) transition density. The linear stability analysis of the isotropic state shows an instability for large activity strength in the low temperature regime. Such instability governs the band formation at density below the equilibrium I-N transition density. As we further increase density, bands vanish and locally ordered patches appear in the inhomogeneous mixed (IM) state. Renormalised mean field calculation confirms the jump in the scalar order parameter and the shift in the transition density. With

increasing temperature the shift in the transition density and the jump in scalar order parameter decreases, and no bands appear in the system. The IM state is a state with coexisting aligned and disordered domains, similar to the coexisting or defect-ordered states found in Ref. [30, 68–71, 110, 114, 115].

In the high density regime, the active nematic shows switching between the IM (low S) and the homogeneous ordered (HO, high S) states, *i. e.*, the system shows bistability. In the complete filling limit and with excluded volume assumption the active model reduces to the equilibrium model. Therefore, the active model tends to show a homogeneous nematic state in the high density regime. However, large activity strength makes the HO state unstable and leads the system to the IM state. This instability in the HO state is similar to the earlier studies in Ref. [30, 114]. Ngo *et al.* [110] considered a two dimensional off-lattice model for the active nematic without the exclusion constraint. In the low and moderate density regime, they show a homogeneous disordered phase and an inhomogeneous chaotic phase, which are similar to the isotropic and the IM states, respectively. Similar to their study, the spanning area of the IM state (golden regime in the phase diagram Fig. 2.2) along the density axis decreases with the increasing temperature. In the high density limit, they note a homogeneous quasi-ordered phase only, which is similar to the HO state in our study. However, we show the bistability between the HO and the IM state in this density limit.

In conclusion, our lattice model for the active nematic is a simple one to design and execute numerically, and easy to compare with the corresponding equilibrium model. It shows new features like the BS in the low temperature regime and the bistability in the high density regime, as well as some of the earlier characterised states, *e. g.*, the IM state. It also shows many basic features of the active nematic like large number fluctuation, long-time decay of orientation correlation, transition from SRO isotropic to QLRO nematic state. The shift in the transition density due to activity strength compared to the equilibrium model can be tested in experiments where activity can be tuned. We expect the emergence of the bistability in the high density regime in a two dimensional experimental system composed of apolar particles with finite dimension and high activity strength. It would be interesting to study the model without volume exclusion. In this study, particle orientation has continuous symmetry of $O(2)$. Therefore, the equilibrium limit of our model is an apolar analogue

of the two-dimensional XY model. One can also study the model with discrete orientation symmetry as in Ref. [34, 35, 104] and compare the results with the corresponding equilibrium model.

APPENDIX

2.A ORDER-DISORDER TRANSITION IN THE EQUILIBRIUM MODEL

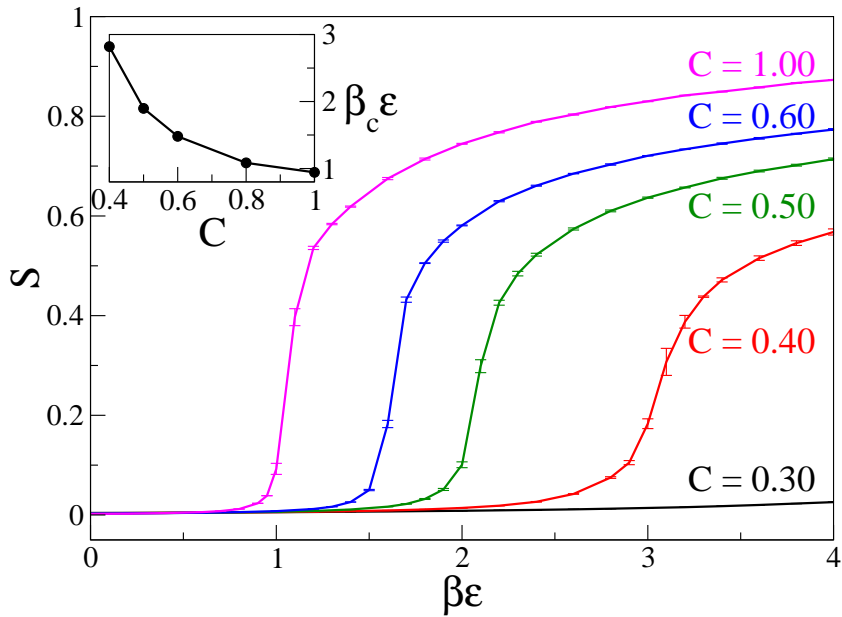


Figure 2.A.1: Order-disorder transition in the equilibrium model. Main – scalar order parameter S versus inverse temperature $\beta\epsilon$ plot for different density C . With increasing $\beta\epsilon$ the system goes from the isotropic (small S) to the nematic (large S) state. The critical temperature for $C = 1$ matches with the corresponding value for the equilibrium XY model [108]. Inset – the critical inverse temperature decreases with increasing density. Similar phenomenon was earlier observed for diluted XY model [108].

2.B RENORMALISED MEAN FIELD (RMF) STUDY OF ACTIVE NEMATIC FOR SMALL SCALAR ORDER PARAMETER

In this appendix section, we write an effective renormalised mean field free energy for the scalar order parameter S under the small S approximation. We consider the fluctuations in the density and ignore the order parameter fluctuations in the coupled hydrodynamic

equations of motion for the active nematic. Density fluctuation introduces a cubic order term in S in the effective free energy. Such term produces a jump in S at a new transition density ρ_c lower than the equilibrium I-N transition point ρ_{IN} . Shift in the transition density and the jump ΔS are directly proportional to the activity strength a_0 . We recover the equilibrium limit for zero a_0 .

If we Consider a small perturbation over the homogeneous steady-state solution of Eqs. (2.5) and (2.6), we obtain from the density equation,

$$\begin{aligned} a_0 \nabla_i \nabla_j \Pi_{ij} + D_\rho \nabla^2 \delta\rho &= 0 \\ \Rightarrow a_0 \nabla_j \Pi_{ij} + D_\rho \nabla_i \delta\rho &= \mathbf{c} \equiv \text{constant}, \end{aligned} \quad (2.16)$$

where $\Pi_{11} = -\Pi_{22} = \frac{\xi}{2} \cos(2\theta)$, $\Pi_{12} = \Pi_{21} = \frac{\xi}{2} \sin(2\theta)$ and θ represents coarse-grained direction of the broken symmetry (see Sec. 1.5.2). Considering only the lowest order terms in S and θ , we obtain

$$\partial_x \delta\rho = -\frac{a_0 \rho_0}{2D_\rho} \partial_x S \Rightarrow \delta\rho(x) = -\frac{a_0 \rho_0}{2D_\rho} S + c_1 \quad (2.17)$$

and

$$\partial_y \delta\rho = \frac{a_0 \rho_0}{2D_\rho} \partial_y S \Rightarrow \delta\rho(y) = \frac{a_0 \rho_0}{2D_\rho} S + c_2. \quad (2.18)$$

Here we assume the system is aligned along one direction, and the variation in orientation is only along the perpendicular direction. Therefore, we can choose either of Eqs. (2.17) or (2.18). Two constants c_1 and c_2 are the fluctuations in density when the nematic order parameter is zero.

Now from the order parameter Eq. (2.6), we obtain an effective equation for S as

$$\partial_t S = \left\{ \alpha_1(\rho) - \frac{\rho^2}{2} \alpha_2 S^2 \right\} S + \mathcal{O}(\nabla^2 S) + \mathcal{O}(\nabla^2 \rho). \quad (2.19)$$

We neglect all the derivative terms and retain only the polynomials in S , *i. e.*, we neglect higher order fluctuations. The Taylor expansion of $\alpha_1(\rho)$ about the mean density ρ_0 gives $\alpha_1(\rho) = \alpha_1(\rho_0 + \delta\rho) = \alpha_1(\rho_0) + \alpha'_1\delta\rho$ where $\alpha'_1 = \frac{\partial\alpha_1}{\partial\rho}|_{\rho_0}$. This gives

$$\partial_t S = \left\{ \alpha_1(\rho_0) + \alpha'_1\delta\rho - \frac{\rho_0^2}{2}\alpha_2 S^2 \right\} S. \quad (2.20)$$

We can write an effective free energy $\mathcal{F}_{eff}(S)$ so that

$$\partial_t S = -\frac{\delta\mathcal{F}_{eff}(S)}{\delta S}. \quad (2.21)$$

Substituting the expression for $\delta\rho$ from Eq. (2.18), we obtain

$$-\frac{\delta\mathcal{F}_{eff}}{\delta S} = S \left\{ \alpha_1(\rho_0) + \alpha'_1 \left(\frac{a_0\rho_0}{2D\rho} S + c_2 \right) - \frac{\rho_0^2}{2}\alpha_2 S^2 \right\}. \quad (2.22)$$

Therefore,

$$\mathcal{F}_{eff}(S) = -\frac{b_2}{2}S^2 - \frac{b_3}{3}S^3 + \frac{b_4}{4}S^4, \quad (2.23)$$

where $b_2 = \alpha_1(\rho_0) + \alpha'_1 c_2$, $b_3 = \frac{a_0\rho_0\alpha'_1}{2D\rho}$ and $b_4 = \frac{1}{2}\rho_0^2\alpha_2$. Since the free energy is a state function, we have assumed the integration constant to be zero. Therefore, the fluctuation in the density introduces a cubic order term in the effective free energy $\mathcal{F}_{eff}(S)$. Effective free energy in Eq. (2.23) is similar to the Landau free energy with a new cubic order term [20]. Now we calculate the jump ΔS and the new critical density from the coexistence condition for free energy. Steady-state solutions of order parameter ($S = 0$ for isotropic and $S \neq 0$ for ordered state) are given by

$$\frac{\delta\mathcal{F}_{eff}}{\delta S} = (-b_2 - b_3 S + b_4 S^2) S = 0. \quad (2.24)$$

Non-zero S is given by $-b_2 - b_3 S_c + b_4 S_c^2 = 0$. Coexistence condition implies

$$\mathcal{F}_{eff}(S_c) = \left(-\frac{b_2}{2} - \frac{b_3}{3}S_c + \frac{b_4}{4}S_c^2 \right) S_c^2 = \mathcal{F}_{eff}(S = 0) = 0. \quad (2.25)$$

Hence we get the solution

$$S_c = -\frac{3b_2}{b_3} \quad (2.26)$$

and

$$b_2^c = -\frac{2b_3^2}{9b_4}. \quad (2.27)$$

Therefore, the jump at the new critical point is $\Delta S = \frac{2b_3}{3b_4}$. Since $b_4 > 0$ and hence $b_2^c < 0$, the new critical density

$$\rho_c = \rho_{IN} \left(1 - \frac{2b_3^2}{9b_4} \right) < \rho_{IN} \quad (2.28)$$

is shifted to a lower density in comparison to the equilibrium transition density ρ_{IN} . Eq. (2.28) gives the expression for new transition density as given in the main text. Therefore, using renormalised mean field theory we find a jump ΔS at a lower density as compared to the equilibrium I-N transition density.

ORDERING DYNAMICS OF SELF-PROPELLED PARTICLES IN AN INHOMOGENEOUS MEDIUM

3.1 INTRODUCTION

The study of coarsening in self-propelled particles (SPPs) is complicated by the fact that the system settles into a non-equilibrium steady-state (NESS). There have very few studies [2, 39, 46, 81–84] of the coarsening kinetics from a homogeneous disordered state to this asymptotic NESS, as we have discussed in Sec. 1.6.2. The ordering dynamics of an assembly of SPPs, both in *clean* and *inhomogeneous* environments, is important to understand growth processes in many natural and granular systems. In this chapter¹, we address this problem for the *polar* SPPs.

The SPPs are defined by their position and orientation (direction of velocity). Each particle moves along its orientation with a constant speed v_s and tries to align with its neighbours. In addition to this, we introduce an inhomogeneous random field \mathbf{h} of fixed strength Δ and random orientation, but quenched in time. This random field locally aligns the orientation field along a preferred (but random) direction. Such a field may arise from physical inhomogeneities in the substrate, *e. g.*, pinning sites, impurities, obstacles, channels. The random field we introduce here is analogous to the random field in equilibrium spin systems discussed in Sec. 1.7.1. We write the coarse-grained equations of motion (EOMs) for hydrodynamic variables – density and polarisation. We numerically solve these coupled nonlinear equations for different strengths of disorder. Starting from a random isotropic state, we ob-

¹ The work reported here is based on the paper “Ordering dynamics of self-propelled particles in an inhomogeneous medium”, Rakesh Das, Shradha Mishra and Sanjay Puri, *Europhysics Letters* **121**, 37002 (2018).

serve coarsening of the density and the polarisation fields. Our primary focus in this chapter is the scaling behaviour and growth laws which characterise the emergence of the asymptotic NESS from the disordered state.

Before proceeding, we should stress that there does not as yet exist a clear understanding of the nature of the NESS in the case with substrate inhomogeneity. This problem definitely requires further study. Nevertheless, it is both useful and relevant to study the coarsening kinetics even without a clear knowledge of the asymptotic state [73]. As a matter of fact, a proper understanding of coarsening kinetics in the inhomogeneous system might also provide valuable information about the corresponding NESS.

This chapter is organised as follows. In Sec. 3.2 we define the model used in this study. Details of the numerical techniques used and choices of the system parameters are given in Sec. 3.3. In Sec. 3.3.1 we shall see that, in the clean SPPs, the polarisation field grows algebraically with exponent 0.5, while the density grows with an exponent close to 0.8. The presence of inhomogeneities slows down the growth rate of the hydrodynamic fields in a complicated manner, as discussed in Sec. 3.3.2. For intermediate times, domains of the polarisation field follow a power-law growth with a disorder-dependent exponent. At late times the polarisation field shows a crossover to logarithmic growth, and the logarithmic growth exponent does not depend on the disorder. For large disorder strength the local polarisation remains pinned in the direction of the quenched random field. However, for the density field, we could not find corresponding unambiguous growth laws. We end this chapter with brief summary and concluding remarks in Sec. 3.4.

3.2 MODEL

We consider a collection of polar SPPs of length l , moving on a two-dimensional (2D) substrate of friction coefficient γ . Each particle is driven by an internal force F acting along the long axis of the particle. The ratio of the force F to the friction coefficient gives a constant self-propulsion speed $v_s = F/\gamma$ to each particle. On time-scales large compared to the interaction time, and length scales much larger than the particle size, the dynamics of the system is governed by two hydrodynamic fields – density (which is conserved), and polarisation

vector (which is a broken-symmetry variable in the ordered state). The ordered state is also a moving state with mean velocity $v_s \mathbf{p}$. The dynamics of the system is characterised by the coupled EOMs for the density and the polarisation vector. The coarse-grained density equation is

$$\frac{\partial \rho}{\partial t} = -v_s \nabla \cdot (\mathbf{p} \rho) + D_\rho \nabla^2 \rho. \quad (3.1)$$

The corresponding polarisation equation is

$$\frac{\partial \mathbf{p}}{\partial t} = [\alpha_1(\rho) - \alpha_2 p^2] \mathbf{p} - \frac{v_s}{2\rho} \nabla \rho + \lambda_1 (\mathbf{p} \cdot \nabla) \mathbf{p} + \lambda_2 \nabla(p^2) + \lambda_3 \mathbf{p} (\nabla \cdot \mathbf{p}) + K \nabla^2 \mathbf{p} + \mathbf{h}. \quad (3.2)$$

The hydrodynamic Eqs. (3.1) and (3.2) are similar in spirit of the Eqs. (1.7) and (1.11). Next we discuss the details of different terms in the above two equations.

In Eq. (3.1), D_ρ represents diffusivity in the density field. Since the number of particles is conserved, we can express the right-hand-side (RHS) of Eq. (3.1) as $-\nabla \cdot \mathbf{J}$, where the current \mathbf{J} consists of terms $J_d \propto \nabla \rho$ and an active current $J_a \propto v_s \mathbf{p} \rho$. The active current arises because of the self-propelled nature of the particles.

The α -terms on the RHS of Eq. (3.2) represent mean-field alignment in the system. We choose $\alpha_1(\rho) = \frac{\rho}{\rho_c} - 1$ and $\alpha_2 = 1$ (for discussion, see Sec. 1.4.3). Then the clean system ($\mathbf{h} = \mathbf{0}$) shows a mean field transition from an isotropic disordered state with $\mathbf{p} = 0$ for mean density $\rho_0 < \rho_c$ to a homogeneous ordered state with $\mathbf{p} = \sqrt{\frac{\alpha_1(\rho_0)}{\alpha_2}}$ for $\rho_0 > \rho_c$. The $\nabla \rho$ term in Eq. (3.2) represents pressure in the system appearing because of density fluctuations. Here, \mathbf{p} plays a dual role in the SPP system. First, it acts like a polarisation vector order parameter of same symmetry as a 2D XY model. Second, $v_s \mathbf{p}$ is the flock velocity with which the density field is convected. Therefore, we choose the same v_s for the active current term in the density equation and the pressure term in the polarisation equation, because origin of both is the presence of non-zero self-propelled speed. As soon as we turn off v_s , the active current turns zero, and the density shows usual diffusive behaviour. Then we can ignore density fluctuations as well as the pressure term. However, in general they can be treated as two independent parameters as discussed in Sec. 1.4.3. λ terms are the convective

nonlinearities, present because of the absence of the Galilean invariance in the system. K represents diffusivity in the polarisation equation.

To introduce inhomogeneity, *i. e.*, disorder in the system, we add a random-field term $\mathcal{F}_h = -\mathbf{h} \cdot \mathbf{p}$ into the ‘free energy’. This contributes the term $-\frac{\delta \mathcal{F}_h}{\delta \mathbf{p}} = \mathbf{h}$ in the polarisation equation. We should stress that such a term coupling to the polarisation field would not arise in the free energy of an equilibrium fluid, but may be realised in the context of the XY model where the polarisation vector is a spin variable. The random field is modeled as $\mathbf{h}(\mathbf{r}) = \Delta (\cos \psi(\mathbf{r}), \sin \psi(\mathbf{r}))$ where Δ represents the disorder strength, and $\psi(\mathbf{r})$ is a uniform random angle $\in [0, 2\pi]$. We call the model defined by the hydrodynamic Eqs. (3.1) and (3.2) as a ‘random-field active model’ (RFAM). This terminology originates from the well-known random-field Ising model (RFIM) discussed in Sec. 1.7.1, which has received great attention in the literature on disordered systems [85, 100]. We are presently studying the phase diagram of the RFAM. However, a clear determination of this is complicated by the presence of long-lived metastable states. Apart from the RFAM, it is also natural to consider a random-bond active model (RBAM), where the average orientation in the microscopic Vicsek model is weighted with ‘random-bonds’ for different neighbours. In this chapter, we will focus on the RFAM.

For zero self-propelled speed, *i. e.*, $v_s = 0$, Eq. (3.1) decouples from the polarisation field and contains only the diffusion current. Hereafter, we refer to this as a ‘zero-SPP model’ (zero-SPPM). In the zero-SPPM, although it contains convective non-linearities, but coupling to density is only diffusive type. For $\Delta = 0$, Eqs. (3.1) and (3.2) reduce to the continuum equations introduced by Toner and Tu [29], which represent the clean system. While writing Eqs. (3.1)-(3.2), all lengths are rescaled by the interaction radius in the underlying microscopic model, and time by the microscopic interaction time. In doing that all the coefficients (speed v_s , diffusivities D_ρ , K , non-linear coupling λ 's and field \mathbf{h}) are in dimensionless units. Thus, Eqs. (3.1)-(3.2) are in dimensionless units.

We should stress that the most general forms of Eqs. (3.1)-(3.2) also contain noise or “thermal fluctuations”, as have been considered in Eqs. (1.7)-(1.11). For domain growth in non-active systems [72, 73], coarsening kinetics is dominated by a zero-noise (or zero-temperature) fixed point. This is because noise only affects the interfaces between domains,

which become irrelevant compared to the divergent domain size [77]. In the present problem, we again have divergent (though different) domain scales for the density and polarisation fields, as we will see shortly. Therefore, it is reasonable to first study the zero-noise versions in Eqs. (3.1)-(3.2), as we do in the present chapter. However, it is also important to undertake a study of the noisy model and confirm the irrelevance of noise.

3.3 NUMERICAL STUDY

We numerically solve Eqs. (3.1) and (3.2) for the hydrodynamic variables. The substrate size is $L \times L$ ($L = 256, 512, 1024, 2048$) with periodic boundary conditions in both directions. An isotropic version of Euler's discretization scheme is used to approximate the partial derivatives appearing in the hydrodynamic EOMs. In our numerical implementation, the first and second order derivatives for an arbitrary function $f(\mathbf{r}, t)$ are discretized as

$$\begin{aligned}\frac{\partial f}{\partial t} &= \frac{f(t + \Delta t) - f(t)}{\Delta t}, \\ \frac{\partial f}{\partial x} &= \frac{f(x + \Delta x) - f(x - \Delta x)}{2\Delta x}, \\ \frac{\partial^2 f}{\partial x^2} &= \frac{f(x + \Delta x) - 2f(x) + f(x - \Delta x)}{(\Delta x)^2},\end{aligned}\tag{3.3}$$

where Δt and Δx are mesh sizes. While solving the equations, the field is specified on each grid point. Thus, we have a field of strength Δ and random orientation (which is quenched in time) at each grid point. The random angle is chosen from a uniform distribution in the range $[0, 2\pi]$. Our numerical scheme is convergent and stable for the chosen grid sizes $\Delta x = 1.0$ and $\Delta t = 0.1$.

We treat the parameters as phenomenological, and choose $-\lambda_1 = \lambda_2 = \lambda_3 = 0.5$, $D_\rho = 1$, $K = 1$ and $v_s = 0.5$. The above values of λ 's are chosen for simplicity. We checked that the homogeneous ordered steady-state in the clean system is stable [39] for the above choice of the parameters, and that can become unstable for large λ 's. We start with a homogeneous isotropic disordered state with mean density $\rho_0 = 0.75$ and random polarisation, and observe ordering dynamics for different strengths of the random-field $\Delta \in [0, 1]$. We assume the mean field critical density $\rho_c = 0.5$ for the clean system.

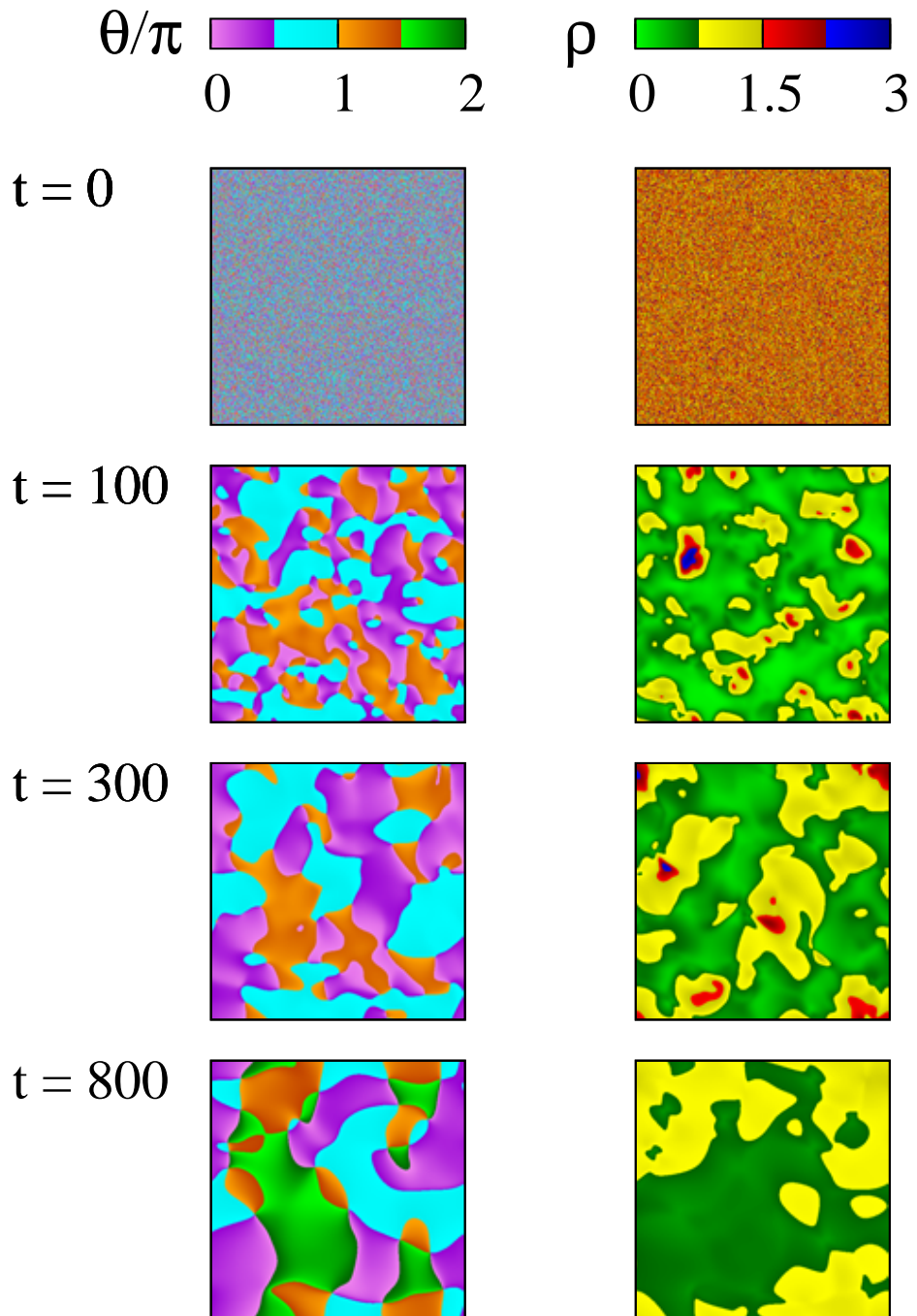


Figure 3.1: Heat map of (left panel) the orientation $\theta(r, t) = \tan^{-1} \left(\frac{p_y(r, t)}{p_x(r, t)} \right)$, and (right panel) the density, shown for the clean system ($\Delta = 0$). Starting with random orientation and uniform density at $t = 0$, the system coarsens with time. Respective times are indicated on the left margin.

3.3.1 Coarsening in clean system

We first study coarsening in the clean system, *i. e.*, for $\Delta = 0$. In Fig. 3.1, we show snapshots of the orientation (left panel) $\theta(\mathbf{r}, t) = \tan^{-1} \left(\frac{p_y(\mathbf{r}, t)}{p_x(\mathbf{r}, t)} \right)$, and the density (right panel) fields at different times. Starting from an initial isotropic state, high density domains with ordered orientation emerge in the system, and the size of these domains increases with time. In the studies of domain growth in far-from equilibrium systems [72, 73], the standard tool to characterise the evolution of morphologies is the equal-time correlation function $C(r, t)$ of the order-parameter field. We use the same tool for the two fields $\mathbf{p}(\mathbf{r}, t)$ and $\rho(\mathbf{r}, t)$, which are relevant in the present context. We introduce the two-point correlation functions:

$$C_p(r, t) = \langle \mathbf{p}(\mathbf{r}_0, t) \cdot \mathbf{p}(\mathbf{r}_0 + \mathbf{r}, t) \rangle_{\mathbf{r}_0}, \quad (3.4)$$

and

$$C_\rho(r, t) = \langle \delta\rho(\mathbf{r}_0, t) \delta\rho(\mathbf{r}_0 + \mathbf{r}, t) \rangle_{\mathbf{r}_0}. \quad (3.5)$$

Here $\delta\rho$ represents fluctuation in the density from its instantaneous local mean value. Angular brackets denote spherical averaging (assuming isotropy), plus an average over space (\mathbf{r}_0) and over 10 independent runs.

In Figs. 3.2(a) and 3.3(a), we show the correlation functions C_p and C_ρ , respectively, at different times for $\Delta = 0$. The data shows coarsening for both the fields, since the correlations increase with time. Characteristic lengths $L_p(t, \Delta)$ and $L_\rho(t, \Delta)$ are defined as the distance over which the corresponding correlation functions fall to 0.5. In Figs. 3.2(b) and 3.3(b), we plot the correlation functions C_p and C_ρ , respectively, as a function of scaled distance r/L_p and r/L_ρ . We find nice scaling collapse for the polarisation, however, not for the density. Similar results are found for other disorder strengths. The absence of dynamical scaling for the density correlation is consistent with the absence of the single energy scale associated with the density growth dynamics [72].

In Fig. 3.4(a), we show the time dependence of these length scales $L_\zeta(t, 0)$ where $\zeta \equiv (\mathbf{p}, \rho)$. We calculate the growth of the polarisation field for two cases – (i) RFAM with self-propelled

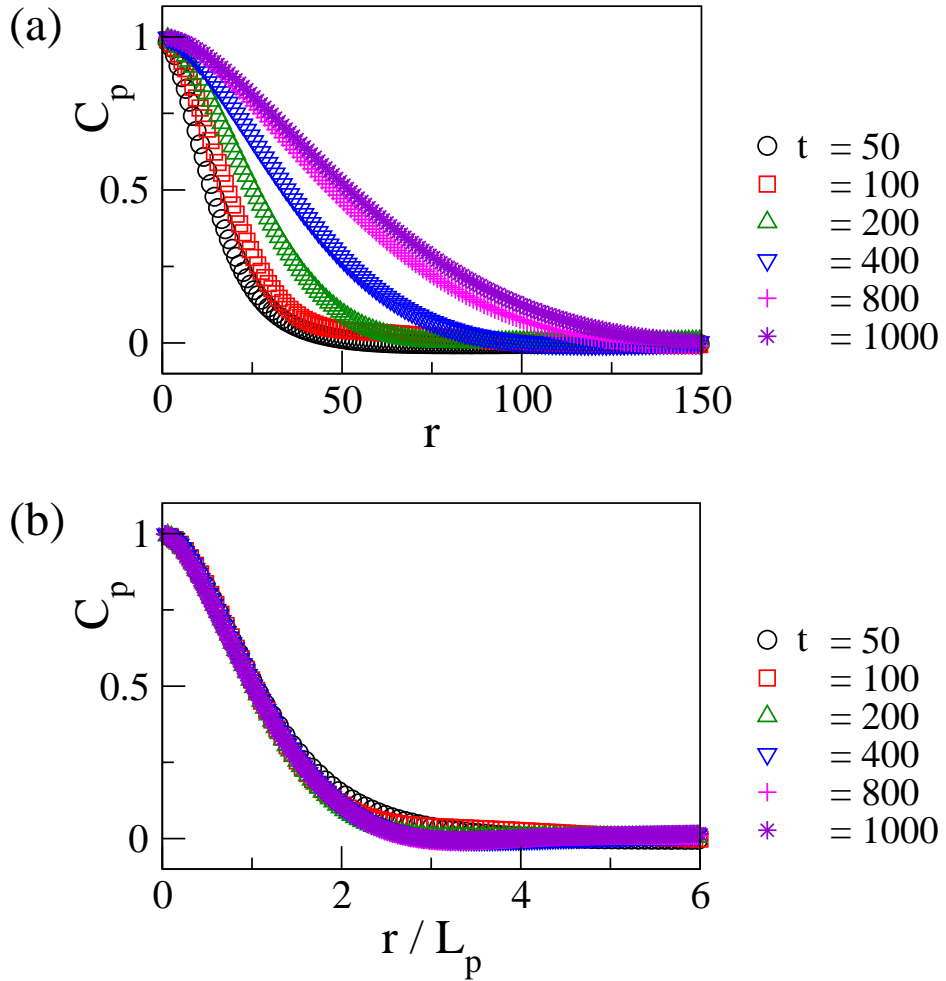


Figure 3.2: (a) Two-point correlation function versus distance plot for the polarisation field in the clean system ($\Delta = 0$) at different times. (b) Two-point correlation function versus scaled distance plot. C_p shows good collapse.

speed $v_s = 0.5$ and (ii) zero-SPPM with $v_s = 0.0$. For the clean system, we find that the characteristic length follows the similar growth law $L_p(t, 0) \sim t^{0.5}$ for both the RFAM and the zero-SPPM. The density shows usual diffusive growth for the zero-SPPM. Although the data does not show clean power-law for the density, Fig. 3.4(a) shows the growth of the characteristic length as $L_\rho(t, 0) \sim t^{0.8}$ for the RFAM in the clean system. Faster growth of the density field in our study is consistent with the previous study of self-propelled particles [46]. We define the algebraic growth law of the hydrodynamic fields in the clean system as $L_\zeta(t, 0) \sim t^{1/z_{\text{eff}}(\zeta)}$, where $z_{\text{eff}}(\zeta)$ is the effective growth exponent. In Fig. 3.4(b), we show the variation of the effective growth exponent $z_{\text{eff}}(\zeta)$ with time on log-linear scale for the two fields in the RFAM. We find $z_{\text{eff}}(p) \sim 2$ for almost two-decades, and $z_{\text{eff}}(\rho) \sim 1.2$,

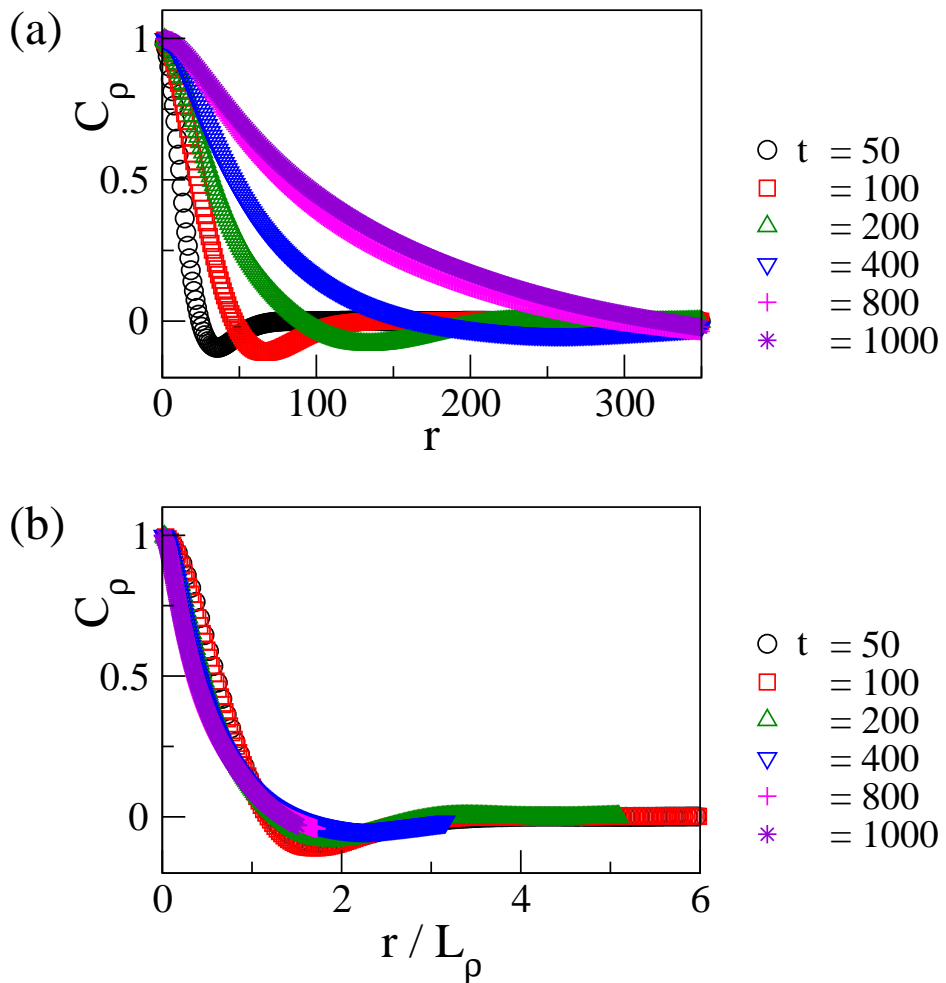


Figure 3.3: (a) Two-point correlation function versus distance plot for the density field in the clean system ($\Delta = 0$) at different times. (b) Two-point correlation function versus scaled distance plot. C_ρ does not show good scaling; therefore, dynamic scaling is absent for the density field.

when averaged over intermediate and late times, although it shows large oscillations. These oscillations are not due to poor averaging, but rather an intrinsic feature of the density growth in the active systems. These may arise due to the absence of a single energy scale for the density growth.

3.3.2 Coarsening in inhomogeneous system

Now we study the effect of disorder in the RFAM. In the studies of domain growth, it has been found that random-field and random-bond disorder slows down the coarsening [91,

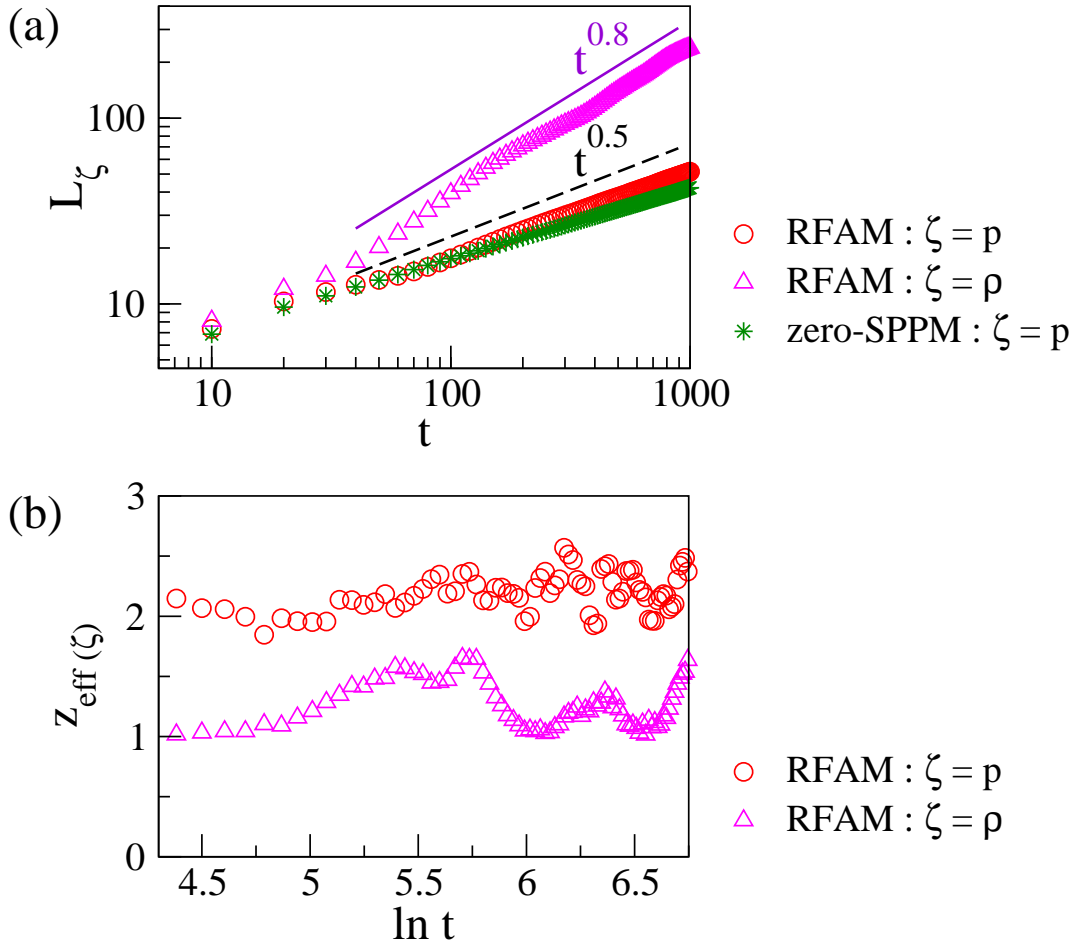


Figure 3.4: (a) Growth law of the hydrodynamic variables in the clean ($\Delta = 0$) system. The self-propelled speed $v_s = 0.5$ for the random field active model (RFAM), whereas $v_s = 0$ for the zero-SPP model (zero-SPPM). The straight lines are drawn for the respectively indicated power-laws. (b) Plot of effective growth exponent of the hydrodynamic fields versus time in the clean system for the RFAM.

[101, 116–119]. This is attributed to the trapping of domain boundaries by sites of quenched disorder [101, 116, 117]. As most of the experimental systems contain disorder, here we investigate the effect of random-field disorder on coarsening in the SPPs. In Fig. 3.5, we show snapshots of the orientation (left panel) and the density (right panel) at time $t = 1000$ for different strength of disorder. We find that domain size decreases with increasing Δ . The effect of inhomogeneity in the system is also inferred from the polarisation two-point correlation function shown in Fig. 3.6(a). Consequently, the characteristic lengths $L_{p,\rho}$ decrease with Δ as shown in Figs. 3.7(a, b). In Fig. 3.6(b), we plot the two point correlation function C_p vs. scaled distance r/L_p for fixed time and different strengths of disorder $\Delta = 0.0, 0.1, 0.2$ and 0.6 . We find good scaling collapse of the correlation functions. This suggests that the

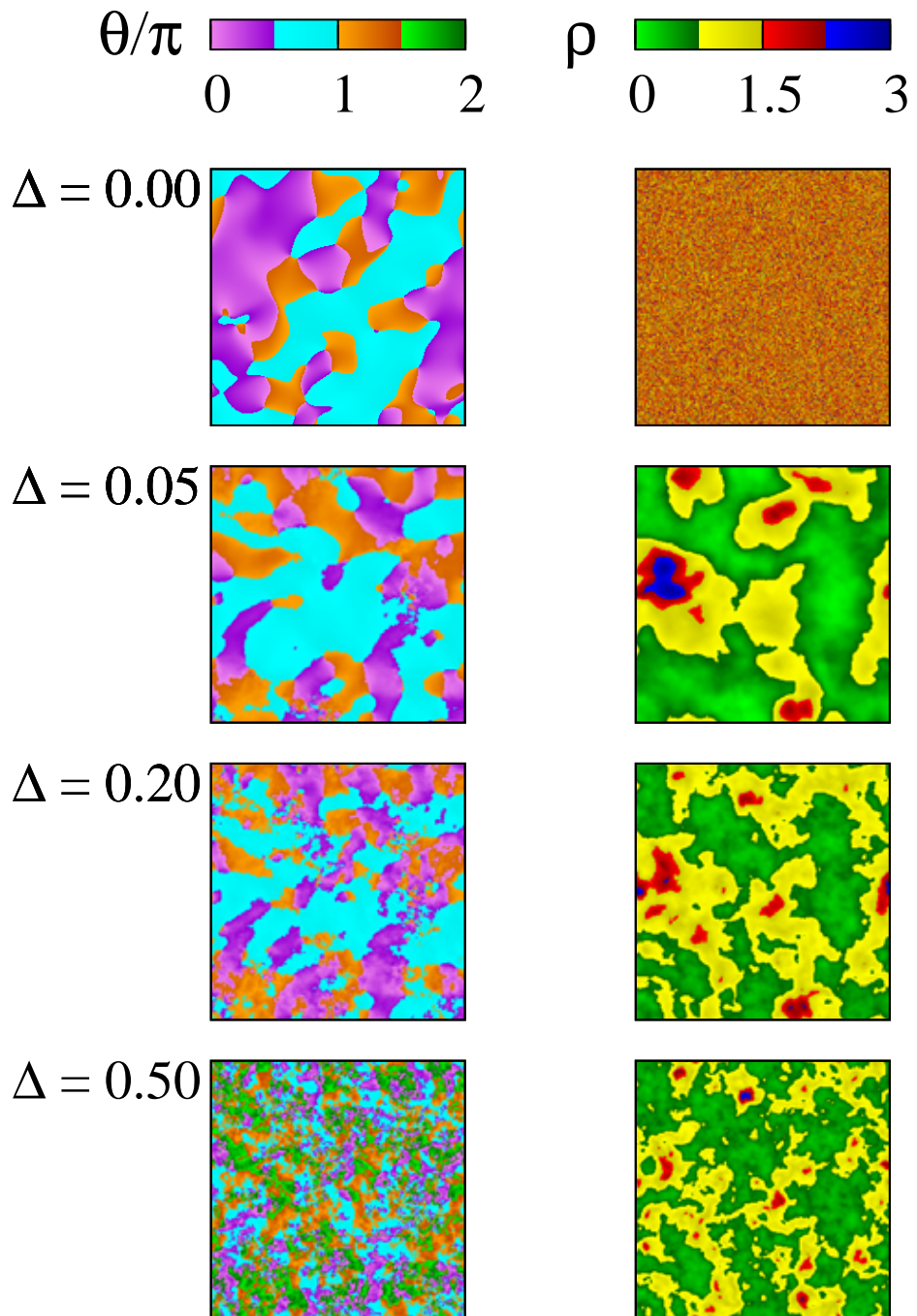


Figure 3.5: Heat map of (left panel) the orientation $\theta(r, t) = \tan^{-1} \left(\frac{p_y(r, t)}{p_x(r, t)} \right)$, and (right panel) the density, shown for fixed time $t = 1000$ and different disorder strengths Δ indicated on the left margin. Size of the ordered domains reduces with increasing strength of disorder.

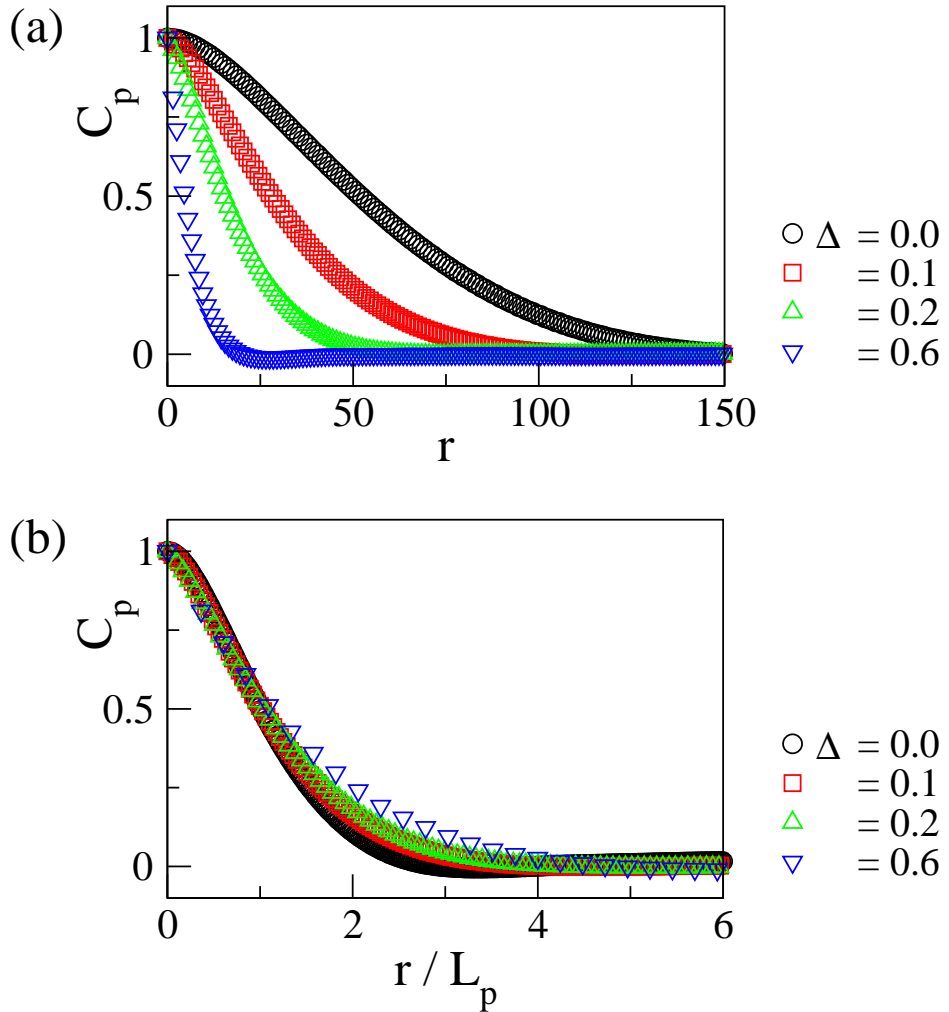


Figure 3.6: (a) Two-point correlation function for the polarisation, drawn for different disorder strengths at $t = 1000$. (b) shows scaling collapse of C_p as a function of r/L_p . Morphology of the polarisation field is approximately independent of disorder.

morphology of the polarisation field is approximately unaffected by disorder. However, this ‘super-universality’ [120] does not extend to the density field which does not even show simple dynamical scaling.

As stated before for the clean system, $z_{\text{eff}(p)}$ shows a mean value $\bar{z}_p(\Delta = 0) \sim 2$ for an extended range of time. In the RFAM, there is a preasymptotic regime with an effective exponent $\bar{z}_p(\Delta)$. As shown in Fig. 3.8(a), \bar{z}_p increases with Δ . Also the preasymptotic regime decreases with increasing Δ , and disappears for $\Delta > 0.4$. Beyond the mean growth exponent regime, $z_{\text{eff}(p)}(t, \Delta)$ increases sharply with time, that signifies pinning of the interfaces because of large disorder strength [91, 92].

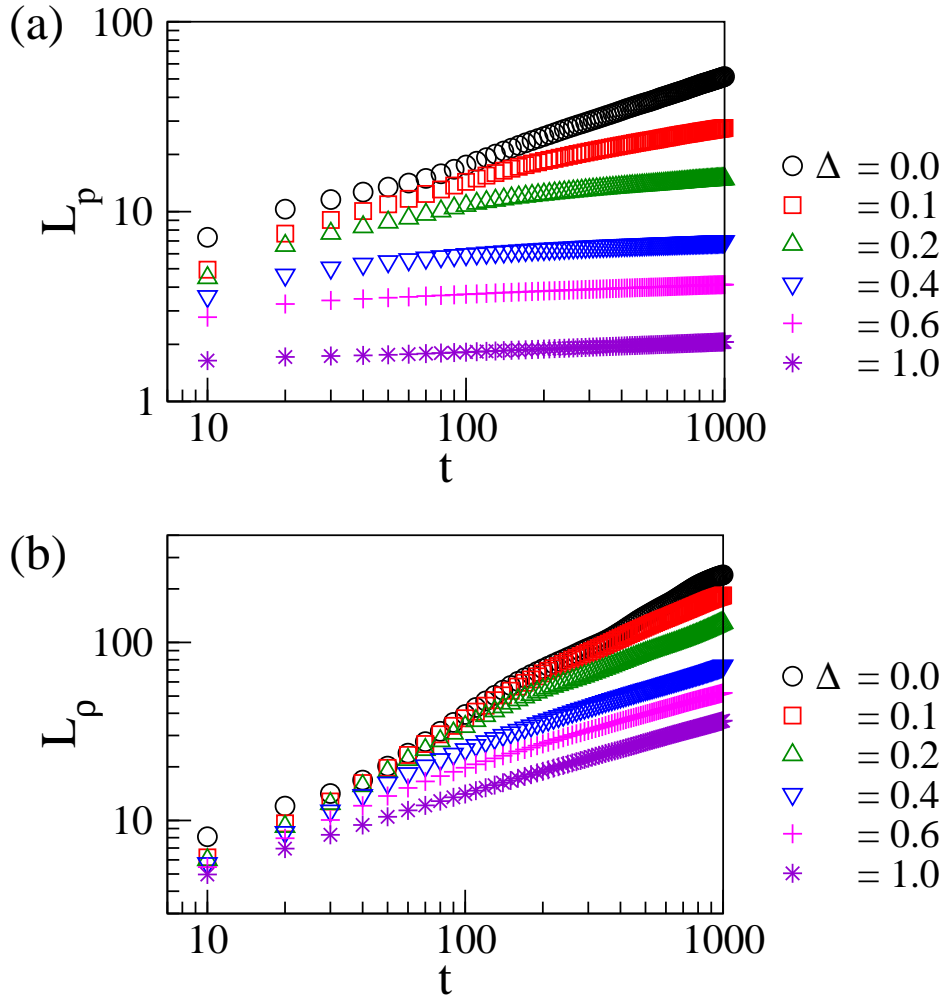


Figure 3.7: Growth law of the field variables - (a) the polarisation and (b) the density in the RFAM, drawn for different disorder strengths. In the disordered environments, the growth deviates from the power-law at late times.

For the density field, we find $z_{\text{eff}(\rho)}(t,0) \sim 1.2$ (not clean power-law). As we increase disorder strength, the effective growth exponent increases, but it does not show a clean power-law and fluctuates very much (data not shown). Hereafter, we characterise the growth law in the presence of disorder for the *polarisation field only*.

In the presence of disorder, we find a deviation from the power-law growth of the polarisation field. To analyse the effect of disorder, we use the method introduced by Corberi *et al.* [91, 92]. They propose the following scaling form for the growth law:

$$L(t, \Delta) \sim t^{1/z_{\text{eff}}} = t^{1/z} f(\Delta/t^\phi). \quad (3.6)$$

Here $z_{\text{eff}}(t, \Delta)$ represents the effective growth exponent, and ϕ is the crossover exponent. The scaling function $f(x)$ behaves as

$$f(x) \sim \begin{cases} \text{const.}, & \text{for } x \rightarrow 0, \\ x^{1/(z\phi)} \ell(x^{-1/\phi}), & \text{for } x \rightarrow \infty, \end{cases} \quad (3.7)$$

where $x = \Delta/t^\phi$. For $\phi < 0$, scaling form in Eq. (3.6) shows a crossover from the power-law $L \sim t^{1/z}$ to an asymptotic behaviour $L \sim \ell(t\Delta^{1/|\phi|})$. We evaluate the effective growth exponent for the polarisation field using the relation $t = L^z g(L/\lambda)$ where the crossover length scale $\lambda = \Delta^{1/\phi z}$, and $g(y) = [f(x)]^{-z}$ with $y = L/\lambda$. Then the effective growth exponent is represented as a function of y as

$$z_{\text{eff}}(y) = \frac{\partial \ln t}{\partial \ln L} = z + \frac{\partial \ln g(y)}{\partial \ln y}. \quad (3.8)$$

In Fig. 3.8(a), we show the time dependence of $z_{\text{eff}(p)}(t, \Delta)$ for $\Delta = 0.05, 0.1, 0.2$ and 0.4 . For the clean system, we find that $z_{\text{eff}(p)}$ is close to 2, as shown in Fig. 3.4(b). For non-zero Δ , the plots show $z_{\text{eff}(p)} \simeq \bar{z}_p$ for sufficient range of time. \bar{z}_p is a disorder-dependent constant. This is followed by late time regime where $z_{\text{eff}(p)}$ is time-dependent. This scenario seems to be a common feature of domain growth in disordered systems as shown in Ref. [92]. Hence we can write Eqs. (3.6), (3.7) and (3.8) by replacing $z \rightarrow \bar{z}$.

Now we study the dependence of z_{eff} on L . From Eq. (3.8), we can say that $z_{\text{eff}} - \bar{z}$ only depends on $y = L/\lambda$. In Fig. 3.8(b), we plot $z_{\text{eff}(p)} - \bar{z}_p$ vs. L_p/λ_p for various disorder values. We choose different λ_p values for different Δ to ensure the data collapse. The corresponding values of λ_p and \bar{z}_p for different Δ are listed in table 3.1. The solid curve in Fig. 3.8(b) is the best-fit to the power-law form

$$z_{\text{eff}} - \bar{z} = by^\varphi \quad (3.9)$$

with $b = 0.193$ and $\varphi = 8.86$. In Fig. 3.8(c), we show the Δ dependence of λ_p , which is fitted by $\lambda_p \sim \Delta^{-0.72}$. The negative exponent implies that the disorder is indeed a relevant

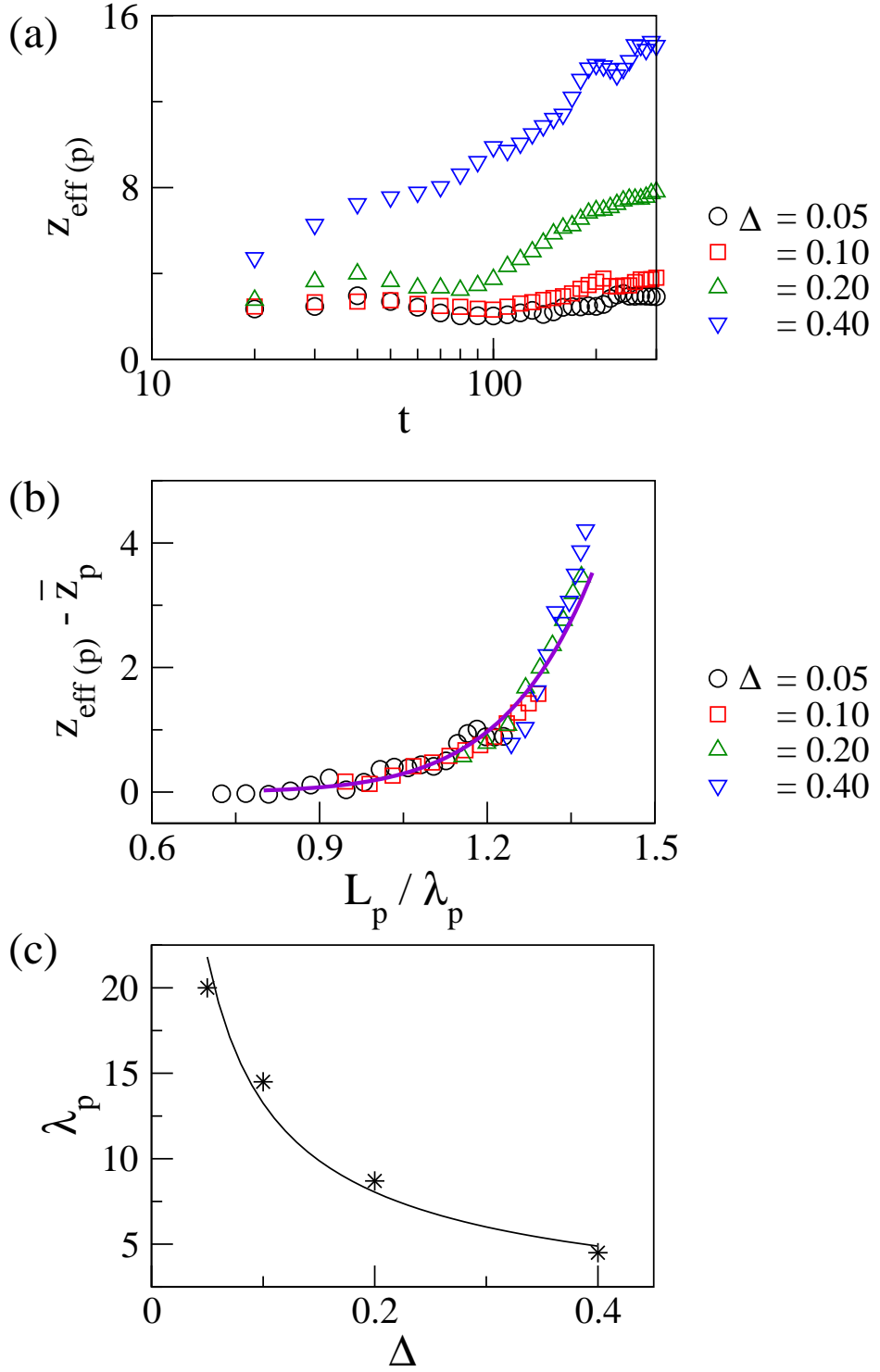


Figure 3.8: (a) Time variation of the effective growth exponent of the polarisation field in the RFAM, shown for different disorder strengths. (b) The scaling collapse of $z_{\text{eff}}(p) - \bar{z}_p$ versus L_p / λ_p . The best fit $z_{\text{eff}}(p) - \bar{z}_p \simeq 0.193(L_p / \lambda_p)^{8.86}$ is shown by the solid line. (c) Disorder dependence of λ_p . The solid line shows a power-law fit $\lambda_p \sim \Delta^{-0.72}$.

Table 3.1: Parameters \bar{z}_p and λ_p in the RFAM with different Δ values.

Δ	0	0.05	0.10	0.20	0.40
\bar{z}_p	2.0	2.06	2.60	3.40	6.50
λ_p	∞	20.0	14.50	8.70	4.50

scaling field. From Eq. (3.9) it is easy to confirm the logarithmic domain growth. The scaling function $g(y)$ can be evaluated by

$$\frac{\partial \ln g(y)}{\partial \ln y} = by^\varphi \Rightarrow g(y) \sim \exp\left(\frac{b}{\varphi}y^\varphi\right). \quad (3.10)$$

Substituting for $g(y)$ in Eq. (3.8) gives the asymptotic logarithmic growth form:

$$\frac{L}{\lambda} \simeq \left[\frac{\varphi}{b} \ln(t/\lambda^z)\right]^{1/\varphi}. \quad (3.11)$$

The exponent φ has important physical significance in domain-growth studies as it measures how the trapping barriers scale with domain size. We find $\varphi = 8.86$ in our RFAM.

3.4 DISCUSSION

In summary, we have studied ordering dynamics in a collection of polar self-propelled particles in an inhomogeneous medium. We use a coarse-grained model where inhomogeneity is introduced as an external disorder field, which is quenched in time and random in space. The strength of disorder is tuned from $\Delta = 0$ to 1.0 and kept fixed during the evolution of the system.

When the system is quenched from a random isotropic state, both the density and the polarisation fields coarsen with time. In the clean system, *i. e.*, for $\Delta = 0$, the polarisation field follows the power-law growth $L_p(t) \sim t^{0.5}$, while the density field approximately grows as $L_\rho(t) \sim t^{0.8}$. We find that the polarisation shows dynamical scaling, whereas the density does not. This indicates that the approach towards the ordered state for the density field is no longer controlled by a single energy scale associated with the cost of a domain wall.

The presence of disorder slows down the growth rate of the hydrodynamic fields. For intermediate time, domains of the polarisation field follow a power-law growth $L_p(t, \Delta) \sim t^{1/\bar{z}_p(\Delta)}$ with a disorder-dependent exponent $\bar{z}_p(\Delta)$. At late times, the polarisation field shows a crossover to logarithmic growth $L_p(t, \Delta) \sim (\ln t)^{1/\varphi}$, where the exponent φ does not depend on disorder. We find the logarithmic exponent is $\varphi = 8.86$ for our two-dimensional RFAM. For large Δ , the local polarisation remains pinned in the direction of the quenched random field. However, we could not find clean growth law for the density field. The scaling function for $C_p(r, t)$ is approximately independent of disorder, showing that the morphology of the polarisation field is relatively unaffected by disorder.

In our present study, we find that the disorder plays an important role in the phase ordering dynamics and scaling in a collection of SPPs. Our study provides novel insights on ordering dynamics in a collection of active polar particles in clean as well as disordered environments. The disorder we introduce in our model is analogous to random fields introduced in usual spin systems. It would be interesting to study the effects of other kinds of disorder on ordering dynamics in the active systems.

POLAR FLOCK IN THE PRESENCE OF RANDOM QUENCHED ROTATORS

4.1 INTRODUCTION

Steady-state properties of the polar SPPs in inhomogeneous medium have been recently addressed by many theoretical and experimental groups [95–99], as we have already discussed in Sec. 1.7.2. While commenting about these studies, Reichhardt and Reichhardt [102] stress upon the understanding of the flocking phenomena in the presence of different kinds of inhomogeneities. In a similar spirit, we study the effect of rotator-type obstacles on the nature of ordering in the polar SPPs. Moreover, we propose a minimal model for the polar SPPs in inhomogeneous medium that can easily be compared with its well-studied equilibrium counterparts [85, 86].

In this chapter¹, we introduce a Vicsek-like model [31] for the polar SPPs in the presence of obstacles in the medium. The obstacles are modeled as random quenched rotators which rotate the orientation of neighbouring SPPs by an angle determined by intrinsic orientations of the rotators. The model can be visualised as in a large moving crowd, some random ‘road-signs’ have been placed. Individual ‘road-sign’ dictates the neighbouring people to take a roundabout by a certain angle from their direction of motion. The specific issue we address here is the correlation of this collective motion in the presence of these random ‘road-signs’.

In the limit of zero self-propulsion speed, our model reduces to the XY-model [20] with random quenched obstacles. In the XY-model, any finite amount of quenched randomness

¹ The work reported in this chapter is based on the pre-print “Polar flock in the presence of random quenched rotators”, Rakesh Das, Manoranjan Kumar and Shradha Mishra, arXiv:1802.08861v2 [cond-mat.stat-mech].

is enough to destroy the orientationally ordered state in dimension $d \leq 4$ [85, 86]. Therefore in two dimensions (2D), an equilibrium system with quenched obstacles does not have any ordered state. Analogous to this, we show that in 2D polar self-propelled system, quenched rotators destroy the long range order (LRO) that usually found in the clean system.

We have organised this chapter as follows. The microscopic model mentioned above is defined in Sec. 4.2. Technique for simulating the model and choices of the model parameters are given in Sec. 4.3. Our numerical results show that small density of quenched rotators leads the the system to a quasi-long range order (QLRO) state. In this QLRO state, the absolute value of average normalised velocity V decreases algebraically with the system size. Also, fluctuation in the orientations of the SPPs increases logarithmically with system size. We present these results in Sec. 4.3.1. This QLRO state survives upto a critical density c_{rc} of the rotators, below which V and fluctuation in orientations of the SPPs show nice scaling collapse with scaled system size, as described in Sec. 4.3.2. In Sec. 4.3.3 we show that increase in the density of the rotators beyond c_{rc} introduces a continuous transition from the QLRO to a disorder state. We construct a phase diagram in noise vs. density of rotators plane indicating the QLRO and the disorder state regimes. The hydrodynamic equations of motion (EOMs) for the above model is introduced in Sec. 4.4. A linearised study of these equations suggests an extra $1/q^2$ divergence in the equal-time spatially Fourier transformed correlation functions of the hydrodynamic fields in the $q \rightarrow 0$ limit. We argue that such divergence destroys the usual LRO of the clean SPPs and leads the system to the QLRO state. We close this chapter in Sec. 4.5 with a brief summary of results, a comparative discussion with the microscopic model introduced by Chepizhko *et al.* [95], and illuminating experimental scope of our model.

4.2 MODEL

We consider a collection of N_s polar SPPs distributed over a 2D square substrate. Each particle moves with a fixed speed v_s along its orientation ϕ . Individual SPP tries to reorient itself along the mean orientation of all the neighbouring SPPs (including itself) within an interaction radius R_s , though ambience noise leads to orientational perturbation. Moreover, there

are N_r immobile rotators randomly distributed on the substrate. Each rotator possesses an intrinsic orientation φ , which can take any random value in the range $[-\pi, \pi]$ and remains fixed. Therefore, the rotators are quenched in time, and we call these as random quenched rotators (RQRs). Each RQR rotates the orientations of the SPPs within an interaction radius R_r by an angle determined by φ and SPP-RQR interaction strength μ . The update rules governing position \mathbf{r}_i and orientation ϕ_i of the i^{th} SPP are as follows:

$$\mathbf{r}_i(t+1) = \mathbf{r}_i(t) + \mathbf{v}_i(t), \quad (4.1)$$

$$\phi_i(t+1) = \langle \phi_j(t) \rangle_{j \in R_s} + \mu \langle \varphi_j \rangle_{j \in R_r} + \Delta\psi, \quad (4.2)$$

where $\mathbf{v}_i(t) = v_s (\cos \phi_i(t), \sin \phi_i(t))$ is the velocity of the particle i at time t , $\langle \phi \rangle_{R_s}$ and $\langle \varphi \rangle_{R_r}$ represent the mean orientation of all the SPPs and the RQRs, respectively, within the interaction radii. Fluctuation in orientation of the SPPs because of ambience noise is represented by an additive noise term $\Delta\psi$ distributed within $\eta [-\pi, \pi]$, where noise strength $\eta \in [0, 1]$. We call this model as ‘active model with quenched rotators’ (AMQR), which reduces to the celebrated Vicsek model (VM) [31] for $\mu = 0$ or in the clean system, *i. e.*, for $N_r = 0$.

4.3 NUMERICAL STUDY

We numerically simulate the collection of N_s SPPs spread over a $L \times L$ ($L \in [50, 300]$) 2D substrate with periodic boundary condition. Initially the particles are chosen to have random velocity, but with constant speed v_s . The density of the SPPs is defined as $c_s = N_s/L^2$. Similarly, the density of the RQRs is given by $c_r = N_r/L^2$. We distribute these rotators uniformly on the substrate, and randomly assign intrinsic orientation $\varphi \in [-\pi, \pi]$. The position and the velocity of all the SPPs in the collection are updated simultaneously following Eqs. (4.1)-(4.2). At every time step we use OpenMP Application Program Interface for parallel updation procedure of all the SPPs.

We consider $c_s = 1.0$, $v_s = 1.0$, $\mu = 1.0$, and for simplicity we take $R_s = R_r = 1$. In the absence of the rotators [31], the system shows disorder to order transition with decreas-

ing noise strength η . The ordering in the system is measured in terms of the conventional absolute value of the average normalised velocity [31]

$$V = \left\langle \frac{1}{N_s v_s} \left| \sum_{i=1}^{N_s} v_i \right| \right\rangle \quad (4.3)$$

of the entire system. Here $\langle \cdot \rangle$ indicates an average over many realisations and time in steady-state. V varies from zero to unity for disorder to order state transition. For the reported data, we start the averaging of observables after 3×10^5 updates to assure reaching the steady-state, and averaging is done for next 5×10^5 updates. Upto 30 realisations are used For better averaging.

4.3.1 Quasi-long range order

For a fixed η we calculate V for different c_r and study its variation with system size. As shown for $\eta = 0.1$ in Fig. 4.1(a), V does not change with system size in the clean system; consequently, the system possesses a non-zero V in the thermodynamic limit. Therefore, the clean system remains in the LRO state, which agrees with earlier prediction by Toner and Tu [29]. However, in the presence of the RQRs, V decreases algebraically with N_s following a relation

$$V = \mathcal{A}(c_r) N_s^{-\nu(c_r)}, \quad (4.4)$$

as shown in Fig. 4.1(a)-(b). Both \mathcal{A} and ν are functions of the rotator density for a fixed noise strength. Therefore, in the thermodynamic limit, V of the system with RQRs reduces to zero. We stress that the system remains in a QLRO state for small c_r , beyond which the AMQR shows a continuous QLRO-disorder state transition, as we will see shortly. In Fig. 4.2 we show snapshots of the orientation and the local density of the SPPs for $\eta = 0.1$ and different c_r . For $c_r = 0$ all the particles are in highly ordered state. RQRs perturb the LRO flocking as shown for $c_r = 0.005, 0.01$. For high density $c_r = 0.02$, the SPPs remain highly disordered.

We further study the fluctuation in the orientation of the SPPs. Width of a normalised distribution $P(\phi)$ of orientation of the SPPs provides a measure of this fluctuation. It is

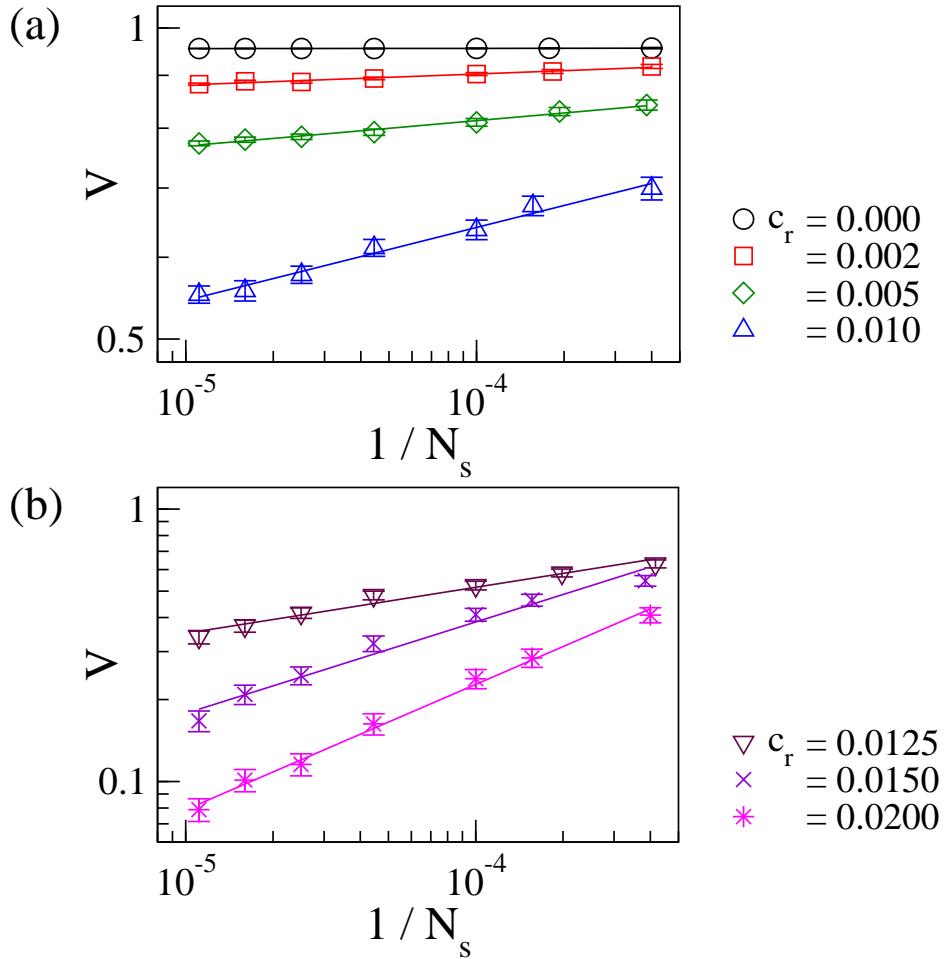


Figure 4.1: V versus $1/N_s$ plots in the (a) ordered and (b) disordered state for $\eta = 0.10$. The error bars indicate standard error in mean. The solid lines show the respective algebraic fits.

calculated by averaging over the distributions at every time step in the steady-state, and also over many realisations. We set the mean orientation of all the distributions at $\phi = 0$ for averaging.

We note that $P(\phi)$ widens with the increasing density of RQRs. This is quite intuitive since the degree of disorder increases with c_r . We fit these distributions with Voigt profile, which is defined as the convolution of the Gaussian and the Lorentzian functions [121]. A brief discussion of Voigt profile and the procedure used to fit $P(\phi)$ with it are provided in Appendix 4.A. From the respective fits, we calculate the full width at half maximum (FWHM) f of the distributions.

We note that, in the clean system, $P(\phi)$ does not change with system size. However, for any fixed $c_r > 0$, $P(\phi)$ widens with increasing system size, as shown in Fig. 4.3(a) for $(\eta, c_r) =$

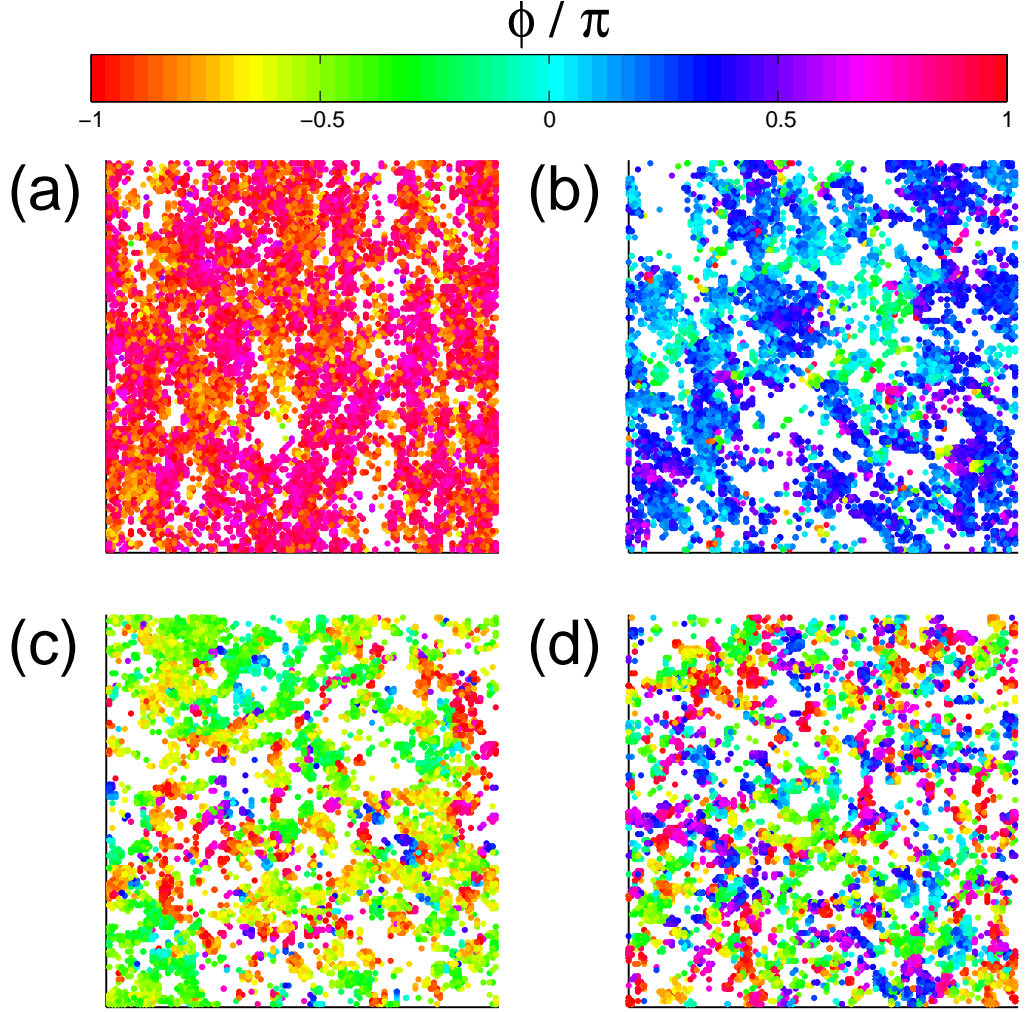


Figure 4.2: Steady-state snapshots are shown for $\eta = 0.10$, $L = 150$. (a - d) are drawn for $c_r = 0, 0.005, 0.01$ and 0.02 , respectively. The colour bar indicates orientation of the SPPs. The rotators with random intrinsic orientation are not shown for the sake of clarity of the figures.

(0.10, 0.005). In Fig. 4.3(b), we show the variation of f with system size for different c_r . f does not change with N_s for $c_r = 0$. Therefore, in the clean system, the fluctuation in the orientation of the SPPs does not depend on the system size, and the system is in the LRO state. However, for $c_r > 0$, FWHM of $P(\phi)$ follows the relation $f = g_1(c_r) + g_2(c_r) \ln(N_s)$, where both g_1 and g_2 are functions of c_r . Since $g_2 \geq 0$, f increases logarithmically with N_s , which further confirms the QLRO in the AMQR.

We should stress that, in the clean system, $P(\phi)$ is always independent of the system size; no matter the system is in the homogeneous ordered state or in the banded state. It is evident

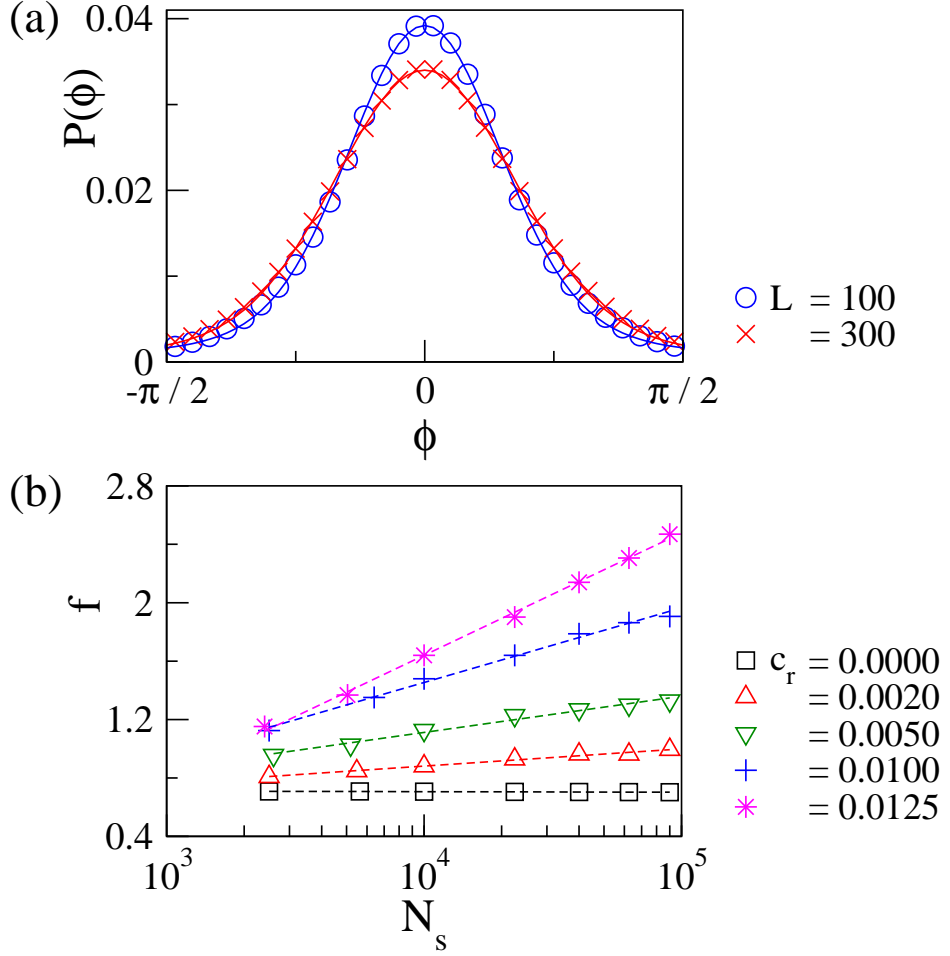


Figure 4.3: (a) Distribution $P(\phi)$ of the orientation of the SPPs is shown for $\eta = 0.10$ and $c_r = 0.005$. The curves are zoomed into the range $\phi \in [-\pi/2, \pi/2]$ for better visibility. The solid lines show the respective fits with Voigt profile. (b) Plot of the FWHM f of $P(\phi)$ versus N_s . In the presence of quenched rotators, f increases logarithmically with N_s . The dashed lines show respective fits.

from Fig. 4.4(a) where we plot $P(\phi)$ for the banded state ($\eta = 0.40$). However, in the presence of the random quenched rotators, $P(\phi)$ widens with system size, as shown in Fig. 4.4(b).

4.3.2 Scaling

We plot V versus scaled system size $N_s/N_s^{\gamma(c_r)}$ for $\eta = 0.1$ and different c_r in Fig. 4.5(a). Here $\gamma(c_r) \simeq 1 - kc_r$, where k is a positive constant. Moreover, $\nu = z(1 - \gamma)$, where z is a non-monotonic function of η . We note nice scaling collapse for $c_r \leq 0.0125$. This predicts that, for $c_r \leq 0.0125$, the system can be divided into sub-systems of size $N_s^{\gamma(c_r)}$ within which

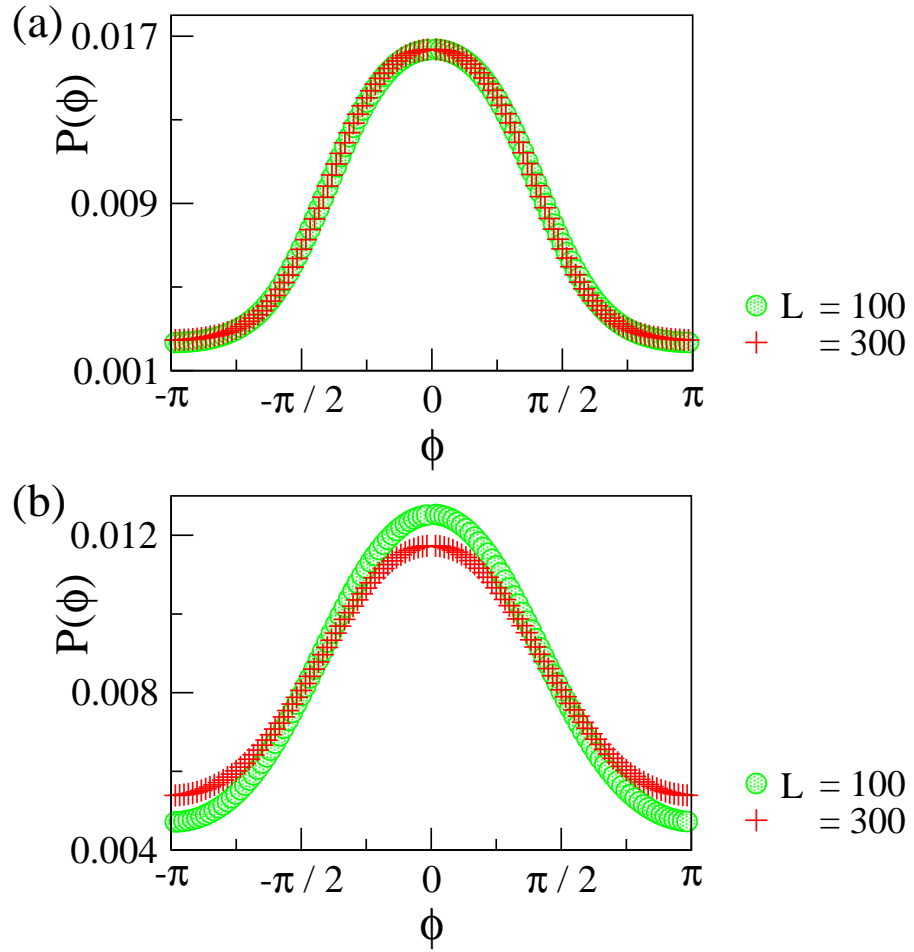


Figure 4.4: Plot of orientation distribution $P(\phi)$ of the SPPs for $\eta = 0.40$. In the clean system, *i. e.*, for $c_r = 0$, the system remains in the banded state. As shown in (a), $P(\phi)$ does not change with system size in this state. However, as shown in (b) for $c_r = 0.008$, fluctuation in V increases with system size. Respective fits with Voigt profile has not been shown for the sake of clarity of the plots.

the SPPs remain ordered. Since $\gamma = 1$ for $c_r = 0$, V does not depend on the system size, and therefore the clean system remains in the LRO state. However, in the presence of the RQRs, the system remains in the QLRO state. This scaling also predicts self-similarity of the system for different $c_r \leq 0.0125$. As shown in Fig. 4.5(b), we also find nice scaling collapse of $f - g_1(c_r)$ with scaled system size $N_s/N_s^{\Gamma(c_r)}$ for different $c_r \leq 0.0125$, where $\Gamma = 1 - g_2(c_r)$ that varies linearly with c_r for small c_r . Similar scaling holds for other η values in the QLRO state.

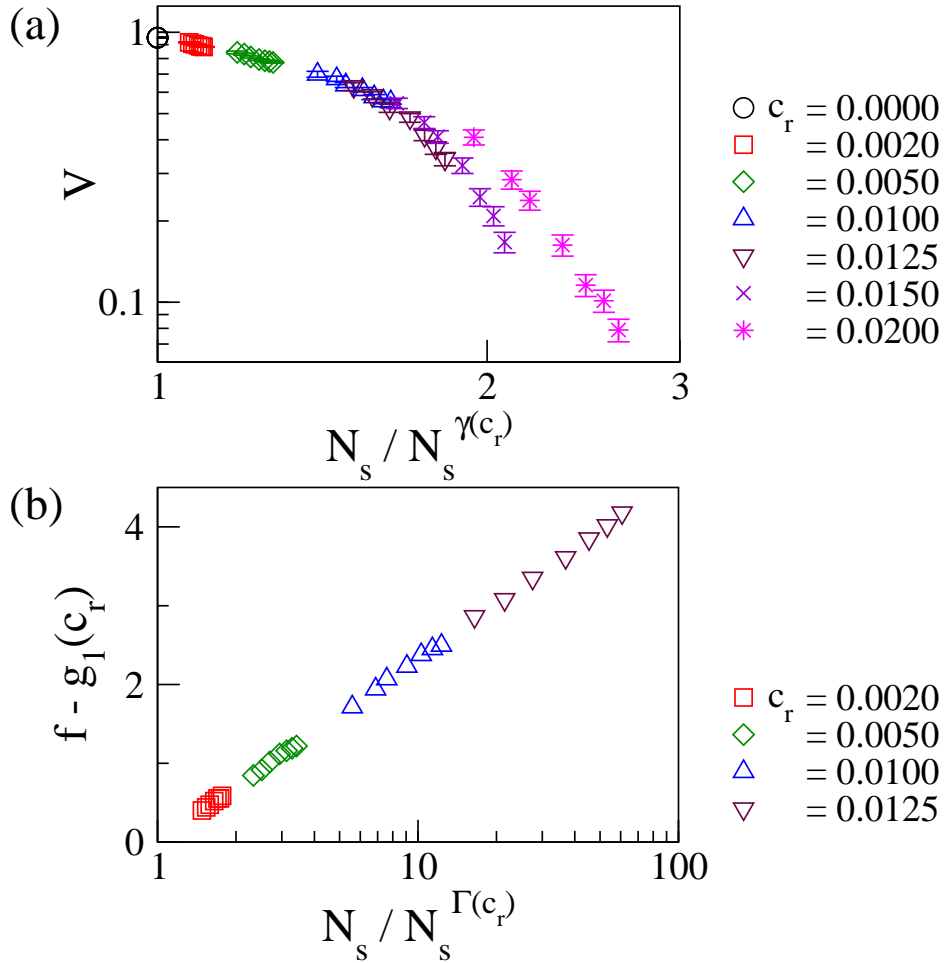


Figure 4.5: (a) Plot of V versus scaled system size N_s/N_s^γ on log-log scale, where γ is a function of c_r . The data shows good scaling for $0 < c_r \leq 0.0125$, but deviates for $c_r \geq 0.0125$. (b) Plot of shifted FWHM $f - g_1(c_r)$ with scaled system size N_s/N_s^Γ , where both g_1 and Γ are functions of c_r . The scaling holds good for $c_r \leq 0.0125$.

4.3.3 Transition from quasi-long range order to disorder state

The variation of V with c_r is shown in Fig. 4.6(a) for $\eta = 0.1$ and different system sizes. Starting from the value of V close to 1 for small c_r , V decreases to smaller values with increasing c_r . Therefore, with increasing c_r , QLRO-disorder transition takes place in the system. We further calculate the variance χ of V for different system sizes, and plot these as a function of c_r in Fig. 4.6(b). Data shows a peak in χ as a function of c_r where fluctuation is large. The position of the peak shifts from $c_r = 0.016$ to 0.0125 as we increase the system size from $L = 100$ to 300. The critical density $c_{rc}(L)$ of the QLRO-disorder state transition for the system size L is obtained from the position of the peak in χ versus c_r plot. We plot V as function

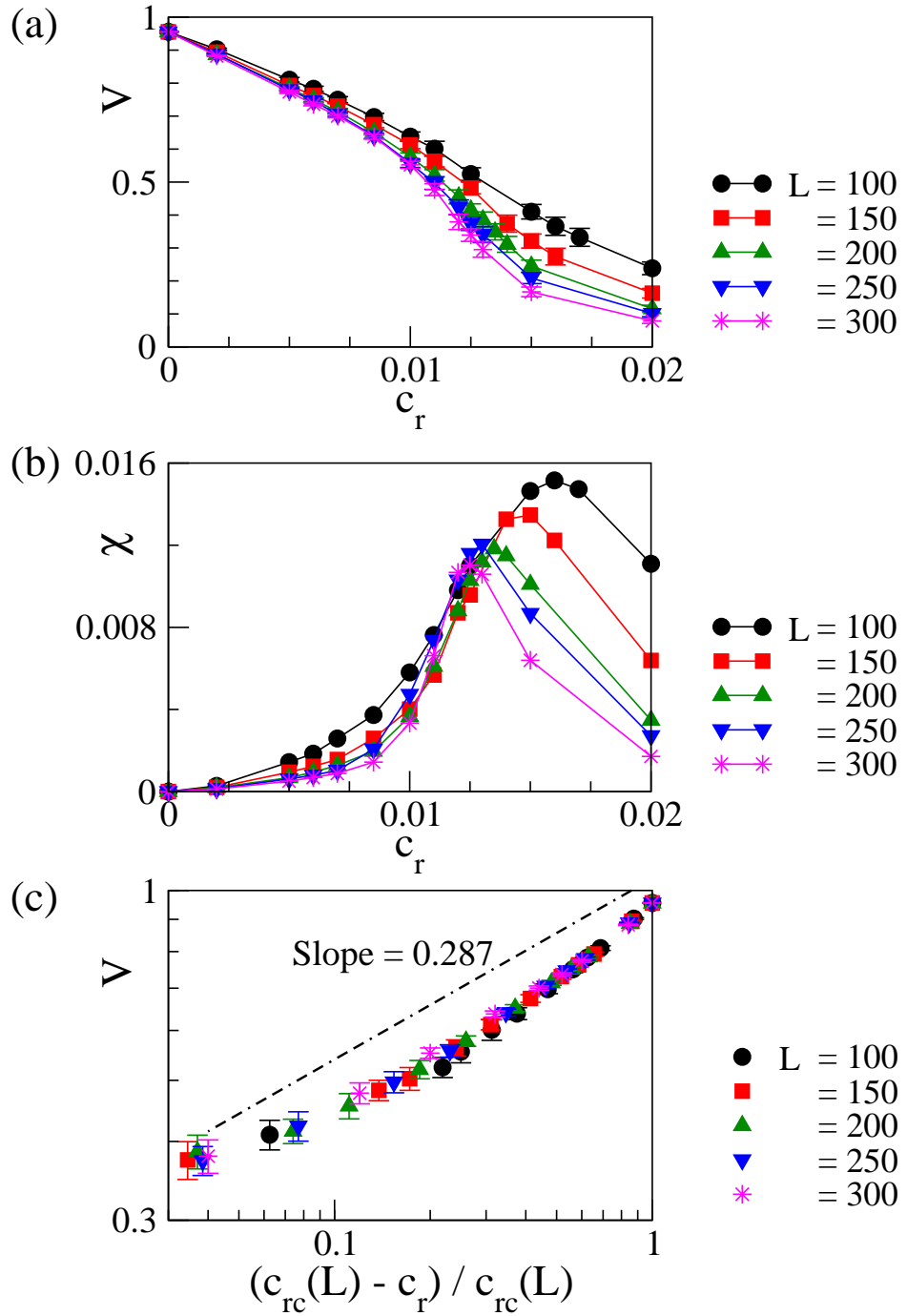


Figure 4.6: (a) Variation of V with c_r shown for different system sizes and $\eta = 0.10$. (b) Variance χ of V plotted with c_r . The peaks in the curves indicate the critical density of rotators $c_{rc}(L)$ for the QLRO-disorder transition for the respective system sizes. (c) V shows good scaling with reduced density of rotators $c(L) = (c_{rc}(L) - c_r) / c_{rc}(L)$ for $c_r \leq c_{rc}$ for all system sizes. The dashed line shows the scaling $V \sim c^{0.287}$.

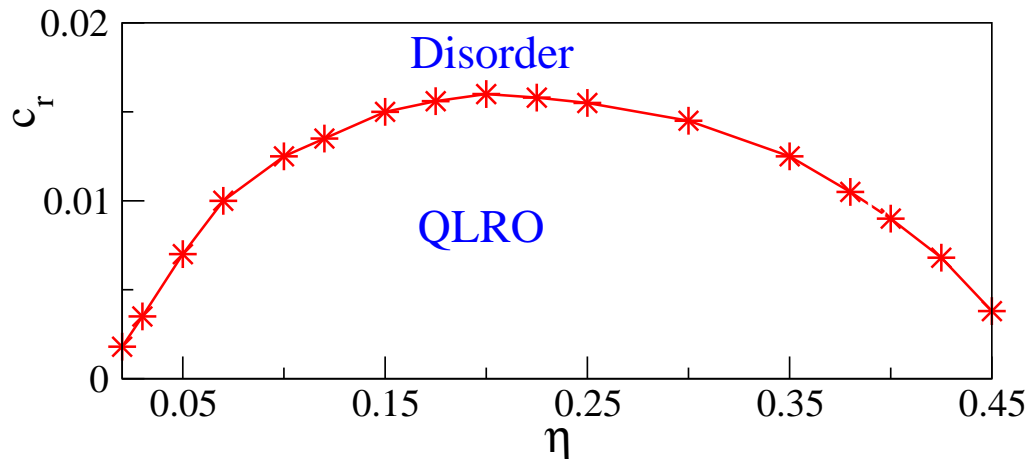


Figure 4.7: Phase diagram in noise strength versus density of rotator plane. For small c_r , the QLRO state prevails, beyond which the system continuously goes to the disorder state.

of reduced density of rotators $c(L) = (c_{rc}(L) - c_r)/c_{rc}(L)$ in Fig. 4.6(c), and note that the data for all system sizes merge onto each other. We find a good scaling as $V \sim c^\delta$, where $\delta \approx 0.287$. Similar scaling is noted for other η values also, where δ varies between 0.28 and 0.35. In analogy of the exponent β in the usual equilibrium models [20], we anticipate δ close to $1/3$. This suggests a continuous QLRO-disorder state transition in the AMQR. We note that for all η values, $c_{rc}(L)$ flattens on increasing L . Therefore, using the extrapolated values $c_{rc}(L \rightarrow \infty)$, we construct a phase diagram in the noise strength versus density of rotator plane. We stress that in the presence of RQRs, the system remains in the QLRO below the phase boundary shown in Fig. 4.7.

4.4 LINEARISED HYDRODYNAMICS

We introduce the hydrodynamic EOMs of the relevant field variables for the AMQR in this section. Since the AMQR reduces to the VM in the absence of the RQRs, we adopt the hydrodynamic EOMs introduced by Toner and Tu [29, 49] for the coarse-grained density $\rho(\mathbf{r}, t)$ of SPPs and the velocity field $\mathbf{v}(\mathbf{r}, t)$. The velocity field $\mathbf{v}(\mathbf{r}, t)$ is a broken symmetry parameter analogous to the polarisation field $\mathbf{p}(\mathbf{r}, t)$ introduced in Sec. 1.4.3, and they are

related by $\mathbf{v}(\mathbf{r}, t) = v_0 \mathbf{p}(\mathbf{r}, t)$, where v_0 is the average speed of the flock. We introduce the effect of the quenched randomness in the Toner-Tu model by a field $\zeta(\mathbf{r}, t)$ with correlations

$$\langle \zeta_i(\mathbf{r}, t) \zeta_j(\mathbf{r}', t') \rangle = \zeta^2 \delta_{ij} \delta(\mathbf{r} - \mathbf{r}'), \quad (4.5)$$

where dummy indices i and j represent Cartesian components. Therefore, the hydrodynamic EOMs of the polar SPPs with quenched randomness take forms as follows:

$$\begin{aligned} \partial_t \rho + \nabla \cdot (\mathbf{v} \rho) &= D_\rho \nabla^2 \rho, & (4.6) \\ \partial_t \mathbf{v} + \lambda_1 (\mathbf{v} \cdot \nabla) \mathbf{v} + \lambda_2 (\nabla \cdot \mathbf{v}) \mathbf{v} + \lambda_3 \nabla (v^2) \\ &= (\alpha_1 - \alpha_2 v^2) \mathbf{v} - \nabla P + D_B \nabla (\nabla \cdot \mathbf{v}) + D_T \nabla^2 \mathbf{v} \\ &+ D_2 (\mathbf{v} \cdot \nabla)^2 \mathbf{v} + \frac{\rho_o}{\rho} \zeta + \mathbf{f}, & (4.7) \end{aligned}$$

where ρ_o represents density of obstacles. As compared to the polarisation Eq. (1.11), here we have discarded equal elastic constant approximation, and therefore all possible types of diffusion terms are written in Eq. (4.7). The ∇P term on the RHS of Eq. (4.7) represents the pressure, similar to the $\nabla \rho$ term in Eq. (1.11). \mathbf{f} represents the annealed noise term that provides a random driving force. We assume this to be a white Gaussian noise with the correlation

$$\langle f_i(\mathbf{r}, t) f_j(\mathbf{r}', t') \rangle = \Delta \delta_{ij} \delta(\mathbf{r} - \mathbf{r}') \delta(t - t') \quad (4.8)$$

where Δ is a constant. For $\zeta = 0$, the set of Eqs. (4.6)-(4.8) represents the Toner-Tu [29] model.

Now we check whether a broken symmetry state of the SPPs in the presence of the obstacle field survives to small fluctuation in the hydrodynamic fields. In the hydrodynamic limit, a linearised study of Eqs. (4.6)-(4.7) alongwith the correlations in Eqs. (4.5) and (4.8) gives spatially Fourier transformed equal-time correlation functions for the density

$$C_{\rho\rho}(\mathbf{q}, t) = \frac{1}{q^2} \left\{ \frac{\zeta^2 \rho_o^2 a_\rho(\theta)}{b(\theta) q^2 + d(\theta)} + \Delta A_\rho(\theta) \right\}, \quad (4.9)$$

and the velocity

$$C_{vv}(\mathbf{q}, t) = \frac{1}{q^2} \left\{ \frac{\zeta^2 \rho_0^2 a_v(\theta)}{b(\theta)q^2 + d(\theta)} + \Delta A_v(\theta) \right\}. \quad (4.10)$$

The parameters $a_{\rho,v}$, $A_{\rho,v}$, b and d depend on the specific microscopic model and on the angle θ between the wave vector \mathbf{q} and the flocking direction. The detailed calculation for Eqs. (4.9)-(4.10) is given in Appendix 4.B. For $\zeta = 0$, our result matches with the earlier prediction by Toner and Tu [29], where the two structure factors diverges as $1/q^2$ for small q . However, for $\zeta \neq 0$, we find that the structure factors have strong direction dependence and possess another divergence of $\mathcal{O}(1/q^2)$ for small q . Appearance of such additional fluctuation break the usual LRO present in the clean system and leads the system to QLRO state in the presence of quenched inhomogeneities. Therefore, our linearised hydrodynamic calculation agrees with the numerical predictions for the AMQR. However, a dynamic renormalisation group [122] calculation would be helpful to understand the effect of nonlinearities.

4.5 DISCUSSION

In summary, we have studied the effect of random quenched rotators on the flocking state of the polar SPPs. These rotators are one kind of obstacles that rotate the orientation of the SPPs. We find that, for small density of the rotators, the usual LRO of the clean polar SPPs is destroyed, and a QLRO state prevails. With further increase in the density of the rotators, a continuous QLRO to disorder state transition takes place in the system. Our linearised hydrodynamical analysis predicts appearance of an extra $1/q^2$ divergence in the presence of quenched inhomogeneities that destroys the usual LRO of the polar SPPs in 2D. In equilibrium systems with random quenched obstacles, ordered state does not exist below four dimensions [85, 86]. However, as compared to the equilibrium systems, in our model for the polar SPPs with quenched rotators, we find QLRO in 2D. Our prediction of the QLRO in the polar SPPs in the presence of quenched obstacles agrees with recent observations [95, 123, 124].

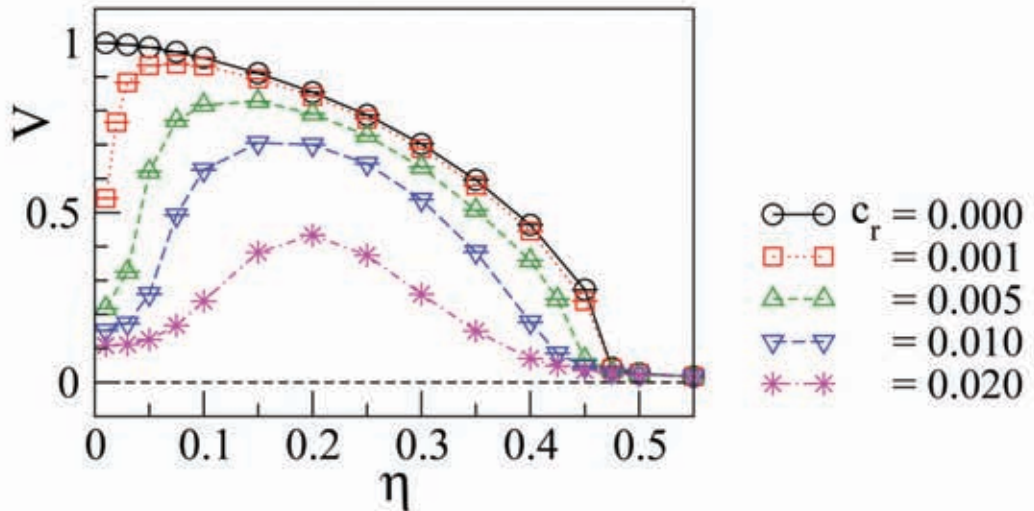


Figure 4.8: Plot of average normalised velocity versus noise strength shown for $L = 100$ and different density of the rotators. While V decreases monotonically with increasing η for the clean system, in the presence of the rotators, a certain amount of noise maximizes the ordering.

In contrast to the LRO at some non-zero finite density of obstacles in Ref. [95], we note QLRO only, because of the basic difference in the nature of obstacles. The force due to obstacles in Ref. [95] is a modulated function which depends on local density and velocity of the SPPs, whereas in our case it is completely random. However, similar to their results, we note the existence of an optimal noise for which the system attains the maximum ordering in the presence of quenched rotators. As shown in Fig. 4.8, V decays monotonically with increasing η in the clean system. Surprisingly, in the presence of the RQRs, a certain amount of noise facilitates flocking, and below that the ordering reduces again. This happens because, in the presence of the RQRs, the system must have a non-zero noise to transfer the information of one sub-flock to another. Our model can be applied in natural systems like a shoal of fishes moving in sea in the presence of vortices. An experiment on a collection of fishes living in a shallow water-pool [43, 125–127], in the presence of uncorrelated artificial vortices, may verify our predictions.

APPENDIX

4.A VOIGT PROFILE

Voigt profile is defined as

$$\mathcal{V}(\phi; \sigma, \epsilon) = \int_{-\pi}^{\pi} \frac{\exp(-\Phi^2/2\sigma^2)}{\sigma\sqrt{2\pi}} \frac{\epsilon}{\pi [(\phi - \Phi)^2 + \epsilon^2]} d\Phi, \quad (4.11)$$

where the Gaussian and the Lorentzian contributions are signified by the parameters σ and ϵ , respectively. The FWHM of the Voigt profile is approximately given by the relation [121]

$$f \approx 0.5346f_L + \sqrt{0.2166f_L^2 + f_G^2}, \quad (4.12)$$

where $f_L = 2\epsilon$ represents the FWHM of the Lorentzian distribution, and $f_G = 2\sigma\sqrt{2\ln 2}$ represents FWHM of the Gaussian distribution.

As mentioned in Sec. 4.3.1, we realise that the distribution $P(\phi)$ follows Voigt profile. So we take discrete Fourier transform (DFT) of $P(\phi)$ and fit the transformed distribution with the characteristic function $\zeta(n; \sigma, \epsilon) = \exp\left(\frac{\sigma^2 n^2}{2} - \epsilon|n|\right)$ of $\mathcal{V}(\phi; \sigma, \epsilon)$. Here n represents the Fourier conjugate of ϕ . From the fits in the Fourier space, we extract the values of the parameters σ and ϵ , and calculate the FWHM of $P(\phi)$ using Eq. (4.12). The fits shown in Fig. 4.3(a) are obtained by the inverse DFT of the fitted functions $\zeta(n; \sigma, \epsilon)$.

4.B LINEARISED THEORY OF THE BROKEN SYMMETRY STATE IN THE PRESENCE OF QUENCHED INHOMOGENEITIES

Given the EOMs of the hydrodynamic fields in Sec. 4.4, we check whether a broken symmetry state of the SPPs in the presence of the obstacle field survives to small fluctuations

in the hydrodynamic fields. We consider a broken symmetry state $\mathbf{v} = v_0 \hat{y} + \delta \mathbf{v}$, where the spontaneous average value of the velocity $\langle \mathbf{v} \rangle = v_0 \hat{y}$ and $v_0 = \sqrt{\alpha_1/\alpha_2}$. Fluctuation in the density field is given by $\delta \rho = \rho - \bar{\rho}$, where $\bar{\rho}$ represents the mean density of SPPs. We expand spatial and temporal gradients appearing in the EOMs, and retain upto lowest-order terms in derivatives, since we are interested in long-time and long-distance behaviour of the system. Doing so, we obtain the EOM for the fluctuation δv_y as

$$\partial_t \delta v_y + 2\alpha_1 \delta v_y = -\sigma_1 \partial_y \delta \rho + \frac{\rho_o}{\bar{\rho}} \zeta_y + \text{irrelevant terms.} \quad (4.13)$$

Since we are interested in hydrodynamic modes, *i. e.*, modes for which frequency $\omega \rightarrow 0$ as wave number $q \rightarrow 0$, we can neglect time-variation of δv_y as compared to its value. Therefore, from Eq. (4.13), we obtain the relation

$$\delta v_y = \frac{1}{2\alpha_1} \left(-\sigma_1 \partial_y \delta \rho + \frac{\rho_o}{\bar{\rho}} \zeta_y \right). \quad (4.14)$$

Using the expression for δv_y from Eq. (4.14), we obtain the EOMs for $\delta \rho$ and δv_x as

$$\left(\partial_t + v_0 \partial_y - D_{\rho y} \partial_y^2 - D_\rho \partial_x^2 \right) \delta \rho + \bar{\rho} \partial_x \delta v_x = -\frac{\rho_o}{2\alpha_1} \partial_y \zeta_y, \quad (4.15)$$

$$\sigma_1 \partial_x \delta \rho + \left(\partial_t + \gamma \partial_y - D_L \partial_x^2 - D_y \partial_y^2 \right) \delta v_x = \frac{\rho_o}{\bar{\rho}} \zeta_x + f_x, \quad (4.16)$$

where $D_{\rho y} = D_\rho + \bar{\rho} \sigma_1 / 2\alpha_1$, $D_L = D_B + D_T$, $D_y = D_T + D_2 v_0^2$ and $\gamma = \lambda_1 v_0$. These parameters depend on the scalar quantities v^2 and $\rho(\mathbf{r})$ whose fluctuations are small in the broken symmetry state. So, hereafter we consider these parameters as constants.

It is now instructive to Fourier transform the set of Eqs. (4.15)-(4.16) in space and time. Given a function $u(\mathbf{r}, t)$, its Fourier transform in space and time is defined as

$$u(\mathbf{q}, \omega) = \int_{-\infty}^{\infty} dt d\mathbf{r} e^{i\omega t} e^{-i\mathbf{q} \cdot \mathbf{r}} u(\mathbf{r}, t). \quad (4.17)$$

Using the above definition, we write the equations of motion for the fluctuations in the Fourier space as follow

$$[i(\omega - v_0 q_y) - \Gamma_\rho(\mathbf{q})] \delta\rho - i\bar{\rho}q_x \delta v_x = -i\frac{\rho_0}{2\alpha_1} q_y \zeta_y, \quad (4.18)$$

$$i\sigma_1 q_x \delta\rho + [-i(\omega - \gamma q_y) + \Gamma_L(\mathbf{q})] \delta v_x = \frac{\rho_0}{\bar{\rho}} \zeta_x + f_x, \quad (4.19)$$

where wave number dependent dampings are

$$\Gamma_\rho(\mathbf{q}) = D_\rho q_x^2 + D_{\rho y} q_y^2, \quad (4.20)$$

$$\Gamma_L(\mathbf{q}) = D_L q_x^2 + D_y q_y^2. \quad (4.21)$$

The normal modes of the pair of coupled Eqs. (4.18)-(4.19) are two propagating sound waves with complex eigenfrequencies

$$\omega_\pm = c_\pm(\theta)q - i\Gamma_L \left[\frac{v_\pm(\theta)}{2c_2(\theta)} \right] - i\Gamma_\rho \left[\frac{v_\mp(\theta)}{2c_2(\theta)} \right], \quad (4.22)$$

where θ is the angle between \mathbf{q} and the direction of flock, *i. e.*, \hat{y} -direction, and

$$c_\pm(\theta) = \frac{\gamma + v_0}{2} \cos\theta \pm c_2(\theta), \quad (4.23)$$

$$v_\pm(\theta) = c_2(\theta) \pm \frac{\gamma - v_0}{2} \cos\theta, \quad (4.24)$$

$$c_2(\theta) = \sqrt{\frac{1}{4}(\gamma - v_0)^2 \cos^2\theta + \sigma_1 \bar{\rho} \sin^2\theta}. \quad (4.25)$$

Solving the linear set of Eqs. (4.18)-(4.19) for $\delta\rho(\mathbf{q}, \omega)$ and $\delta v_x(\mathbf{q}, \omega)$, we obtain

$$\begin{bmatrix} \delta\rho(\mathbf{q}, \omega) \\ \delta v_x(\mathbf{q}, \omega) \end{bmatrix} = \begin{bmatrix} G_{\rho\rho}(\mathbf{q}, \omega) & G_{\rho L}(\mathbf{q}, \omega) \\ G_{L\rho}(\mathbf{q}, \omega) & G_{LL}(\mathbf{q}, \omega) \end{bmatrix} \begin{bmatrix} i\rho_0 \zeta_y q_y / 2\alpha \\ f_x + \rho_0 \zeta_x / \bar{\rho} \end{bmatrix} \quad (4.26)$$

where the propagators are

$$G_{\rho\rho}(\mathbf{q}, \omega) = \frac{-i(\omega - \gamma q \cos \theta) + \Gamma_L(\mathbf{q})}{[\omega - c_+(\theta)q][\omega - c_-(\theta)q] + i\omega [\Gamma_\rho(\mathbf{q}) + \Gamma_L(\mathbf{q})] - iq \cos \theta [\gamma\Gamma_\rho(\mathbf{q}) + v_0\Gamma_L(\mathbf{q})]}, \quad (4.27)$$

$$G_{\rho L}(\mathbf{q}, \omega) = \frac{i\bar{\rho}q \sin \theta}{[\omega - c_+(\theta)q][\omega - c_-(\theta)q] + i\omega [\Gamma_\rho(\mathbf{q}) + \Gamma_L(\mathbf{q})] - iq \cos \theta [\gamma\Gamma_\rho(\mathbf{q}) + v_0\Gamma_L(\mathbf{q})]}, \quad (4.28)$$

$$G_{L\rho}(\mathbf{q}, \omega) = \frac{-i\sigma_1 q \sin \theta}{[\omega - c_+(\theta)q][\omega - c_-(\theta)q] + i\omega [\Gamma_\rho(\mathbf{q}) + \Gamma_L(\mathbf{q})] - iq \cos \theta [\gamma\Gamma_\rho(\mathbf{q}) + v_0\Gamma_L(\mathbf{q})]}, \quad (4.29)$$

$$G_{LL}(\mathbf{q}, \omega) = \frac{i(\omega - v_0 q \cos \theta) - \Gamma_\rho(\mathbf{q})}{[\omega - c_+(\theta)q][\omega - c_-(\theta)q] + i\omega [\Gamma_\rho(\mathbf{q}) + \Gamma_L(\mathbf{q})] - iq \cos \theta [\gamma\Gamma_\rho(\mathbf{q}) + v_0\Gamma_L(\mathbf{q})]}. \quad (4.30)$$

Using the expression given in Eqs. (4.26)-(4.30) and the correlations given in Eqs. (4.5) and (4.8), we calculate correlation functions for the density and the velocity fields. Retaining upto lowest-order terms in q , we obtain density-density correlation function

$$C_{\rho\rho}(\mathbf{q}, \omega) = \frac{(\omega - \gamma q \cos \theta)^2 \left[-\frac{\rho_0^2}{4\alpha_1^2} \zeta^2 q^2 \cos^2 \theta \delta(\omega) \right] + \bar{\rho}^2 q^2 \sin^2 \theta \left[\Delta + \frac{\rho_0^2}{\bar{\rho}^2} \zeta^2 \delta(\omega) \right]}{[\omega - c_+(\theta)q]^2 [\omega - c_-(\theta)q]^2 + \left\{ \omega [\Gamma_\rho(\mathbf{q}) + \Gamma_L(\mathbf{q})] - q_y [\gamma\Gamma_\rho(\mathbf{q}) + v_0\Gamma_L(\mathbf{q})] \right\}^2}, \quad (4.31)$$

and velocity-velocity correlation function

$$C_{vv}(\mathbf{q}, \omega) = \frac{-\sigma_1^2 \zeta^2 q^4 \sin^2 2\theta \frac{\rho_0^2}{16\alpha_1^2} \delta(\omega) + (\omega - v_0 q \cos \theta)^2 \left[\Delta + \frac{\rho_0^2}{\bar{\rho}^2} \zeta^2 \delta(\omega) \right]}{[\omega - c_+(\theta)q]^2 [\omega - c_-(\theta)q]^2 + \left\{ \omega [\Gamma_\rho(\mathbf{q}) + \Gamma_L(\mathbf{q})] - q_y [\gamma\Gamma_\rho(\mathbf{q}) + v_0\Gamma_L(\mathbf{q})] \right\}^2}. \quad (4.32)$$

Given these Fourier transformed correlation functions, we proceed further to obtain the spatially Fourier transformed equal-time correlation functions for the density and the velocity

fields. Neglecting the higher order fluctuations, we obtain the expressions for $C_{\rho\rho, vv}(\mathbf{q}, t)$ as given in Eqs. (4.9)-(4.10), where

$$\begin{aligned}
b(\theta) &= \cos^2 \theta \{ \gamma (D_\rho \sin^2 \theta + D_{\rho y} \cos^2 \theta) + v_0 (D_L \sin^2 \theta + D_y \cos^2 \theta) \}^2, \\
d(\theta) &= \gamma v_0 \cos^2 \theta - \sigma_1 \bar{\rho} \sin^2 \theta, \\
p_\pm(\theta) &= 2c_2 \{ c_\pm [(D_L + D_\rho) \sin^2 \theta + (D_y + D_{\rho y}) \cos^2 \theta] - \\
&\quad \cos \theta [(v_0 D_L + \gamma D_\rho) \sin^2 \theta + (v_0 D_y + \gamma D_{\rho y}) \cos^2 \theta] \}, \\
s_\pm(\theta) &= (c_\pm - v_0 \cos \theta)^2 / 2\pi, \\
s(\theta) &= \bar{\rho}^2 \sin^2 \theta / 2\pi, \\
a_\rho(\theta) &= \sin^2 \theta / 2\pi, \\
A_\rho(\theta) &= s(\theta) \left[\frac{1}{p_+(\theta)} + \frac{1}{p_-(\theta)} \right], \\
a_v(\theta) &= v_0^2 \cos^2 \theta / 2\pi \bar{\rho}^2, \\
A_v(\theta) &= \left[\frac{s_+(\theta)}{p_+(\theta)} + \frac{s_-(\theta)}{p_-(\theta)} \right].
\end{aligned}$$

POLAR FLOCK IN THE PRESENCE OF NON-QUENCHED INHOMOGENEITY

5.1 INTRODUCTION

We have shown in the last chapter that any amount of quenched randomness destroys the long range order (LRO) usually seen in the polar self-propelled particles (SPPs) in two dimensions (2D) [123, 124]. Here we introduce a Vicsek-like microscopic model for the polar SPPs in the presence of *non-quenched* inhomogeneity and adopt a dynamics so that both the SPPs and the inhomogeneity agents affect orientation of each other. We note that this model leads the system into a LRO state which is robust than that in the clean SPPs.

This chapter is organised as follows. In Sec. 5.2 we define the model, discuss about its different limits, and motivate the practical relevance of the model. The numerical details are provided in Sec. 5.3. In Sec. 5.3.1 we present results for the clean limit of our model which is simply the Vicsek model. We note the existence of quasi-long range order (QLRO) for the quenched inhomogeneity limit of our model, as presented in Sec. 5.3.2. The effect of non-quenched inhomogeneities is presented in Sec. 5.3.3. We note that for the non-quenched dynamics, the system attains a LRO state, and that LRO state survives upto noise strength greater than the critical noise strength for the order-disorder transition in the clean SPPs. This chapter is closed with concluding remarks in Sec. 5.4.

We consider a Vicsek-like model [31] for a collection of polar SPPs distributed over a 2D square substrate with periodic boundary condition. Each particle moves with a fixed speed v_s along their orientation $\theta \in [-\pi, \pi]$. The particles interact with their neighbours ‘ferromagnetically’ within a circle of radius $R_s = 1$; *i. e.*, all the neighbouring particles within the interaction range try to mutually align their orientation θ . However, the ambient noise perturbs mutual alignment of the SPPs. To introduce inhomogeneity in the system, we consider some immobile agents randomly distributed on the substrate. These inhomogeneity agents possess some intrinsic orientation ϕ , which may change depending on their interaction with the SPPs. These agents primarily act like obstacles, and try to align the orientation of the neighbouring SPPs (within a circle of radius $R_o = 1.0$) along their intrinsic orientations. Also the neighbouring SPPs affect the intrinsic orientation of the interacting obstacles. Therefore, the model follows the update rules

$$\mathbf{r}_j(t+1) = \mathbf{r}_j(t) + \mathbf{v}_j(t), \quad (5.1)$$

$$\theta_j(t+1) = \arg \left[\sum_{k \in R_s} e^{i\theta_k(t)} + \mu \sum_{k \in R_s} e^{i\phi_k(t)} \right] + \Delta\psi, \quad (5.2)$$

$$\phi_j(t+1) = \arg \left[e^{i\phi_j(t)} + \alpha \sum_{k \in R_o} e^{i\theta_k(t)} \right]. \quad (5.3)$$

Here $\mathbf{r}_j(t)$ and $\mathbf{v}_j(t) = v_s(\cos \theta_j(t), \sin \theta_j(t))$ respectively represent the position and the velocity of the j^{th} SPP at time t . The first term under summation on the right-hand-side (RHS) of Eq. (5.2) takes care of the SPP-SPP interaction, while the second term represents SPP-obstacle interaction tuned by a parameter μ . The ambient noise is represented by $\Delta\psi$ which can take any value randomly in the range $\eta[-\pi, \pi]$ for noise strength $\eta \in [0, 1]$. We assume $\Delta\psi$ an additive Gaussian white noise with delta correlation and zero mean. On the RHS of Eq. (5.3), the first term expresses inertia of the obstacle to retain its earlier orientation, while the second term takes care of the effect of SPP-obstacle interactions on the obstacle. In this equation, we consider another SPP-obstacle interaction strength α which is different from μ since the total linear momentum may not be conserved in this *dry active* system (see Sec. 1.2.2). This α

term makes the obstacles *non-quenched*, and for $\alpha = 0$ the model represents dynamics with *quenched* obstacles. We do not consider any explicit noise term to affect the ϕ update. The model defined by Eqs. (5.1)-(5.3) reduces to the celebrated Vicsek model (VM) [31] for the clean system.

The model described above is significantly different from the rotator-model described by Eqs. (4.1)-(4.2) in Chapter 4. There the obstacles are modeled as quenched rotators that add random angle over the mean orientation of all the SPPs within an interaction range. On the contrary, the effect of SPP-SPP and SPP-obstacle interactions are added ‘vectorially’ in the present model, and the direction of the ‘resultant vector’ gives the updated orientation in absence of the ambience noise. Therefore, in this model the obstacles are like ‘magnetic impurities’ and have different interaction strength as compared to the SPP-SPP interaction. The condition $\alpha \neq 0$ makes these obstacles or inhomogeneities non-quenched.

Let us consider a physical example to understand the relevance of the present model. Suppose there is a large mass gathering in a big hall, and we want to evacuate that place in a panic situation. We place some barriers randomly in the hall that can rotate about their body axes. The initial orientation of one barrier will affect a chunk of people close to it. In turn, the barrier will also reorient itself because of the pressure (push) exerted by those people. In the following sections, we show that the above model provides us an efficient way of ‘crowd controlling’.

5.3 NUMERICAL STUDY

We consider a collection of N_s polar SPPs spread over a $L \times L$ square substrate with periodic boundary condition. Density of the SPPs is defined as $c_s = N_s/L^2$. Similarly the density of the obstacles (inhomogeneity) is $c_o = N_o/L^2$ where the substrate has N_o obstacles uniformly distributed on the substrate. We consider $v_s = 1.0$, $R_s = R_o = 1$ for simplicity. Initially the orientation θ of the SPPs are chosen randomly in the range $[-\pi, \pi]$. Also, the obstacle orientations $\phi \in [-\pi, \pi]$ are chosen randomly at the beginning. The position and the orientation of the SPPs, and the orientation of the obstacles are updated following the update rules given by Eqs. (5.1)-(5.3). We thermalise the system for 3×10^5 iterations to achieve steady-state, and

calculate the required macroscopic variables by averaging over next 5×10^5 iterations. We also use many realisations for better averaging. During each iteration, all the microscopic variables of the SPPs and the obstacles are updated simultaneously using OpenMP Application Programme Interface. The ordering of the SPPs is characterised by the scalar value of the average normalised velocity $V = \langle \frac{1}{N_s v_s} | \sum_{j=1}^{N_s} \mathbf{v}_j | \rangle$.

5.3.1 Clean system

We first study the clean system, *i. e.*, the VM in the steady-state. The system shows monotonous order-disorder transition with noise strength as shown in Fig. 5.1 for $c_o = 0$. The system remains highly clustered and highly ordered for low η values. The ordering decreases and the system gets more homogeneous with increasing η . For moderately high η , bands appear in the system and ordering decreases further. The system gets completely disordered for further increment in noise. The real space snapshot of the clean system for different η values are shown in the top panel of Fig. 5.2. Note that in the clean system, the parameters μ and α have no relevance.

5.3.2 SPPs with quenched inhomogeneity

The effect of quenched obstacles (*i. e.*, $\alpha = 0$) on the SPPs are discussed in this section. As shown in Figs. 5.1(a)-(b), the system with quenched inhomogeneities attains the maximum order at a finite noise strength. This phenomenon of optimal ordering is clear from the snapshots shown in the second panel from the top of Fig. 5.2, and has already been discussed in Sec. 4.5. We note that for the above mentioned values of the microscopic parameters, the optimal η is very small for small μ . Therefore, we choose a moderate value $\mu = 200$ for further studies. We note that V decreases algebraically with N_s following Eq. (4.4) in the presence of quenched inhomogeneities, as shown in Fig. 5.3(a). Moreover, the orientation distribution $P(\theta)$ (see Sec. 4.3.1 for definition) broadens with system size, as shown in Fig. 5.4(a). These results provide further confirmation for the presence of QLRO in the presence of quenched inhomogeneities in 2D collection of SPPs.

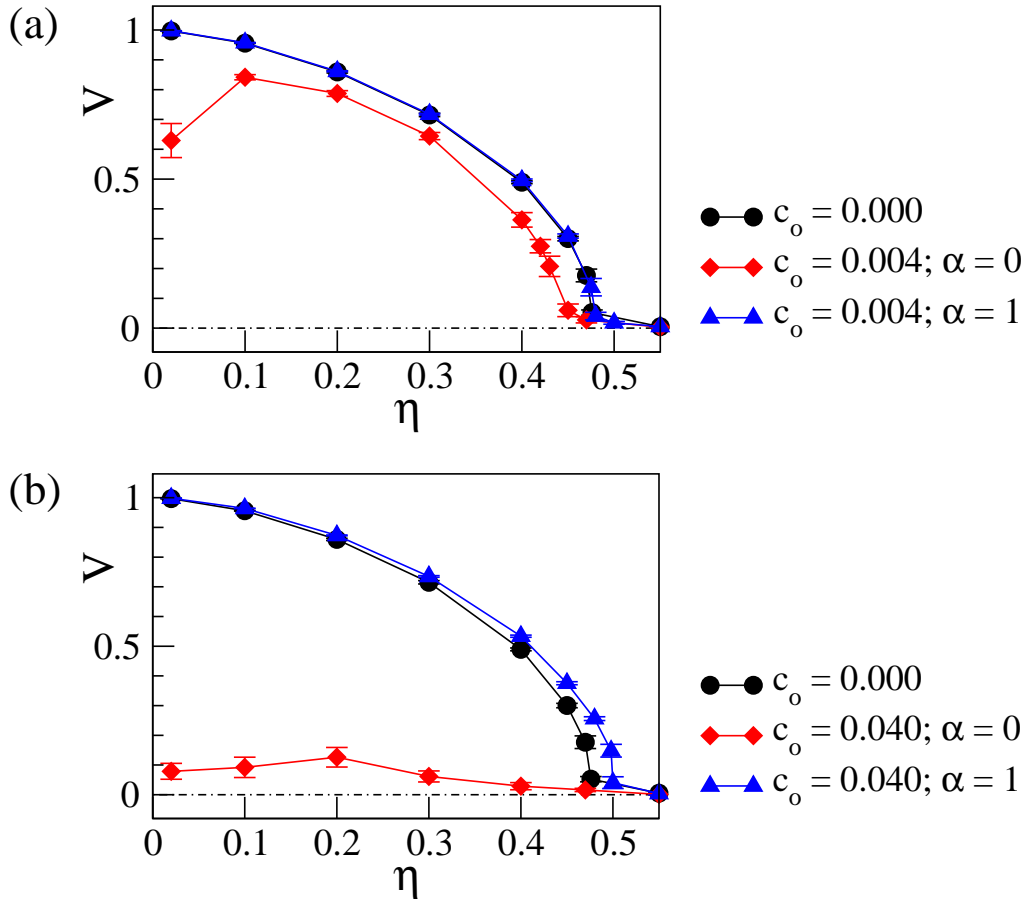


Figure 5.1: Order-disorder transition with noise strength shown for $L = 200$. The clean system shows monotonous transition. The same curve has been drawn in (a) and (b) for the clean system. In the presence of obstacles, (a) and (b) are drawn for $c_o = 0.004$ and 0.040 , respectively. If the obstacles are quenched in nature ($\alpha = 0$), optimal ordering is attained at finite $\eta > 0$. For non-quenched obstacles ($\alpha = 1$), the system shows monotonous transition. Also, for non-quenched obstacles the transition takes place at higher η as compared to the clean system.

5.3.3 SPPs with non-quenched inhomogeneity

Now we set $\alpha > 0$; therefore, the inhomogeneities become non-quenched. We note that any value of $\alpha > 0$ ultimately leads the system to the same steady-state, and α only changes the time required to attain the steady-state. Although it will be interesting to look for the evolution rates depending on α , it is beyond the scope of the current work. In this chapter, we consider $\alpha = 1$ and study the corresponding steady-states only.

We note that because of the mutual alignment interaction between the SPPs and the obstacles, the obstacles get aligned with the SPPs for favourable η . Once the obstacles get aligned,

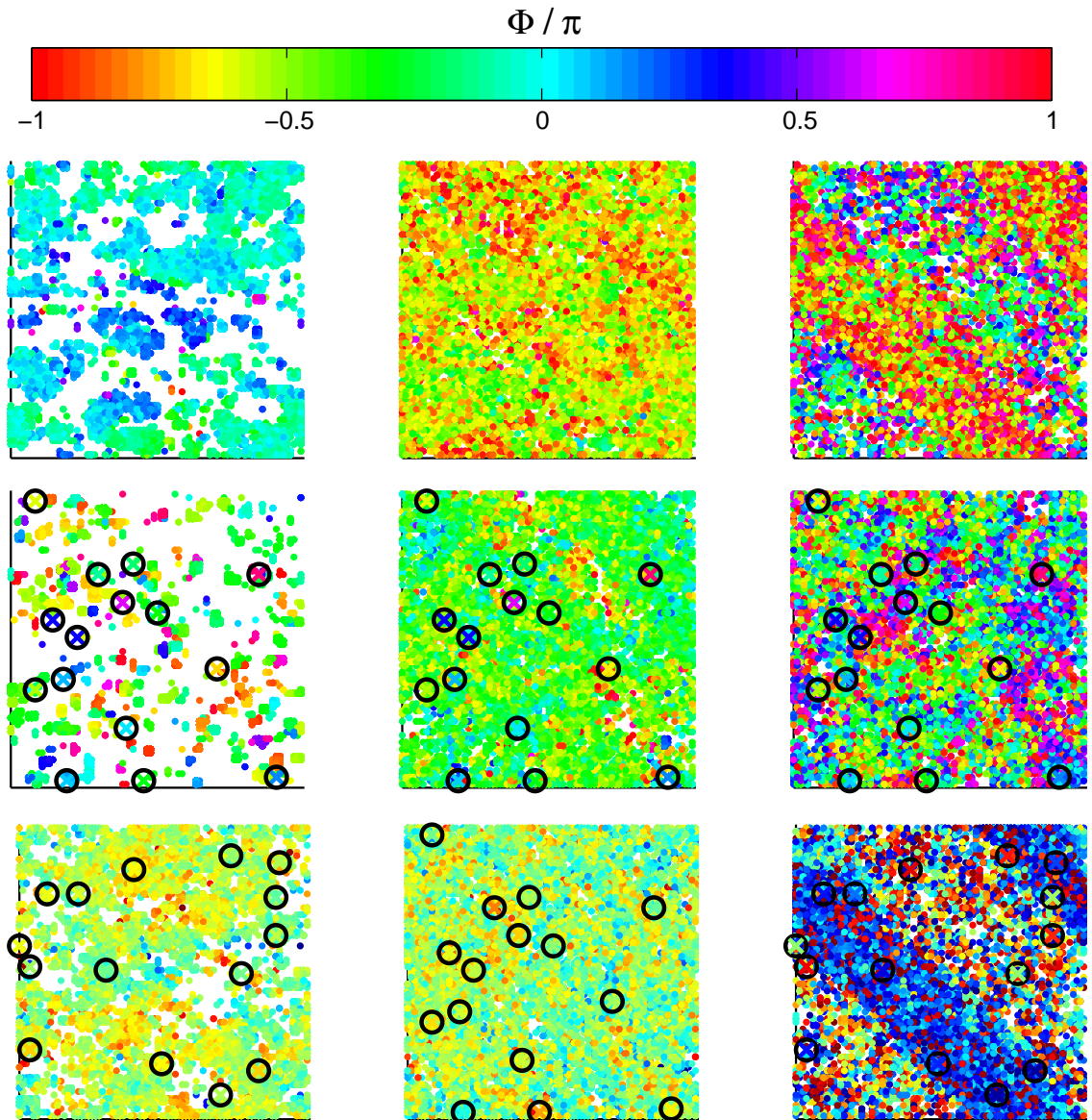


Figure 5.2: Real space snapshot. The colour bar indicates orientation $\Phi \equiv \theta$ (respectively ϕ) of the SPPs (obstacles). The obstacles are represented by \otimes symbols, and the colour of \times in \otimes indicates ϕ . From left to right, the panels correspond to $\eta = 0.01, 0.20$ and 0.40 respectively. (Top panel) is drawn for the clean system ($c_0 = 0$). The ordering decreases monotonously with η for the clean system. Band appears in the right most panel. (Second panel from the top) is drawn for $c_0 = 0.006$ with quenched obstacles, *i. e.*, $\alpha = 0$. In this case the system is disordered at low noise, gets ordered at moderate noise, and again gets disordered at high noise (band is destroyed at $\eta = 0.40$). (Bottom panel) is drawn for $c_0 = 0.006$ with non-quenched obstacles ($\alpha = 1$). In this case, the system shows monotonous order-disorder transition like the clean system. Again band appears for $\eta = 0.40$. All obstacles are not shown for the sake of the clarity of the figures.

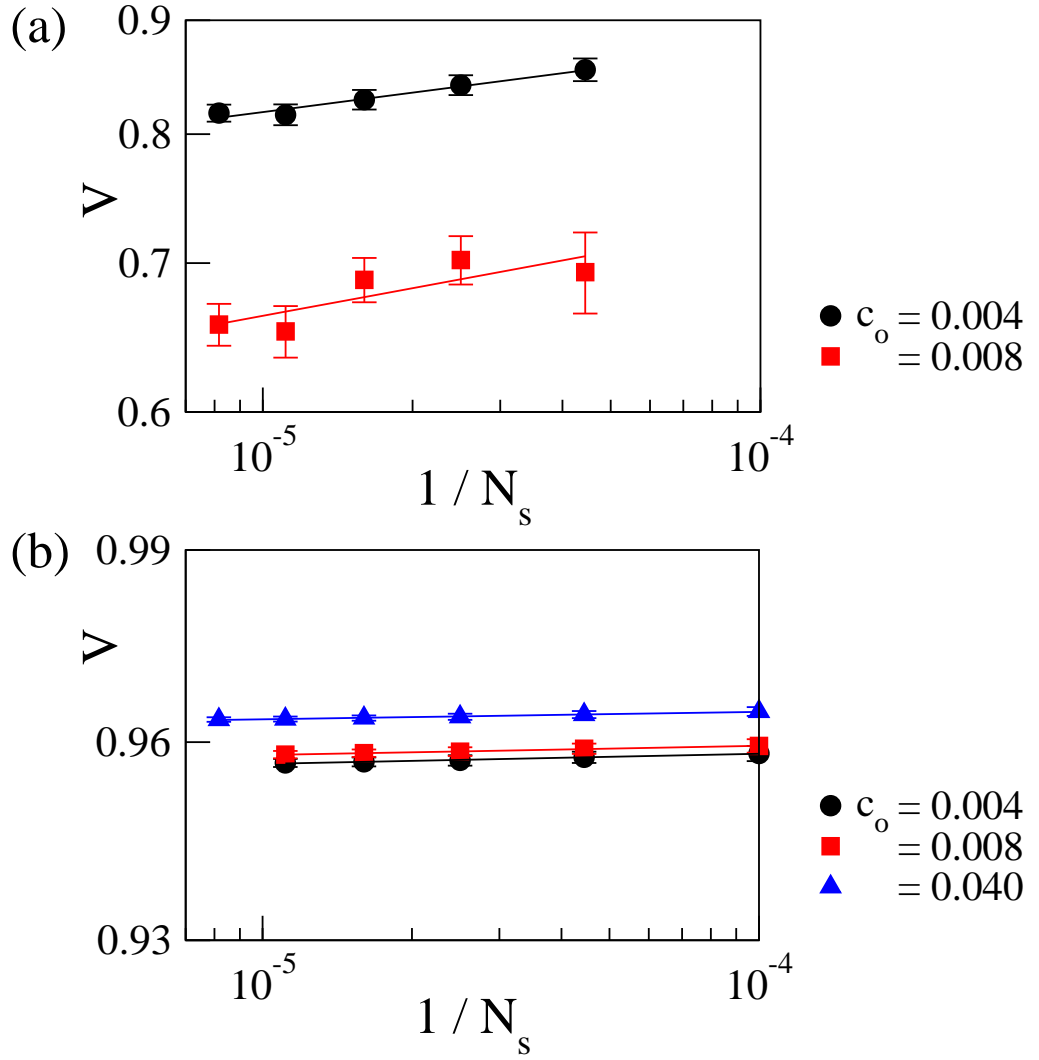


Figure 5.3: V versus $1/N_s$ plot on log-log scale for $\eta = 0.10$. (a) In the presence of quenched obstacles, *i. e.*, for $\alpha = 0$, V decreases algebraically with N_s . The solid lines show respective fits. (b) For $\alpha = 1$ and $c_o > 1$, V shows almost no change with N_s . The solid lines show algebraic fits with exponent $\nu < 10^{-3}$.

they make the neighbouring SPPs more aligned; therefore, the obstacles turn into aligners, and thereby we call these inhomogeneity agents ‘obstacle-turned-aligners’ (OTAs). In the presence of these OTAs, the system shows monotonous order-disorder transition with η , as shown in Fig. 5.1. Therefore, the presence of OTAs suppress the phenomenon of optimal ordering at finite noise which has earlier been seen in the presence of quenched inhomogeneities. Similar to the clean system, the system with OTAs show clustered and highly ordered state at low noise. For moderate noise, the system is homogeneous and moderately ordered. For further increase in noise, bands appear in the system, and the system become

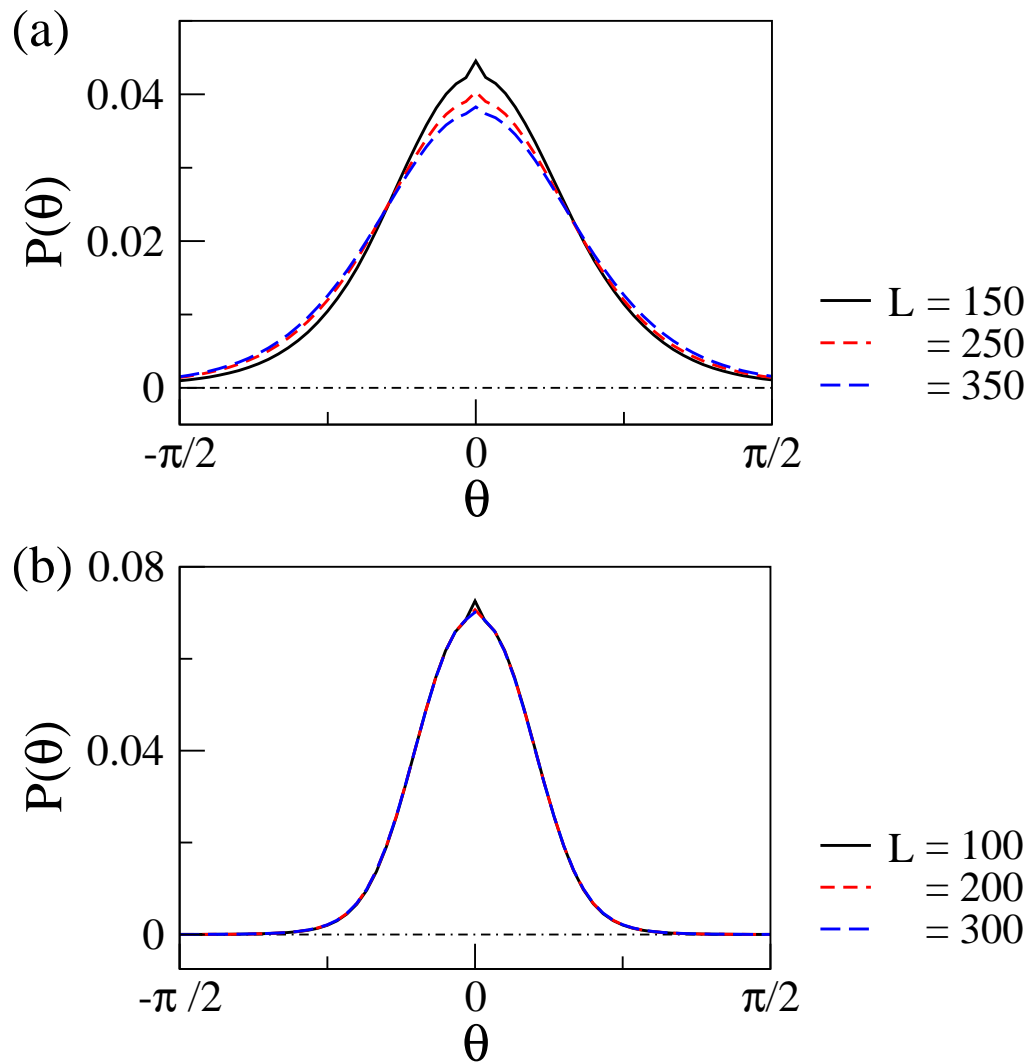


Figure 5.4: Steady-state orientation distribution of the SPPs shown for $\eta = 0.10$ and $c_o = 0.004$. (a) Width of $P(\theta)$ increases with system size in the presence of quenched obstacles. (b) For non-quenched obstacles $P(\theta)$ does not depend on system size. θ axis has been zoomed into the range $[-\pi/2, \pi/2]$ for better visibility.

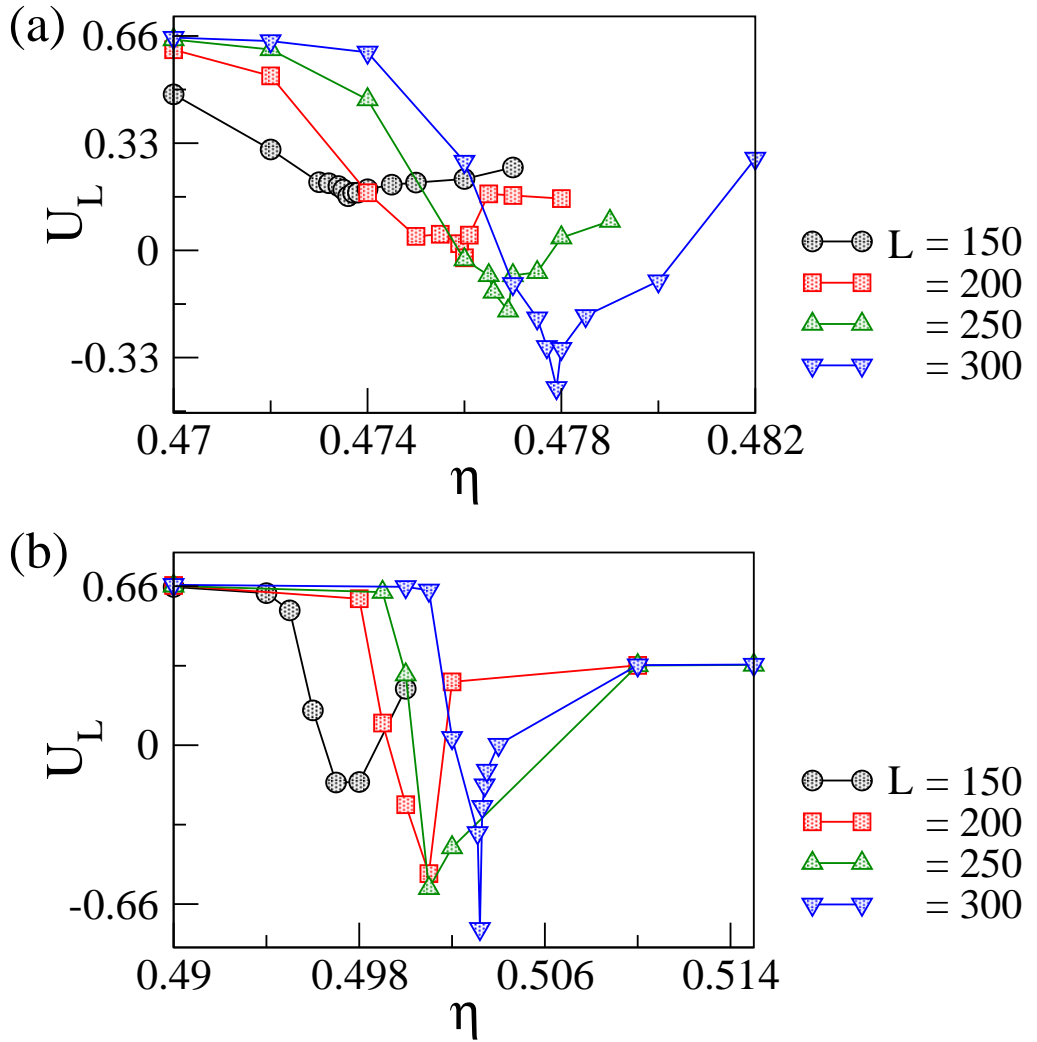


Figure 5.5: (a) and (b) show Binder cumulant for $c_0 = 0$ and 0.04, respectively. (b) is shown for $\alpha = 1$. The transition noise η_c is given by the deepest U_L for the corresponding system size L .

disordered beyond a critical noise η_c . These phenomena are clear from the snapshots shown in the bottom panel of Fig. 5.2.

Next we study the variation of V with system size for different η and c_0 in the ordered steady-state. As shown in Fig. 5.3(b) for $\eta = 0.10$, V does not change with system size. We also note that $P(\theta)$ is independent of the system size in the presence of the OTAs, as shown in Fig. 5.4(b). Therefore, the modification of the quenched inhomogeneities through the dynamics described by Eq. (5.3) again establishes the LRO in the polar SPPs.

In the presence of OTAs, the SPPs become more robust to the ambient noise as compared to the clean SPPs. Fig. 5.1(b) shows that the critical noise η_c associated with the order-

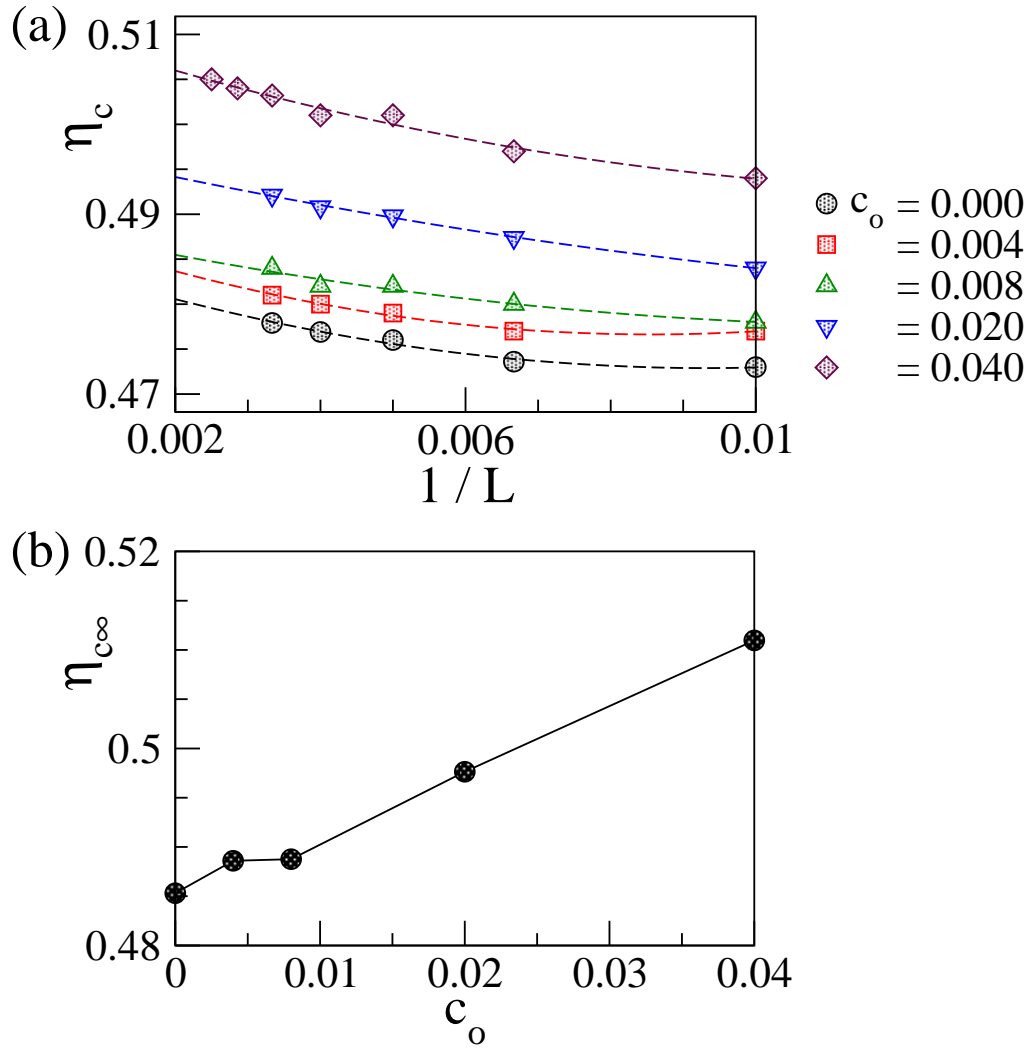


Figure 5.6: (a) shows finite size scaling of η_c for different c_o . The dashed lines are the respective quadratic fits. Intercept on η_c -axis gives thermodynamic value of the critical noise strength ($\eta_{c\infty}$). (b) In the presence of the OTAs, $\eta_{c\infty}$ increases monotonously with c_o .

disorder transition increases in the presence of OTAs. To study this phenomenon in detail, we calculate η_c for different c_o and L using Binder cumulant defined as

$$U_L = 1 - \frac{\langle V_{inst}^4 \rangle}{3\langle V_{inst}^2 \rangle^2}, \quad (5.4)$$

where V_{inst} represents instantaneous absolute value of the average normalised velocity, and $\langle \cdot \rangle$ represents averaging over simulation time and many realisations. Plots of U_L vs. η are shown for different system sizes for $c_o = 0$ and 0.04 in Figs. 5.5(a) and (b), respectively. We assume that the minimum value of U_L indicates the respective η_c . In Fig. 5.6(a), we show the

variation in η_c with the system size for different c_o . These data show quadratic fit with $1/L$. Interpolating those fits, we obtain the values of the critical noise in the thermodynamic limit $\eta_{c\infty} = \eta_c(L \rightarrow \infty)$. As shown in Fig. 5.6(b), $\eta_{c\infty}$ increases monotonously with c_o . Since the mean separation between neighbouring OTAs decreases with increasing c_o , the OTAs offer more stability to the bands of SPPs. Therefore, the ordered state of the SPPs become more robust to noise for high density of the OTAs .

5.4 DISCUSSION

In summary, we have studied the effect of *non-quenched* inhomogeneities on the polar SPPs in 2D. The dynamics of the system is such that both the SPPs and the inhomogeneity agents feedback orientation of each other. We show that this dynamics again establishes the long range order in the SPPs which is destroyed in the presence of the quenched randomness. Moreover, these non-quenched inhomogeneities make the ordering in the polar SPPs robust than the clean system. We anticipate that this understanding can be used to control crowd, or in other polar self-propelled systems where we need better ordering and robustness.

We have not discussed the hydrodynamics of the numerical model introduced above, since we are yet to draw some conclusion from that. We have calculated auto-correlation of the non-quenched inhomogeneities, which suggests that these non-quenched inhomogeneities *cannot* be considered as pure annealed randomness. We realise that a complicated interplay of the ambience noise, the density of the inhomogeneity and the parameter α controls the eigenfrequencies of the corresponding sound modes. These inhomogeneities may act like pure quenched or annealed obstacles depending on the values of the microscopic parameters, which we shall discuss somewhere else.

CONCLUSION

In this chapter, we provide a brief summary and concluding remarks on all the problems discussed so far. We have introduced a lattice model for the active nematic in two dimensions (2D) consisting of apolar SPPs. The dynamics of the apolar SPPs is anisotropic since it moves towards the axis, horizontal or vertical, with which it makes the least angle. This active model reduces to its equilibrium counterpart if the anisotropic dynamics is ceased and the particles are allowed to diffuse towards any axes. We have incorporated volume exclusion interaction in both the models, active or equilibrium. Furthermore, the particles interact nematically with their neighbours. We note that the equilibrium model shows a simple isotropic disorder to nematic state transition with the change in temperature or particle density. On the contrary, the phase diagram of the active model in temperature-density plane is a complicated and interesting one. We see that the system remains disordered at high temperature and low density regime. With the increase in density, some highly ordered domains with high local density emerges in the background of a low local density disordered regime. Hence, the active system is said to be in an inhomogeneous mixed state. The system shows bistability between a homogeneous globally ordered state and the inhomogeneous mixed state at high density regime. This bistability appears because of the volume exclusion interaction in the model, since at the complete filling limit there is no space to move for the active particles. Therefore, the active model reduces to the equilibrium model. We also see that at low temperature regime, the transition from the disorder state to the inhomogeneous mixed state takes place through band formation. This observation has further been justified by our linearised study of the corresponding hydrodynamics. It will be interesting to employ

this model of active and equilibrium nematic in three spatial dimensions for a comparative study. In the current model the particles have the same chances to move either of the two sides of a selected axis. Adaptation of an asymmetric simple exclusion process [128] may invoke further interesting properties in the active model.

The phase ordering kinetics of the hydrodynamic fields of the 2D polar SPPs are discussed in Chapter 3. We note that in the clean system, the polarisation field grows algebraically with time and shows dynamical scaling. However, we do not find any clean growth law for the density field, and it follows an approximate power-law growth. The density field does not show dynamical scaling; therefore, the dynamics of this field is not dominated by a single energy scale. We introduce quenched inhomogeneity in the system by a random field, and thereby we call it a random field active model analogous to the celebrated random field Ising model. The growth dynamics slows down for both the fields in presence of the quenched inhomogeneity. We note that though initially the polarisation field follows a disorder-dependent algebraic growth law, at late times the growth is logarithmic and the corresponding exponent does not depend on the strength of inhomogeneity. An analogous study of the phase ordering kinetics in the polar SPPs in the presence of random bonds would be interesting.

The next problem we addressed is the steady-state behaviour of the 2D polar SPPs in presence of quenched inhomogeneities. We introduce a Vicsek-like model for the polar SPPs, and the inhomogeneities are modeled as quenched rotators, similar to the vortices appearing in rivers. Our numerical study shows that a small density of the rotators is sufficient to destroy the usual long-range order of the polar SPPs in clean environment. The system goes continuously to the disorder state with increasing density of the rotators. We also do a linearised study of the corresponding hydrodynamic equations of motion. Our calculation shows that the structure factors of the hydrodynamic fields contain an extra $1/q^2$ divergence in the small wave-number limit in the presence of quenched inhomogeneities, and this divergence possesses strong directional anisotropy. We argue that this extra divergence destroys the usual long range order of the clean SPPs. There may be question regarding the importance of the non-linearities in the equations, however, recently Toner *et al.* categorically answer this query in their preprints [123, 124]. Note that in the equilibrium limit, our model is analogous to the

XY model. It is now well known that in presence of quenched inhomogeneity, there cannot be any long range order below four dimensions. Similar to this, we claim that quenched inhomogeneity destroy the long range order in the polar SPPs in 2D.

The destruction of the long-range order in the 2D polar SPPs in presence of the quenched inhomogeneities motivates us to search for the tuning mechanism that can again establish the long range order in presence of some inhomogeneity. To do so, we introduce a Vicsek-like model for inhomogeneous system where the orientation of the SPPs and the inhomogeneities depend on each other. We show that such a dynamics not only establishes the long range order in the system, but that new long range order state is robust as compared to the clean SPPs. In this thesis we have only presented the order-disorder transition in the model, however this model possess interesting growth dynamics which we shall discuss somewhere else.

BIBLIOGRAPHY

- ¹M. C. Marchetti, J. F. Joanny, S. Ramaswamy, T. B. Liverpool, J. Prost, M. Rao, and R. A. Simha, “Hydrodynamics of soft active matter,” *Review of Modern Physics* **85**, 1143–1189 (2013) (cit. on pp. 1, 6, 7, 11, 13, 19, 20).
- ²J. Toner, Y. Tu, and S. Ramaswamy, “Hydrodynamics and phases of flocks,” *Annals of Physics* **318**, Special Issue, 170–244 (2005) (cit. on pp. 1, 6, 12, 25, 52).
- ³S. Ramaswamy, “The mechanics and statistics of active matter,” *Annual Review of Condensed Matter Physics* **1**, 323–345 (2010) (cit. on pp. 1, 6, 11, 13, 19, 20).
- ⁴T. Vicsek and A. Zafeiris, “Collective motion,” *Physics Reports* **517**, Collective motion, 71–140 (2012) (cit. on pp. 1, 6).
- ⁵M. E. Cates, “Diffusive transport without detailed balance in motile bacteria: does microbiology need statistical physics?” *Reports on Progress in Physics* **75**, 042601 (2012) (cit. on pp. 1, 6).
- ⁶C. A. Yates, R. Baker, R. Erban, and P. Maini, “Refining self-propelled particle models for collective behaviour,” *Canadian Applied Maths Quarterly* **18** (2011) (cit. on pp. 1, 6).
- ⁷S. Ramaswamy, “Active matter,” *Journal of Statistical Mechanics: Theory and Experiment* **2017**, 054002 (2017) (cit. on pp. 1, 6, 7).
- ⁸M. E. Cates and J. Tailleur, “Motility-induced phase separation,” *Annual Review of Condensed Matter Physics* **6**, 219–244 (2015) (cit. on p. 1).
- ⁹A. Bricard, J.-B. Caussin, N. Desreumaux, O. Dauchot, and D. Bartolo, “Emergence of macroscopic directed motion in populations of motile colloids,” *Nature* **503**, 95 EP – (2013) (cit. on pp. 1, 8, 17).
- ¹⁰I. Theurkauff, C. Cottin-Bizonne, J. Palacci, C. Ybert, and L. Bocquet, “Dynamic clustering in active colloidal suspensions with chemical signaling,” *Physical Review Letters* **108**, 268303 (2012) (cit. on p. 1).

- ¹¹J. Deseigne, O. Dauchot, and H. Chaté, “Collective motion of vibrated polar disks,” *Physical Review Letters* **105**, 098001 (2010) (cit. on pp. 1, 8, 16).
- ¹²V. Narayan, N. Menon, and S. Ramaswamy, “Nonequilibrium steady states in a vibrated-rod monolayer: tetratic, nematic, and smectic correlations,” *Journal of Statistical Mechanics: Theory and Experiment* **1**, 01005 (2006), eprint: [cond-mat/0510082](https://arxiv.org/abs/cond-mat/0510082) (cit. on pp. 1, 8, 21, 32).
- ¹³V. Narayan, S. Ramaswamy, and N. Menon, “Long-lived giant number fluctuations in a swarming granular nematic,” *Science* **317**, 105–108 (2007) (cit. on pp. 1, 8, 21, 32).
- ¹⁴D. L. Blair, T. Neicu, and A. Kudrolli, “Vortices in vibrated granular rods,” *Physical Review E* **67**, 031303 (2003) (cit. on pp. 1, 8, 16, 21).
- ¹⁵N. Kumar, H. Soni, S. Ramaswamy, and A. K. Sood, “Flocking at a distance in active granular matter,” *Nature Communications* **5**, Article, 4688 EP – (2014) (cit. on pp. 1, 8, 16, 17).
- ¹⁶W. F. Paxton, K. C. Kistler, C. C. Olmeda, A. Sen, S. K. St. Angelo, Y. Cao, T. E. Mallouk, P. E. Lammert, and V. H. Crespi, “Catalytic nanomotors: autonomous movement of striped nanorods,” *Journal of the American Chemical Society* **126**, 13424–13431 (2004) (cit. on pp. 1, 16).
- ¹⁷M. W. Zemansky, *Heat and thermodynamics; an intermediate textbook [by] mark w. zemansky*, English, 5th ed. (McGraw-Hill New York, 1968), xx, 658 p. (Cit. on pp. 2, 3).
- ¹⁸R. K. Pathria, *Statistical mechanics / r.k. pathria*, English, 2nd ed. (Butterworth-Heinemann Oxford ; Boston, 1996), xiv, 529 p. : (cit. on pp. 2, 3, 26).
- ¹⁹K. Huang, *Statistical mechanics*, 2nd ed. (John Wiley & Sons, 1987) (cit. on pp. 2, 3, 26).
- ²⁰P. M. Chaikin and T. C. Lubensky, *Principles of condensed matter physics* (Cambridge University Press, 1995) (cit. on pp. 3, 4, 8, 11, 12, 14, 17–19, 21, 24, 26, 27, 33, 50, 69, 79).
- ²¹V. Balakrishnan, *Elements of nonequilibrium statistical mechanics*, English (CRC Press, 2008), p. 314 (cit. on pp. 3, 4).
- ²²D. P. Landau and K. Binder, *A Guide to Monte Carlo Simulations in Statistical Physics - 2nd Edition* (Sept. 2005), p. 448 (cit. on pp. 3, 31, 32).

- ²³G. Szamel, “Self-propelled particle in an external potential: existence of an effective temperature,” *Physical Review E* **90**, 012111 (2014) (cit. on p. 4).
- ²⁴D. Loi, S. Mossa, and L. F. Cugliandolo, “Effective temperature of active matter,” *Physical Review E* **77**, 051111 (2008) (cit. on p. 4).
- ²⁵T. Speck, J. Bialké, A. M. Menzel, and H. Löwen, “Effective cahn-hilliard equation for the phase separation of active brownian particles,” *Physical Review Letters* **112**, 218304 (2014) (cit. on p. 4).
- ²⁶J. Tailleur and M. E. Cates, “Statistical mechanics of interacting run-and-tumble bacteria,” *Physical Review Letters* **100**, 218103 (2008) (cit. on p. 4).
- ²⁷T. Speck, “Stochastic thermodynamics for active matter,” *Europhysics Letters* **114**, 30006 (2016) (cit. on p. 4).
- ²⁸E. Fodor, C. Nardini, M. E. Cates, J. Tailleur, P. Visco, and F. van Wijland, “How far from equilibrium is active matter?” *Physical Review Letters* **117**, 038103 (2016) (cit. on p. 4).
- ²⁹J. Toner and Y. Tu, “Flocks, herds, and schools: a quantitative theory of flocking,” *Physical Review E* **58**, 4828–4858 (1998) (cit. on pp. 4, 7, 10–14, 19, 55, 72, 79–81).
- ³⁰X.-q. Shi and Y.-q. Ma, “Topological structure dynamics revealing collective evolution in active nematics,” *Nature Communications* **4**, Article, 3013 EP – (2013) (cit. on pp. 7, 21, 29, 46).
- ³¹T. Vicsek, A. Czirók, E. Ben-Jacob, I. Cohen, and O. Shochet, “Novel type of phase transition in a system of self-driven particles,” *Physical Review Letters* **75**, 1226–1229 (1995) (cit. on pp. 7–9, 14, 16, 25, 69, 71, 72, 89, 90).
- ³²G. Grégoire and H. Chaté, “Onset of collective and cohesive motion,” *Physical Review Letters* **92**, 025702 (2004) (cit. on pp. 7, 9, 10, 13, 14, 16, 25).
- ³³S. Mishra and S. Ramaswamy, “Active nematics are intrinsically phase separated,” *Physical Review Letters* **97**, 090602 (2006) (cit. on pp. 7, 20, 25).
- ³⁴S. Ngo, A. Peshkov, I. S. Aranson, E. Bertin, F. Ginelli, and H. Chaté, “Large-scale chaos and fluctuations in active nematics,” *Physical Review Letters* **113**, 038302 (2014) (cit. on pp. 7, 14, 29, 32, 47).

- ³⁵A. P. Solon and J. Tailleur, “Flocking with discrete symmetry: the two-dimensional active ising model,” *Physical Review E* **92**, 042119 (2015) (cit. on pp. 7, 14, 29, 32, 47).
- ³⁶S. Ramaswamy, R. A. Simha, and J. Toner, “Active nematics on a substrate: giant number fluctuations and long-time tails,” *Europhysics Letters* **62**, 196 (2003) (cit. on pp. 7, 14, 18–21, 29, 32, 43).
- ³⁷E. Bertin, H. Chaté, F. Ginelli, S. Mishra, A. Peshkov, and S. Ramaswamy, “Mesoscopic theory for fluctuating active nematics,” *New Journal of Physics* **15**, 085032 (2013) (cit. on pp. 7, 20, 29, 32, 43).
- ³⁸T. Ihle, “Kinetic theory of flocking: derivation of hydrodynamic equations,” *Physical Review E* **83**, 030901 (2011) (cit. on pp. 7, 10, 14).
- ³⁹S. Mishra, A. Baskaran, and M. C. Marchetti, “Fluctuations and pattern formation in self-propelled particles,” *Physical Review E* **81**, 061916 (2010) (cit. on pp. 7, 13, 25, 52, 56).
- ⁴⁰J. Buhl, D. J. T. Sumpter, I. D. Couzin, J. J. Hale, E. Despland, E. R. Miller, and S. J. Simpson, “From disorder to order in marching locusts,” *Science* **312**, 1402–1406 (2006), eprint: <http://science.sciencemag.org/content/312/5778/1402.full.pdf> (cit. on p. 8).
- ⁴¹R. Kemkemer, D. Kling, D. Kaufmann, and H. Gruler, “Elastic properties of nematoid arrangements formed by amoeboid cells,” *European Physical Journal E* **1** (2000) epje/v1/p215(e9284) (cit. on pp. 8, 21, 32).
- ⁴²Gruler, H., Dewald, U., and Eberhardt, M., “Nematic liquid crystals formed by living amoeboid cells *,” *European Physical Journal B* **11**, 187–192 (1999) (cit. on pp. 8, 21).
- ⁴³J. W. Jolles, N. J. Boogert, V. H. Sridhar, I. D. Couzin, and A. Manica, “Consistent individual differences drive collective behavior and group functioning of schooling fish,” *Current Biology* **27**, 2862–2868.e7 (2017) (cit. on pp. 8, 82).
- ⁴⁴O. Feinerman, I. Pinkoviezky, A. Gelblum, E. Fonio, and N. S. Gov, “The physics of cooperative transport in groups of ants,” *Nature Physics* (2018) 10.1038/s41567-018-0107-y (cit. on p. 8).
- ⁴⁵H. Chaté, F. Ginelli, and G. Grégoire, “Comment on “phase transitions in systems of self-propelled agents and related network models”,,” *Physical Review Letters* **99**, 229601 (2007) (cit. on pp. 9, 10).

- ⁴⁶H. Chaté, F. Ginelli, G. Grégoire, and F. Raynaud, “Collective motion of self-propelled particles interacting without cohesion,” *Physical Review E* **77**, 046113 (2008) (cit. on pp. 9, 10, 13, 14, 25, 52, 59).
- ⁴⁷M. Nagy, I. Daruka, and T. Vicsek, “New aspects of the continuous phase transition in the scalar noise model (snm) of collective motion,” *Physica A: Statistical Mechanics and its Applications* **373**, 445–454 (2007) (cit. on p. 9).
- ⁴⁸M. Aldana, V. Dossetti, C. Huepe, V. M. Kenkre, and H. Larralde, “Phase transitions in systems of self-propelled agents and related network models,” *Physical Review Letters* **98**, 095702 (2007) (cit. on p. 9).
- ⁴⁹J. Toner and Y. Tu, “Long-range order in a two-dimensional dynamical XY model: how birds fly together,” *Physical Review Letters* **75**, 4326–4329 (1995) (cit. on pp. 10–14, 79).
- ⁵⁰E. Bertin, M. Droz, and G. Grégoire, “Boltzmann and hydrodynamic description for self-propelled particles,” *Physical Review E* **74**, 022101 (2006) (cit. on pp. 10, 14).
- ⁵¹E. Bertin, M. Droz, and G. Grégoire, “Hydrodynamic equations for self-propelled particles: microscopic derivation and stability analysis,” *Journal of Physics A: Mathematical and Theoretical* **42**, 445001 (2009) (cit. on pp. 10, 13, 14).
- ⁵²R. Simha and S. Ramaswamy, “Statistical hydrodynamics of ordered suspensions of self-propelled particles: waves, giant number fluctuations and instabilities,” *Physica A: Statistical Mechanics and its Applications* **306**, Invited Papers from the 21th IUPAP International Conference on Statistical Physics, 262–269 (2002) (cit. on pp. 14, 18).
- ⁵³N. D. Mermin and H. Wagner, “Absence of ferromagnetism or antiferromagnetism in one- or two-dimensional isotropic heisenberg models,” *Physical Review Letters* **17**, 1133–1136 (1966) (cit. on p. 14).
- ⁵⁴V. Schaller, C. Weber, C. Semmrich, E. Frey, and A. R. Bausch, “Polar patterns of driven filaments,” *Nature* **467**, 73–77 (2010) (cit. on p. 15).
- ⁵⁵V. Schaller, C. Weber, E. Frey, and A. R. Bausch, “Polar pattern formation: hydrodynamic coupling of driven filaments,” *Soft Matter* **7**, 3213–3218 (2011) (cit. on p. 15).

- ⁵⁶B. Szabó, G. J. Szöllösi, B. Gönci, Z. Jurányi, D. Selmeczi, and T. Vicsek, “Phase transition in the collective migration of tissue cells: experiment and model,” *Physical Review E* **74**, 061908 (2006) (cit. on p. 15).
- ⁵⁷D. Yamada, T. Hondou, and M. Sano, “Coherent dynamics of an asymmetric particle in a vertically vibrating bed,” *Physical Review E* **67**, 040301 (2003) (cit. on p. 16).
- ⁵⁸A. Kudrolli, G. Lumay, D. Volfson, and L. S. Tsimring, “Swarming and swirling in self-propelled polar granular rods,” *Physical Review Letters* **100**, 058001 (2008) (cit. on p. 16).
- ⁵⁹C. A. Weber, T. Hanke, J. Deseigne, S. Léonard, O. Dauchot, E. Frey, and H. Chaté, “Long-range ordering of vibrated polar disks,” *Physical Review Letters* **110**, 208001 (2013) (cit. on p. 16).
- ⁶⁰P. G. de Gennes, *The physics of liquid crystals, by p. g. de gennes*, English (Clarendon Press Oxford [Eng.], 1974), xi, 333 p. (Cit. on pp. 17, 21, 33).
- ⁶¹H. Chaté, F. Ginelli, and R. Montagne, “Simple model for active nematics: quasi-long-range order and giant fluctuations,” *Physical Review Letters* **96**, 180602 (2006) (cit. on pp. 17, 18, 25, 29).
- ⁶²X.-q. Shi and Y.-q. Ma, “Deterministic endless collective evolution in active nematics,” ArXiv e-prints (2010), [arXiv:1011.5408 \[cond-mat.stat-mech\]](https://arxiv.org/abs/1011.5408) (cit. on pp. 20, 29).
- ⁶³F. Ginelli, F. Peruani, M. Bär, and H. Chaté, “Large-scale collective properties of self-propelled rods,” *Physical Review Letters* **104**, 184502 (2010) (cit. on pp. 21, 25).
- ⁶⁴A. Peshkov, I. S. Aranson, E. Bertin, H. Chaté, and F. Ginelli, “Nonlinear field equations for aligning self-propelled rods,” *Physical Review Letters* **109**, 268701 (2012) (cit. on p. 21).
- ⁶⁵S. Ngo, F. Ginelli, and H. Chaté, “Competing ferromagnetic and nematic alignment in self-propelled polar particles,” *Physical Review E* **86**, 050101 (2012) (cit. on p. 21).
- ⁶⁶T. Sanchez, D. T. N. Chen, S. J. DeCamp, M. Heymann, and Z. Dogic, “Spontaneous motion in hierarchically assembled active matter,” *Nature* **491**, 431 EP – (2012) (cit. on p. 21).
- ⁶⁷Y. Sumino, K. H. Nagai, Y. Shitaka, D. Tanaka, K. Yoshikawa, H. Chaté, and K. Oiwa, “Large-scale vortex lattice emerging from collectively moving microtubules,” *Nature* **483**, 448–452 (2012) (cit. on p. 21).

- ⁶⁸S. J. DeCamp, G. S. Redner, A. Baskaran, M. F. Hagan, and Z. Dogic, “Orientational order of motile defects in active nematics,” *Nature Materials* **14**, 1110 EP – (2015) (cit. on pp. 21, 29, 46).
- ⁶⁹A. U. Oza and J. Dunkel, “Antipolar ordering of topological defects in active liquid crystals,” *New Journal of Physics* **18**, 093006 (2016) (cit. on pp. 21, 29, 46).
- ⁷⁰A. Doostmohammadi, M. F. Adamer, S. P. Thampi, and J. M. Yeomans, “Stabilization of active matter by flow-vortex lattices and defect ordering,” *Nature Communications* **7**, Article, 10557 EP – (2016) (cit. on pp. 21, 29, 46).
- ⁷¹S. P. Thampi, R. Golestanian, and J. M. Yeomans, “Instabilities and topological defects in active nematics,” *Europhysics Letters* **105**, 18001 (2014) (cit. on pp. 21, 29, 46).
- ⁷²A. Bray, “Theory of phase-ordering kinetics,” *Advances in Physics* **43**, 357–459 (1994), eprint: <https://doi.org/10.1080/00018739400101505> (cit. on pp. 22, 24, 55, 58).
- ⁷³S. Puri, “Kinetics of phase transitions,” *Phase Transitions* **77**, 407–431 (2004), eprint: <https://doi.org/10.1080/01411590410001672648> (cit. on pp. 22, 24, 53, 55, 58).
- ⁷⁴R. J. Glauber, “Time-Dependent Statistics of the Ising Model,” *Journal of Mathematical Physics* **4**, 294–307 (1963) (cit. on p. 22).
- ⁷⁵K. Kawasaki, “Diffusion constants near the critical point for time-dependent ising models. i,” *Physical Review* **145**, 224–230 (1966) (cit. on p. 22).
- ⁷⁶P. C. Hohenberg and B. I. Halperin, “Theory of dynamic critical phenomena,” *Review Modern Physics* **49**, 435–479 (1977) (cit. on pp. 23, 32).
- ⁷⁷S Puri and Y Oono, “Effect of noise on spinodal decomposition,” *Journal of Physics A: Mathematical and General* **21**, L755 (1988) (cit. on pp. 23, 56).
- ⁷⁸A. J. Bray, “Exact renormalization-group results for domain-growth scaling in spinodal decomposition,” *Physical Review Letters* **62**, 2841–2844 (1989) (cit. on p. 23).
- ⁷⁹A. J. Bray, “Renormalization-group approach to domain-growth scaling,” *Physical Review B* **41**, 6724–6732 (1990) (cit. on p. 23).

- ⁸⁰D. A. Huse, “Corrections to late-stage behavior in spinodal decomposition: lifshitz-slyozov scaling and monte carlo simulations,” *Physical Review B* **34**, 7845–7850 (1986) (cit. on p. 24).
- ⁸¹S. Dey, D. Das, and R. Rajesh, “Spatial structures and giant number fluctuations in models of active matter,” *Physical Review Letters* **108**, 238001 (2012) (cit. on pp. 25, 52).
- ⁸²Y. Tu, J. Toner, and M. Ulm, “Sound waves and the absence of galilean invariance in flocks,” *Physical Review Letters* **80**, 4819–4822 (1998) (cit. on pp. 25, 52).
- ⁸³J. Stenhammar, A. Tiribocchi, R. J. Allen, D. Marenduzzo, and M. E. Cates, “Continuum theory of phase separation kinetics for active brownian particles,” *Physical Review Letters* **111**, 145702 (2013) (cit. on pp. 25, 52).
- ⁸⁴R. Wittkowski, A. Tiribocchi, J. Stenhammar, R. J. Allen, D. Marenduzzo, and M. E. Cates, “Scalar ph4 field theory for active-particle phase separation,” *Nature Communications* **5**, Article, 4351 EP – (2014) (cit. on pp. 25, 52).
- ⁸⁵Y. Imry and S.-k. Ma, “Random-field instability of the ordered state of continuous symmetry,” *Physical Review Letters* **35**, 1399–1401 (1975) (cit. on pp. 26, 27, 55, 69, 70, 81).
- ⁸⁶G. Grinstein and A. Luther, “Application of the renormalization group to phase transitions in disordered systems,” *Physical Review B* **13**, 1329–1343 (1976) (cit. on pp. 26, 69, 70, 81).
- ⁸⁷T. C. Lubensky, “Critical properties of random-spin models from the ϵ expansion,” *Physical Review B* **11**, 3573–3580 (1975) (cit. on p. 26).
- ⁸⁸D. S. Fisher, G. M. Grinstein, and A. Khurana, “Theory of random magnets,” *Physics Today* **41**, 56–67 (1988) (cit. on pp. 26, 27).
- ⁸⁹A. B. Harris, “Effect of random defects on the critical behaviour of ising models,” *Journal of Physics C: Solid State Physics* **7**, 1671 (1974) (cit. on p. 26).
- ⁹⁰K. Binder and A. P. Young, “Spin glasses: experimental facts, theoretical concepts, and open questions,” *Review Modern Physics* **58**, 801–976 (1986) (cit. on pp. 26, 27).
- ⁹¹F. Corberi, E. Lippiello, A. Mukherjee, S. Puri, and M. Zannetti, “Growth law and superuniversality in the coarsening of disordered ferromagnets,” *Journal of Statistical Mechanics: Theory and Experiment* **2011**, P03016 (2011) (cit. on pp. 26, 27, 60, 63, 64).

- ⁹²F. Corberi, E. Lippiello, A. Mukherjee, S. Puri, and M. Zannetti, “Crossover in growth law and violation of superuniversality in the random-field ising model,” *Physical Review E* **85**, 021141 (2012) (cit. on pp. 26, 27, 63–65).
- ⁹³D. Belitz, T. R. Kirkpatrick, and T. Vojta, “Annealed disorder, rare regions, and local moments: a novel mechanism for metal-insulator transitions,” *Physical Review Letters* **84**, 5176–5179 (2000) (cit. on p. 26).
- ⁹⁴A. Bera, D. Rakshit, A. Sen(De), and U. Sen, “Spontaneous magnetization of quantum xy spin model in joint presence of quenched and annealed disorder,” *Physical Review B* **95**, 224441 (2017) (cit. on p. 26).
- ⁹⁵O. Chepizhko, E. G. Altmann, and F. Peruani, “Optimal noise maximizes collective motion in heterogeneous media,” *Physical Review Letters* **110**, 238101 (2013) (cit. on pp. 26, 27, 69, 70, 81, 82).
- ⁹⁶D. Yllanes, M Leoni, and M. C. Marchetti, “How many dissenters does it take to disorder a flock?” *New Journal of Physics* **19**, 103026 (2017) (cit. on pp. 26, 28, 69).
- ⁹⁷A. Morin, N. Desreumaux, J.-B. Caussin, and D. Bartolo, “Distortion and destruction of colloidal flocks in disordered environments,” *Nature Physics* **13**, 63 EP – (2016) (cit. on pp. 26, 28, 69).
- ⁹⁸D. A. Quint and A. Gopinathan, “Topologically induced swarming phase transition on a 2d percolated lattice,” *Physical Biology* **12**, 046008 (2015) (cit. on pp. 26, 27, 69).
- ⁹⁹C. Sándor, A. Libál, C. Reichhardt, and C. J. Olson Reichhardt, “Dynamic phases of active matter systems with quenched disorder,” *Physical Review E* **95**, 032606 (2017) (cit. on pp. 26, 28, 69).
- ¹⁰⁰T. NATTERMANN, “Theory of the random field ising model,” in *Spin glasses and random fields* (), pp. 277–298, eprint: https://www.worldscientific.com/doi/pdf/10.1142/9789812819437_0009 (cit. on pp. 27, 55).
- ¹⁰¹Kumar, Manoj, Banerjee, Varsha, and Puri, Sanjay, “Random field ising model with conserved kinetics: super-universality violation, logarithmic growth law and the generalized tomita sum rule,” *Europhysics Letters* **117**, 10012 (2017) (cit. on pp. 27, 60, 61).

- ¹⁰²C. J. O. Reichhardt and C. Reichhardt, "Disorder in the wild," *Nature Physics* **13**, 10 EP – (2016) (cit. on pp. 27, 69).
- ¹⁰³R. Aditi Simha and S. Ramaswamy, "Hydrodynamic fluctuations and instabilities in ordered suspensions of self-propelled particles," *Physical Review Letters* **89**, 058101 (2002) (cit. on p. 29).
- ¹⁰⁴F. Peruani, J. Starruß, V. Jakovljevic, L. Søgaard-Andersen, A. Deutsch, and M. Bär, "Collective motion and nonequilibrium cluster formation in colonies of gliding bacteria," *Physical Review Letters* **108**, 098102 (2012) (cit. on pp. 29, 47).
- ¹⁰⁵F. Peruani, T. Klaus, A. Deutsch, and A. Voss-Boehme, "Traffic jams, gliders, and bands in the quest for collective motion of self-propelled particles," *Physical Review Letters* **106**, 128101 (2011) (cit. on p. 29).
- ¹⁰⁶F. D. C. Farrell, M. C. Marchetti, D. Marenduzzo, and J. Tailleur, "Pattern formation in self-propelled particles with density-dependent motility," *Physical Review Letters* **108**, 248101 (2012) (cit. on p. 29).
- ¹⁰⁷P. A. Lebowitz and G. Lasher, "Nematic-liquid-crystal order`22a monte carlo calculation," *Physical Review A* **6**, 426–429 (1972) (cit. on pp. 31, 33).
- ¹⁰⁸S. A. Leonel, P. Z. Coura, A. R. Pereira, L. A. S. Mól, and B. V. Costa, "Monte carlo study of the critical temperature for the planar rotator model with nonmagnetic impurities," *Physical Review B* **67**, 104426 (2003) (cit. on pp. 32, 33, 48).
- ¹⁰⁹E. Mondal and S. K. Roy, "Finite size scaling in the planar lebowitzlasher model," *Physics Letters A* **312**, 397–410 (2003) (cit. on p. 33).
- ¹¹⁰S. Ngo, A. Peshkov, I. S. Aranson, E. Bertin, F. Ginelli, and H. Chaté, "Large-scale chaos and fluctuations in active nematics," *Physical Review Letters* **113**, 038302 (2014) (cit. on pp. 38, 46).
- ¹¹¹S. Coleman and E. Weinberg, "Radiative corrections as the origin of spontaneous symmetry breaking," *Physical Review D* **7**, 1888–1910 (1973) (cit. on p. 45).
- ¹¹²B. I. Halperin, T. C. Lubensky, and S.-k. Ma, "First-order phase transitions in superconductors and smectic-*a* liquid crystals," *Physical Review Letters* **32**, 292–295 (1974) (cit. on p. 45).

- ¹¹³J.-H. Chen, T. C. Lubensky, and D. R. Nelson, "Crossover near fluctuation-induced first-order phase transitions in superconductors," *Physical Review B* **17**, 4274–4286 (1978) (cit. on p. 45).
- ¹¹⁴A. Baskaran and M. C. Marchetti, "Hydrodynamics of self-propelled hard rods," *Physical Review E* **77**, 011920 (2008) (cit. on p. 46).
- ¹¹⁵E. Putzig, G. S. Redner, A. Baskaran, and A. Baskaran, "Instabilities, defects, and defect ordering in an overdamped active nematic," *Soft Matter* **12**, 3854–3859 (2016) (cit. on p. 46).
- ¹¹⁶D. A. Huse and C. L. Henley, "Pinning and roughening of domain walls in ising systems due to random impurities," *Physical Review Letters* **54**, 2708–2711 (1985) (cit. on p. 61).
- ¹¹⁷Z. W. Lai, G. F. Mazenko, and O. T. Valls, "Classes for growth kinetics problems at low temperatures," *Physical Review B* **37**, 9481–9494 (1988) (cit. on p. 61).
- ¹¹⁸S Puri and N Parekh, "Non-algebraic domain growth in binary alloys with quenched disorder," *Journal of Physics A: Mathematical and General* **25**, 4127 (1992) (cit. on p. 61).
- ¹¹⁹R. Paul, S. Puri, and H. Rieger, "Domain growth in random magnets," *Europhysics Letters* **68**, 881 (2004) (cit. on p. 61).
- ¹²⁰S Puri, D Chowdhury, and N Parekh, "Non-algebraic domain growth in random magnets: a cell dynamical approach," *Journal of Physics A: Mathematical and General* **24**, L1087 (1991) (cit. on p. 63).
- ¹²¹J. Olivero and R. Longbothum, "Empirical fits to the voigt line width: a brief review," *Journal of Quantitative Spectroscopy and Radiative Transfer* **17**, 233 –236 (1977) (cit. on pp. 73, 83).
- ¹²²S.-k. Ma, *Modern theory of critical phenomena / shang-keng ma*, English (W. A. Benjamin, Advanced Book Program Reading, Mass, 1976), xxix, 561 p. : (cit. on p. 81).
- ¹²³J. Toner, N. Guttenberg, and Y. Tu, "Hydrodynamic Theory of Flocking in the Presence of Quenched Disorder," ArXiv e-prints (2018), [arXiv:1805.10326 \[cond-mat.stat-mech\]](https://arxiv.org/abs/1805.10326) (cit. on pp. 81, 88, 100).
- ¹²⁴J. Toner, N. Guttenberg, and Y. Tu, "Swarming in the Dirt: Ordered Flocks with Quenched Disorder," ArXiv e-prints (2018), [arXiv:1805.10324 \[cond-mat.stat-mech\]](https://arxiv.org/abs/1805.10324) (cit. on pp. 81, 88, 100).

- ¹²⁵D. J. T. Sumpter, J. Krause, R. James, I. D. Couzin, and A. J. W. Ward, "Consensus decision making by fish," *Current Biology* **18**, 1773–1777 (2008) (cit. on p. 82).
- ¹²⁶L. Snijders, R. H. J. M. Kurvers, S. Krause, I. W. Ramnarine, and J. Krause, "Individual- and population-level drivers of consistent foraging success across environments," *bioRxiv* (2018) 10.1101/260604, eprint: <https://www.biorxiv.org/content/early/2018/02/06/260604.full.pdf> (cit. on p. 82).
- ¹²⁷J. G. Puckett, A. R. Pokhrel, and J. A. Giannini, "Collective gradient sensing in fish schools," *Scientific Reports* **8**, 29765115[pmid], 7587 (2018) (cit. on p. 82).
- ¹²⁸F. Spitzer, "Interaction of markov processes," *Advances in Mathematics* **5**, 246–290 (1970) (cit. on p. 100).